UNIVERSIDADE DE SÃO PAULO
FFCLRP - DEPARTAMENTO DE FÍSICA
PÓS-GRADUAÇÃO EM FÍSICA APLICADA À MEDICINA E BIOLOGIA

Desenvolvimento e caracterização de um tomógrafo óptico para aplicações clínicas

MATHEUS ANTONIO DA SILVEIRA

Ribeirão Preto - SP
2021

UNIVERSIDADE DE SÃO PAULO
FFCLRP - DEPARTAMENTO DE FÍSICA
PÓS-GRADUAÇÃO EM FÍSICA APLICADA À MEDICINA E BIOLOGIA

Desenvolvimento e caracterização de um tomógrafo óptico para aplicações clínicas

MATHEUS ANTONIO DA SILVEIRA

Ribeirão Preto - SP
2021

MATHEUS ANTONIO DA SILVEIRA

Desenvolvimento e caracterização de um tomógrafo óptico para aplicações clínicas

Tese apresentada à Faculdade de Filosofia, Ciências e Letras de Ribeirão Preto da Universidade de São Paulo, como parte das exigências para a obtenção do título de Doutor em Ciências, Área: Física aplicada à Medicina e Biologia

Área de concentração: Física aplicada a medicina e Biologia.

Orientador:
Prof. Dr. Oswaldo Baffa

Co-Orientadora:
Prof. Dra. Juliana Fernandes Pavoni.

Ribeirão Preto –SP
2021

MATHEUS ANTONIO DA SILVEIRA

Development and Characterization of an Optical Computed Tomography for clinical procedures

A thesis submitted in partial fulfillment of the requirements for the degree of Doctor of Philosophy Department of Physics, Faculty of Philosophy, Sciences and Letters of Ribeirão Preto, University of São Paulo.

Study Area: Physics Applied to Medicine and Biology
Advisor: Oswaldo Baffa Filho
Co-Advisor: Juliana Fernandes Pavoni

Ribeirão Preto –SP
2021

FICHA CATALOGRÁFICA

Silveira, Matheus Antonio

Desenvolvimento e caracterização de um tomógrafo óptico para aplicações clinicas / Matheus Antonio da Silveira; orientador Oswaldo Baffa Filho; co-orientadora: Juliana Fernandes Pavoni. Ribeirão Preto - SP, 2020.

118f.:il.

Tese (Doutorado - Programa de Pós-Graduação em Física Aplicada à Medicina e Biologia) - Faculdade de Filosofia, Ciências e Letras de Ribeirão Preto da Universidade de São Paulo, 2021.

1. CT - Óptico. 2.Dosimetria gel. 3.Géis dosimétricos. 4.Controle de qualidade em radioterapia.

Nome: Matheus Antonio da Silveira

Título: Desenvolvimento e caracterização de um tomógrafo óptico para aplicações clínicas

Title: Development and Characterization of an Optical Computed Tomography for clinical procedures

Tese apresentada à Faculdade de Filosofia, Ciências e Letras de Ribeirão Preto da Universidade de São Paulo, como parte das exigências para a obtenção do título de Doutor em Ciências.

Aprovado em: ____/____/____.

Banca examinadora

Prof. Dr.: _____ Instituição: _____

Julgamento: _____ Assinatura: _____

Prof. Dr.: _____ Instituição: _____

Julgamento: _____ Assinatura: _____

Prof. Dr.: _____ Instituição: _____

Julgamento: _____ Assinatura: _____

Prof. Dr.: _____ Instituição: _____

Julgamento: _____ Assinatura: _____

Prof. Dr.: _____ Instituição: _____

Julgamento: _____ Assinatura: _____

Agradecimentos

De maneira muito especial agradeço ao meu orientador Prof. Dr, Oswaldo Baffa Filho, pela oportunidade, sabedoria em sua orientação, apoio, incentivo, paciência e amizade, no decorrer do desenvolvimento do trabalho. O Professor Baffa é uma pessoa muito ocupada e dedicada à ciência e a academia, mas nunca mediu esforços para ajudar e ensinar no que for necessário. Por fim quero dizer que a pessoa do professor Baffa é sim uma grande inspiração para o caminho da ciência e do conhecimento.

À Professora Dr. Juliana Fernandes que também orientou esse trabalho, sua pelos seus ensinamentos em radioterapia e sua disciplina inspiradora. Poderia escrever muito sobre essa pessoa fantástica que é a professora Juliana, mas resumindo, não tem como sair desmotivado depois de uma conversa com ela em sua sala.

Ao Professor Dr. Kevin Jordan por ter me recebido em seu laboratório em London na província de Ontario no Canadá. Com certeza existe um Matheus antes e depois desse período que fiquei sob sua orientação, seus ensinamentos completaram e potencializaram tudo que aprendi com o Professor Dr. Baffa e a Professora Dr. Juliana.

Aos funcionários do Departamento de Física, Nilza, Ricardo, Loureço, Serginho, Aziane, Agnelo, Carlão, Fernando, por toda ajuda que necessitei.

A todos os professores do programa FAMB, a aqueles que tiveram contato comigo e a aqueles que não tiveram, quero dizer que cada um que, de maneira especial, são transmissores de uma inspiração diferenciada para seguir o caminho da ciência.

Aos meus pais, meu irmão e meus avós que sempre me incentivaram, apoiaram e estão comigo em todos os momentos da minha vida, tanto nos momentos de alegria como de tribulações.

Ao Hospital das Clínicas de Ribeirão Preto, pessoal da radioterapia pelas irradiações necessárias em cada etapa do trabalho.

Ao Hospital do Amor em Barretos que proporcionou as irradiações desse trabalho.

Agradeço a todos os meus colegas de pós-graduação, por caminharem junto a mim durante esse período de crescimento.

À CAPES pelo apoio financeiro.

À USP pelo local de trabalho e toda sua infraestrutura.

À Nossa Senhora das Graças, minha padroeira por sua intercessão nessa etapa da minha vida.

E finalmente à Deus por ter proporcionado esse momento de crescimento e santificação, pois sem Ele não existiria sentido em minha vida.

Muito Obrigado.

Resumo

Silveira, Matheus Antonio. **Desenvolvimento e caracterização de um tomógrafo óptico para aplicações clínicas**. 2021 118f. Tese (Doutorado – Programa de Pós-graduação em Física Aplicada à Medicina e Biologia) – Faculdade de Filosofia, Ciências e Letras de Ribeirão Preto, Universidade de São Paulo, Ribeirão Preto – SP 2021

O surgimento de tecnologias em radioterapia, como a radioterapia de intensidade modulada (IMRT) e a irradiação volumétrica em arco (VMAT) permitem uma deposição de elevada dose ao tecido tumoral ao mesmo tempo em que protegem o tecido sadio devido à sua precisão. Junto com essa evolução também surge a necessidade de rigorosos controles de qualidade e verificando informações cada vez mais completas, visto que, hoje não há uma medição de dose verdadeiramente tridimensional (3D) no contexto clínico para simular e reproduzir fielmente o tratamento de radioterapia a ser executado no paciente. Para suprir essa necessidade a dosimetria gel associada a uma técnica de imagem vem ganhando destaque por fornecer essa informação 3D para a dose absorvida. A medição 3D da dose absorvida pode ser feita irradiando um gel radiocrômico ou polimérico e a dose pode ser determinada por uma técnica de imagem como ressonância magnética, tomografia computadorizada de raios-x ou mesmo um tomógrafo ótico com luz visível. Considerando essa demanda, nesse trabalho é desenvolvido um tomógrafo ótico para ser utilizado na rotina clínica como um sistema de dosimetria para controle de qualidade 3D. Nesse trabalho é montado um tomógrafo ótico baseado em um feixe de iluminação e aquisição em cone (*Cone beam optical computed tomgraphy* – CBCT), sua caracterização ótica e dosimétrica necessária para a reconstrução de imagens de qualidade, é apresentada. O CBCT construído nesse trabalho apresentou baixa contaminação e luz dispersa, coeficiente de atenuação e dose absorvida de acordo com as técnicas já consolidadas, espectrofotômetro e a câmara de ionização, respectivamente. Para utilizar o CBCT no contexto clínico durante o trabalho surgiu a necessidade de se desenvolver um gel radiocrômico que fosse utilizável em temperatura ambiente e apresentasse características dosimétricas estáveis. Assim, os géis Fricke – Xylenol - Orange (FXO) e o Turnbull – Blue (TB) foram modificados e tiveram na sua composição a adição de formaldeído. Os dois géis tiveram seus pontos de fusão aumentados significativamente e não apresentaram dependência energética e com a taxa de dose da irradiação. Entretanto, para aplicação em medidas 3D de interesse clínico foi escolhido o gel FXO – f (FXO com formaldeído). Finalmente, o CBCT combinado com o gel FXO-f foi utilizado para o controle de qualidade 3D em um tratamento de neuroeixo, onde foi avaliada a distribuição de dose na região de junção dos campos de tratamento cranial e espinhal, planejados usando IMRT. Nesse controle foram encontradas regiões de alta aprovação na análise gama, mas regiões com reprovação, abaixo dos 90% e que não foram encontradas no controle de qualidade convencional.

Palavras-chave: CT - Óptico; Dosimetria gel; Géis dosimétricos; Fricke - Xylenol-Orange; Turnbull-Blue; Controle de qualidade em radioterapia.

Abstract

Silveira, Matheus Antonio. **Development and Characterization of an Optical Computed Tomography for clinical procedures**. 2021. 118p. A thesis submitted in partial fulfillment of the requirements for the degree of Doctor of Philosophy Department of Physics, Faculty of Philosophy, Sciences and literature of Ribeirão Preto – SP, 2021.

The emergence of new technologies in radiotherapy, such as intensity-modulated radiotherapy (IMRT) and volumetric arc irradiation (VMAT) allows a high dose deposition to tumor tissue while protecting healthy tissue. Along with this evolution, there is also the need for strict quality controls and more and more complete information, since, today, there is no truly three-dimensional (3D) measurement in the clinical context to simulate and faithfully reproduce the radiotherapy treatment to be performed in the patient. To meet this need, the dosimetry gel associated with an imaging technique has been gaining prominence for providing this 3D information for the absorbed dose. The 3D measurement of the absorbed dose can be done by radiating a radiochromic or polymeric gel. The dose calculation can be done by an imaging technique such as ultrasound, magnetic resonance, X-ray computed tomography, or even an optical tomography with visible light. Considering this demand, in this work, an optical tomography is developed to be used in the clinical routine as a 3D quality control. In this work, an optical tomography based on a beam and cone acquisition (Cone beam optical CT - CBCT) is assembled and its optical and dosimetric characterization is necessary for the reconstruction of quality images. The CBCT built in this work showed low contamination and scattered light, attenuation coefficient, and absorbed dose according to the techniques already consolidated, spectrophotometer and the ionization chamber, respectively. To use CBCT in the clinical context during work, the need arose to develop a radiochromic gel that could be used at room temperature and had stable dosimetric characteristics. Thus, Fricke - Xynelol - Orange (FXO) and Turnbull - Blue (TB) gels had in their composition the addition of formaldehyde. The two gels had their melting points significantly increased and did not show energy and dose rate dependence. However, for clinical application the FXO - f gel (FXO with formaldehyde) was chosen. Finally, the CBCT combined with the FXO-f gel was used for 3D quality control in a craniospinal treatment where the region of the junction of this planned irradiation in multiple isocenters was evaluated. In this control, regions with high approval were found in the gamma analysis, but regions with disapproval, below 90%, were not found in conventional quality controls.

Keywords: Optical –CT, Gel Dosimetry, Radiochromic gel, Fricke–Xylenol–Orange, Turnbull-Blue, Radiotherapy Quality Assurance.

List of figures

List of Tables

List of Abbreviations

2D ..... two-dimensional

3D ..... three-dimensional

AAPM .....American Association of Physicists in Medicine

ADU .....analog-digital units

CCD .....charge coupled device

CNR .....contrast to noise ratio

CT ..... computed tomography

CTV ..... clinical target volume

DTA ..... distance to agreement

EBRT/XBRT .....external beam radiation therapy

FBP .....filtered backprojection

FT .....Fourier transform

FFT ..... Fast Fourier transform

FWHM ..... full width at half maximum

FXO ..... ferrous xylenol orange

GPU .....graphics processing unit

GTV .....gross tumour volume

He-Ne ....helium-neon

kVCT .....kilovoltage computed tomography

ICRU .....International Commission on Radiological Units

IGRT .....image guided radiation therapy

IMRT .....intensity modulated radiation therapy

IROC .....Imaging and Radiation Oncology Core

ITV ..... internal target volume

LED .....light emitting diode

MLC .....multileaf collimator

MRI .....magnetic resonance imaging

MU ..... monitor unit

MV ..... megavoltage

OAR .....organ at risk

OBI ..... on-board imaging

OD ..... optical density

SIRT-TV…….. Simultaneous iterative reconstruction technique with total variation minimization

OSL .....optically stimulated luminescence

PDD .....percent depth dose

PETE ..... polyethylene terephthalate

PMMA.....polymethyl methacrylate

PTV .....planning target volume

QA ..... quality assurance

RDF .....relative dose factor

ROF .....relative output factor

ROI .....region of interest

RTAP .....resolution, time, accuracy, precision

SNR .....signal to noise ratio

SPR .....scatter to primary ratio

TAR .....tissue to air ratio

TLD .....thermoluminescent dosimeter

TPR .....tissue to phantom ratio

TPS ..... treatment planning system

VMAT …… volumetric modulated arc therapy

Table of Contents

Chapter 1 - General Introduction

1.1 Cancer Basis and Radiation Therapy

Cancer is a disease characterized by a genetic mutation that generates uncontrolled cell growth. This conduces to a malignant tumor formation, able to spread to different organs' tissues leading to death. There are multiple factors, for example, hereditary and pathogens, that increase the probability to cause cancer, to complicate scenario, some cancers appear without a known cause. Thus several treatments are employed to control and in some cases cure cancer.

In Brazil, according to National Cancer Institute-INCA (Instituto Nacional do Câncer), in the years 2020 through 2022, around 625.000 new cases were estimated, for men and women. Among these cases, ,177.000 patients will have skin cancer and the number of new cases of prostate and mama cancer are estimated in 66.000 each (INSTITUTO NACIONAL DE CÂNCER JOSÉ ALENCAR GOMES DA SILVA., 2020).

Radiation therapy uses ionizing radiation as part of a cancer treatment combined with surgery, chemotherapy, hormone therapy and immunotherapy to control tumor cell growth. The main objective of radiation therapy can be curative. The context of radiation therapy includes adjuvant treatment to keep cancer from returning, neoadjuvant treatment to reduce tumors before the main treatment (surgery, for example), or palliative treatment to relieve symptoms of the disease. (Khan and Potish, 1998).

The application of radiation therapy is commonly done infractions to give the healthy cells a chance to recover. To save healthy tissues, conformational radiation beams are faced to the target volume from different angles of exposure to provide a much larger

absorbed dose to the tumor than to the normal tissue. The absorbed dose (D) is measured in Gray (Gy), the standard unit of absorbed ionizing-radiation amount, corresponding to one joule per kilogram (J/Kg) (Khan,2014, ATTIX et al, 1992).

Over these years, significant advances beyond the 3DCRT (3D conformational radiotherapy) in the context of conformational radiation therapy can be cited, such as the IMRT (Intensity-modulated radiation therapy) using the multi-leaf collimators (MLC), provide the conformation while modulating the field intensity. This can be done in static or moving the MLC during the irradiation. The result of this irradiation process is different intensities to the irradiation region, high doses to the PTV and less dose to the OAR (Zelefsky et al., 2002). Another implementation is the intensity-modulated arc therapy (VMAT). In this technique, the intensity-modulated dose is delivered continuously with the linear accelerator gantry rotation (Yu et al.,1995) while the velocity of the gantry, consequently, dose rate varies, Depending on the planning treatment, also the MLC aperture shape is varied over one or more gantry arcs during the dose delivery. This contemporary technique provides less irradiation time than conventional irradiation and IMRT. In summary, the main goal of these new developments is the possibility to deliver more doses to the target volume, and less dose to the risk organs. This ability combined to the irradiation fraction can save normal tissues from irradiation damage (Gedik et al., 2017, Vanneste et al.,2016). Figure 1.1 presents a visual comparison between the conventional 3DRTm IMRT and VMAT techniques.

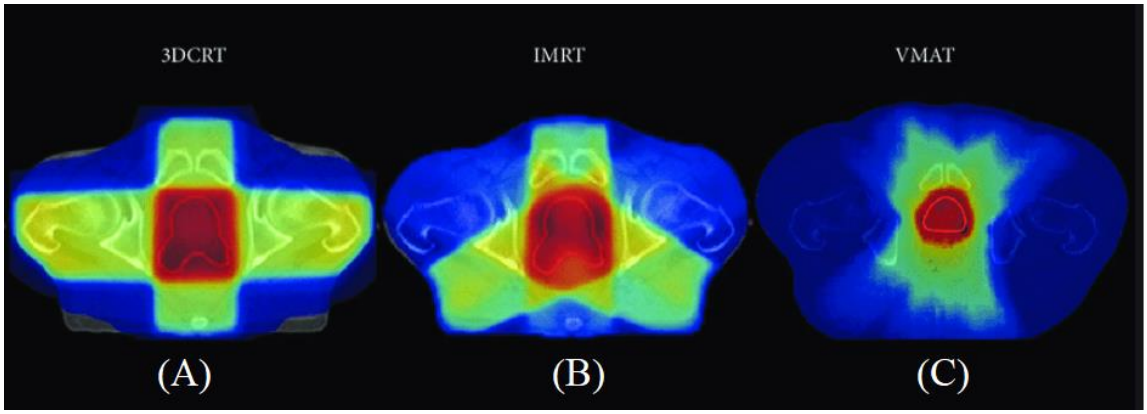

Figure 1.1: Radiation therapy for prostate cancer (A) 3D conformational radiotherapy (B) Intensity modulated radiotherapy (C) Volumetric arc therapy. Figure extracted and modified from Vanneste et al, 2016

1.2 Radiation Therapy planning

Once the radiotherapy treatment is recommended for cancer treatment, the patient is submitted to an x-ray computed tomography (CT). This first process will localize and visualizes the tumor shape with the patient at the treatment positioning. Additional image techniques can be required, mainly magnetic resonance image (MRI), or positron emission tomography (PET) for better delineation and characterization of the tumor. (Brown et al. 2017, Khan and Potish, 1998, Webb 2003)

The planning images from CT are imported to Treatment Planning System (TPS), a software dedicated to calculating the spatial form and deliver dose fields to irradiate the target volume. In this process it is important to delineate the planning target volume (PTV) and organs at risk (OAR) and, finally, based on the clinical protocols for the specific tumor, the oncologist prescribes the radiation dose to the target volume. This prescription is based on the clinical protocols associated with OAR dose constraints. (Khan and Potish, 1998)

1.3 Radiation Therapy dose verification

The new technologies on radiation therapy are increasing the demand for real tridimensional quality assurance (3DQA) for complex planning treatment. At the

moment, a truly 3DQA is not present in the clinical context. Ionization chambers, diodes, metal oxide semiconductors field-effect transistors (MOSFET), and thermoluminescent dosimeters (TLD) are examples of dosimeters used in the clinical context for a dose verification in a point or a small volume. Flat-panel, array of detectors, scintillator devices, and radiochromic film dosimetry are used for two-dimensional dosimetry. To perform a 3D dose verification, it is possible to use the film dosimetry in multiple planes, however, this kind of procedure involves multiple 2D images and a reconstruction algorithm to find a 3D dose information, the verification becomes a challenging process to get and process the data (Khan and Potish, 1998). A truly 3D process solves this problem. Because of this, a gel dosimeter associated with an optical tomography is one of the new candidates to perform the complete 3D dosimetry in the clinical context.

1.4 – Gel dosimetry

Gel dosimeters are radiosensitive chemicals immersed in a matrix that can be of animal origin as gelatin or synthesized as polyvinyl alcohol or acrylamide. Upon radiation, water radiolysis initiates a chemical reaction resulting in the growth of polymer, in the case of a polymer gel dosimeter, or the color change in the case of the radiochromic gel dosimeter. This change is related to the absorbed dose delivered at a particular point of the gelatin matrix volume. This ability, combined with an imaging technique such as MRI, CT, optical CT, or ultrasound, can be used for 3D dose reconstruction and verification by comparing it to the TPS data in the radiotherapy planning. This type of dosimeter provides a complete and truly 3D QA simulating the real patient treatment. There are several groups around the world investigating this area (Baldock et al., 2010). For example, the investigation of the accuracy of MRI gel dosimeters (De Deene et al, ,1988, De Deene et al., 2020, Maryanski et al.,1994), Monte Carlo simulation for MAGIC-f polymer gel dosimeter (Alva et al.,2010, Quevedo et al., 2017), new chemicals

to reduce diffusion in Fricke gels, (Smith et al,.2019.), the studding of absorbance in radiochromic gels (Gambarini et al., 2017), non toxicity gels like genipin gels (Jordan K, 2009), plastic gels, Flexdos3D®(De Deene et al., 2015, and PRESAGE®(Grant et al 2013, Khezerloo et al., 2017) and development and modification of OCTs (Jordan et al.,2017).

1.4.1 – Fricke gel dosimeter

Fricke gel dosimeter (figure 1.2) is a combination of a ferrous sulphuric acid with xylenol orange in a gelatin matrix, was used as a dosimeter by Gore *et al* (Gore et al, 1984) on the determination of 3D dose distribution using MRI. When irradiated, the water radiolysis induces the ferrous (Fe^{2+}) oxidation to ferric ions (Fe^{3+}) (Fricke and Hart,1955)., resulting in a visible color change because of the pH indicator xylenol orange The physical properties of this change upon radiation are related to the absorbed dose. Equation 1.1 to 1.4 present the chemical reaction upon radiation and water radiolysis.

$$Fe^{2+} + OH\bullet \rightarrow Fe^{3+} + OH^{-} \quad (1.1)$$

$$Fe^{2+} + + HO_2\bullet \rightarrow Fe^{3+} + HO_2^{-} \quad (1.2)$$

$$HO_2^{-} - + H_3O^{+} + \rightarrow H_2O_{2+} + H2O \quad (1.3)$$

$$Fe^{2+} + H_2O_2 \rightarrow Fe^{3+} + OH\bullet + OH^{-} \quad (1.4)$$

FXO gel dosimeter demonstrated a well dose-response, linearity, and easy manufacturing. These characteristics become the FXO dosimeter a reference for radiochromic dosimeters to use in development and comparisons of new tools in gel dosimeter context. (Alexander et al., 2015, De Deene et al., 2015, Kelly et al, 1988, Solc et al., 2009). However, the major concern for this gel dosimeter is the diffusion of the ferric ions inside the gelatin matrix resulting in the loss of the spatial distribution of the absorbed dose (Kron et al. ,1988, Rae et al.,1996).

Several studies about FXO gel dosimeter tried to improve sensitivity for low doses and reduce ferric ion diffusion. (Schreiner L ,2014). Chapter 3 will present the addition

of formaldehyde to FXO gel to improve melting point and the effect on the diffusion coefficient.

Figure 1.2: 15cm cylinder diameter and 12cm tall filled with FXO gel dosimeter; Left: non-irradiated; Right: Irradiated at the central portion with 3 Gy PDD max dose.

1.4.2 – Turnbull – Blue gel dosimeter

The chemical reagent Turnbull blue (figure 1.3) is the same chemical as the well known Prussian's blue, differing only on the reaction route to obtain the final compound. Balog et al,1999, reported the chemical reaction upon radiation of the Turnbull blue formation, equation (1.5) and (1.6) and the same reaction happens inside the gelatin matrix. Solc et al report the dosimeter based on the Turnbull-blue formation, using gelatin and phytagel, a type of agar gel with the high optical transmission, to record the 3D absorbed dose in a matrix. The great advantage comparing to the FXO gel dosimeter is the inhibition of the diffusion (Solc et al, 2009). However, the organic compounds present inside the gelatin matrix include spontaneous aging. With time, there is an autoxidation reaction, and the dosimeter becomes dark and is not useful for dosimetry. Recent applications demonstrated good results in determining the tridimensional dose distribution (Kozubikova et al,2015).

$$2[Fe(III)(ox)_3]^{3-} + h\upsilon = 2Fe(II)(ox)_2^{2-} + 2CO_2 + ox^{2-} \quad (1.5)$$

$$Fe(II)(ox)_2^{2-} + [Fe(III)(CN)_6]^{3-} + K^+ = K[Fe(II)Fe(III)(CN)_6] + 2(ox)^{2-} \quad (1.6)$$

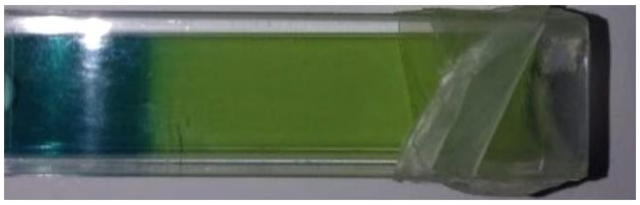

Figure 1.3: Irradiated Turnbull-Blue sample

1.4.3 – Important considerations of dosimeters

There are various type of dosimeters, each one has its particularities, advantages, and disadvantages. According to Attix (1986) it is important to consider some characteristics of the dosimeters when analyzing a possible application. (ATTIX, 1986) These characteristics are:

Tissue and Water Equivalence

The clinical dosimetry and commissioning tasks are performed in a water medium to simulate the absorption and scattering of ionizing radiation in the human body. Having a dosimeter with similar absorption and scattering characteristics as water or tissue, for the type of particles being used to irradiate, allows the interpretation of the dosimetry results more direct, without introducing additional conversion factors uncertainties.

Accuracy

Accuracy refers to how closely a dosimeter agrees with the true value of the absorbed dose. In dosimetry, it is usually defined based on a comparison against a consolidated dosimeter and calibration laboratory. Typically, the ionization chamber measurement is the standard partner.

Precision

Precision is related to the reproducibility of the measurements and is expressed in terms of the standard deviation of a set of repeated measurements. Precision is limited by the noise in the dosimeter or its associated readout system.

Sensitivity

Sensitivity is the rate of change in the dosimeter's readout signal concerning an increasing dose. Graphically, it is the slope of a dosimeter's Readout Signal versus Dose graph.

Linearity

This characteristic is not mandatory, however, a dosimeter whose reading increases linearly with absorbed dose is easier to calibrate than a non-linear dosimeter.

Energy Independence

A dosimeter's sensitivity must exhibit little or no dependence on incoming radiation energy because the energy spectrum of treatment photon beams is broad and changes with depth in tissue. This implies that a dosimeter calibration at the incident beam energy will not guarantee the accuracy of measurements within an absorber unless the dosimeter response is energy-independent.

Dose Rate Independence

For an integrating dosimeter, the response must not be dependent on the rate at which the dose is absorbed. If this is not the case, the reading from the dosimeter must be corrected using additional information because the dose rate at different points in an absorber for a delivered radiation beam varies significantly.

Temporal Stability

Temporal stability refers to the stability of the dosimeter reading as a function of time after irradiation. For example, some radiochromic gel dosimeters exhibit an auto-oxidation or fading that may need to be corrected at readout time. In general, for an integrating dosimeter, we want the dosimeter's response to radiation to be stable for at

least the delay before readout and during readout (unless the readout involves “erasing” the dose signal). A lack of temporal stability may sometimes be misdiagnosed as a dose rate dependence in the dosimeter during very long exposures.

Dose Range

Ideally, a dosimeter can be used for any dose level, within the range of interest. Many dosimeters, however, exhibit a saturation level, or a threshold below which the response is not measurable. This limited range may be due to the dosimeter response itself, or the accompanying readout systems.

Spatial Resolution

The true spatial resolution of a dosimeter is the smallest volume in which meaningful dosimetric information can be provided. This is linked to the size of the sensitive volume for point dosimeters and is tied to the image noise and readout spatial resolution for integrating 2D and 3D dosimeters, for example, films and gels.

Environmental Conditions

The ambient temperature (or pressure) within the sensitive volume should not affect the response in the clinical context. This parameter is always controlled and fixed at the irradiation time. However, for a 3D dosimeter is preferred to have a higher melting point than the environment to keep the spatial information on the matrix that could be a gelatin or a polymer.

1.4.1 – Gel dosimeter scanning

The gel dosimeter can record tridimensional information related to absorbed dose on the matrix. For this determination, an imaging technique is required to associate the image parameter to the absorbed dose. For the polymer gels using Fricke solution as sensitive medium MRI images are preferred to associate the relaxation rate of protons to the absorbed dose, Ultrasound and X-ray-CT can be also used for the determination of

the 3D dose distribution for the polymer gels, however, these image techniques do not have the same sensitivity as MRI for the 3D dosimetry and one problem associated with all of them is the fact that usually, they are available in different departments and not in the radiotherapy section in a hospital, what complicate the logistics (Baldock et al, 2010). On the other hand, an optical computed tomography (OCT) can be dedicated to the radiotherapy service to perform quality assurance. Compared to the other image techniques, OCT has a lower cost and can be dedicated only to 3D QA. In the following section, the principles of optical computed tomography applied to scanning irradiated radiochromic gels dosimeters will be described (Islam et al 2003, Campbell et al 2015).

1.5 – Optical Computed Tomography – OCT

The OCT principles in analogous to x-ray CT and optical projection tomography, however, to acquire an image, the light source is visible light, and the detector can be a photography camera, a CCD, or a CMOS detector, for example (Sharpe et al.,2002). The next subsections present the optical computed tomography basic principles related to this work.

1.5.1 Computed tomography basics

The computed tomography mathematics is well described in Kak and Slaney's textbook published in 1998, "*Principles of computed tomography*" providing a detailed explanation and math demonstrations. Thus, in this section, we will briefly outline the principles to contextualize the construction of the optical-CT present in this work (Kak and Slaney, 1988).

Photon Attenuation

Consider a beam of photons traveling through a block of material. Within the material, some of the photons will interact with the atoms. The nature of these outcomes will depend on the photon energy (visible range, x-ray, megavoltage x-ray, for example). Depending on the nature of the sample, the predominant interaction can be absorption, where the photon is absorbed by the sample, or scattering, where the photon is deflected from the initial beam. These two effects generate fewer intensities thorough the sample, this signal's loss of primary photons is called attenuation. The fraction of incident photons removed from a narrow, monoenergetic beam per thickness unit of the medium is referred to as the linear attenuation coefficient (μ) of that material and is usually expressed in units of cm^{-1}. To relate this attenuation effect of a N_0 number of the photons we can use the Beer-Lambert law as:

$$N = N_0 e^{-\mu x} \quad (1.7)$$

Where N is the number of the photons after the attenuation process, μ, is the linear attenuation coefficient, and x is the thickness of the sample. In practice, the amount of the photons is not measured directly but as an effect related to them. In the context of the CT image reconstruction, we always related this number of the photons to the intensity, being I, its value after the attenuation and I_0 it values before the attenuation. So, we have:

$$I = I_0 e^{-\mu x} \quad (1.8)$$

Equation 1.8 can be modified to evaluate the linear attenuation coefficient, usually determined on the CT reconstructions.

$$\mu = -\frac{1}{x} Ln\left(\frac{I}{I_0}\right) \quad (1.9)$$

However, in practice, the material is not uniform, along the interior of the sample the linear attenuation coefficient is different, and, can be understood as a function of the thickness μ(x), for example in figure (1.4):

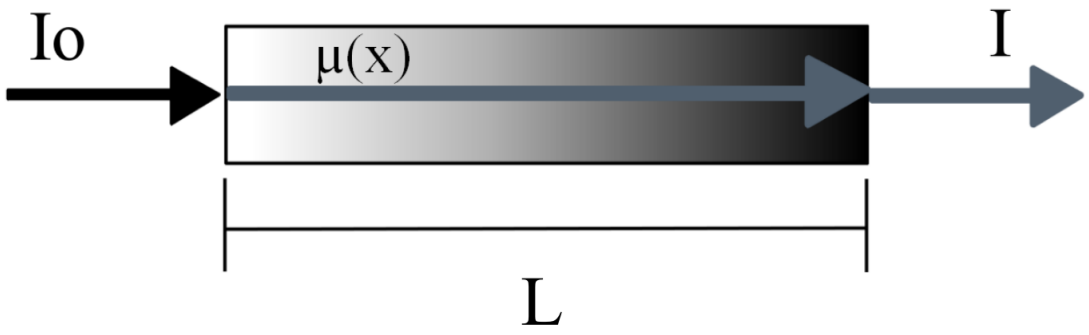

Figure1.4: Attenuation of the primary photons along with sample material.

In this case of the transmission through a sample, the intensity decay along a total thickness L can be rewriting as a line integral of the linear attenuation coefficient.

$$I = I_0 e^{-\int_0^L \mu(x)dx} \quad (1.10)$$

And, taking the logarithm and rearranging the terms we generate:

$$\int_0^L \mu(x)dx = -Ln\left(\frac{I}{I_0}\right) \quad (1.11)$$

In a real OCT experiment, the acquired signal is represented by I and Io. In the context of the gel dosimetry, Io is the intensity signal of non-irradiated simulator object and I is the intensity signal from irradiated object. In absorption spectroscopy, Io is often the acquisition of the water and I intensity along with the sample.

Projections

The projection is defined as the set of line integrals along the object for a determined angle, (equation 1.11). The projections can be acquired using a parallel beam,

fan beam, and, for a 3D acquisition, a cone beam light geometry (figure, 1.5). The simplest case in the parallel beam projections, the integral of the absorption coefficient along the line is known in the literature as Radon Transform, and to obtain the original image object the inverse of radon transform is applied to projections (Radon, 1917).

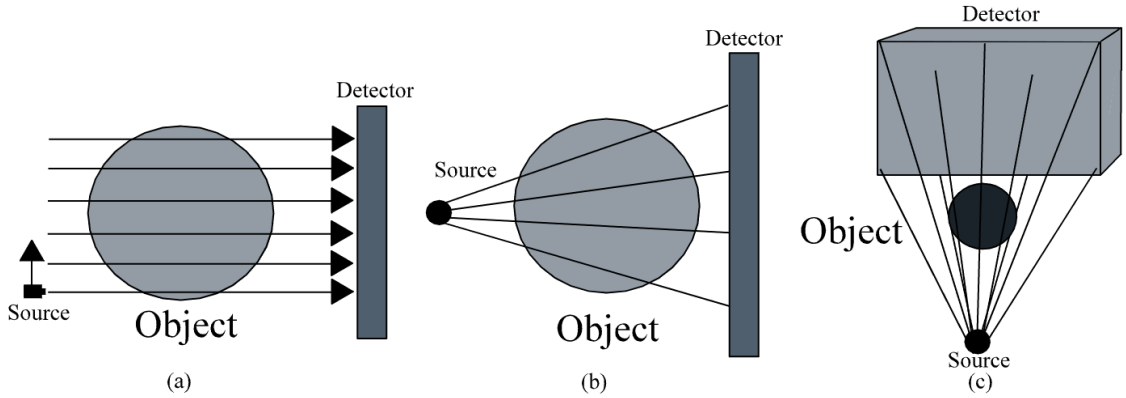

Figure 1.5: a) parallel beam, b) fan-beam and c) cone-beam for CT – projections

The Fourier Slice Theorem and tomographic reconstruction

To understand the CT reconstruction of a set of projections, the Fourier slice theorem presents the mathematics fundamentals. For example, consider a set of parallel-beam projection ($P(\theta)$) at a given angle (θ) along the two-dimensional object denotes as a function, $f(x,y)$ (Figure1.6). In the Fourier domain, the 1D Fourier transform of this projection is a line in this frequency domain (red line in figure 1.6). So, if we obtain all 1D Fourier transform lines around the object function we complete the frequency domain. Therefore, applying the 2D Fourier inverse transform we recover the original object function $f(x,y)$.

The projection data acquired is a transmission data (equation 1.10), then, we can take the natural logarithmic to transform them in a set of line integrals of μ values within the object to reconstruct the original sample. Radon in 1917 proved and reported this technique to reconstruct images from an infinite number of projections.

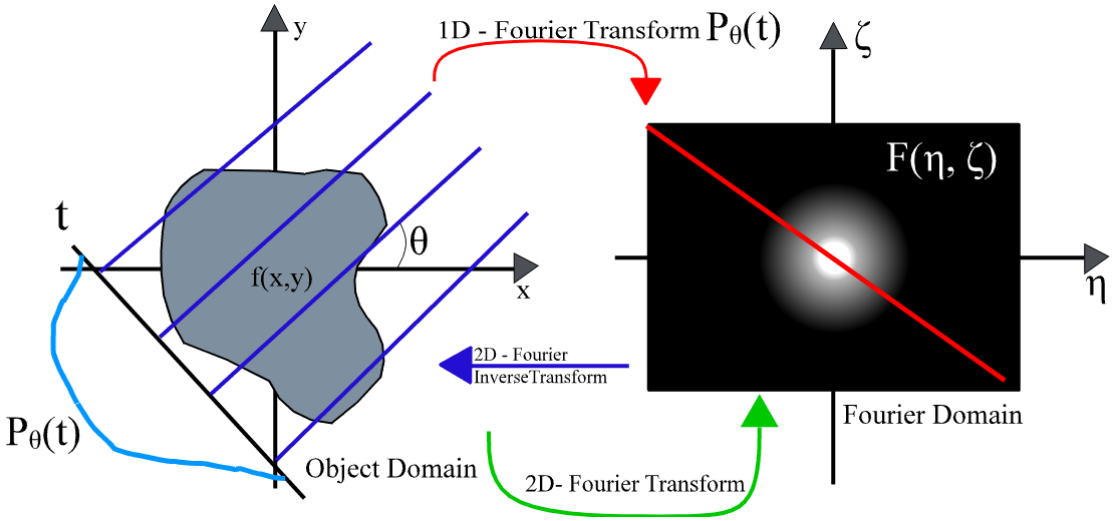

Figure 1.6: The Fourier Slice Theorem. The 1D Fourier transform of a projection P(θ) at angle θ is equal to the 2D Fourier transform of the object at the same angle in the spatial frequency domain.

In practical medical CT images, the Fourier slice theorem is of no use, for some reasons. The acquired images are not continuous data but discrete data. So, the Fourier transform needs to be discretized, this results in a 2D Fourier domain filled in polar coordinates, while the desired object is in Cartesian coordinate. This discretization results in an incomplete information in frequency domain. To complete frequency domain data, an interpolation is needed to fill the "holes" (loss data), but this calculation generates a blurred image and the whole process demands time, a problem not desired in medical image context. Figure 1.6 shows the general scheme and Figure 1.7 A-B the result of the data discretization in the Fourier domain that generate the blurred image, shown in figure 1.7C.

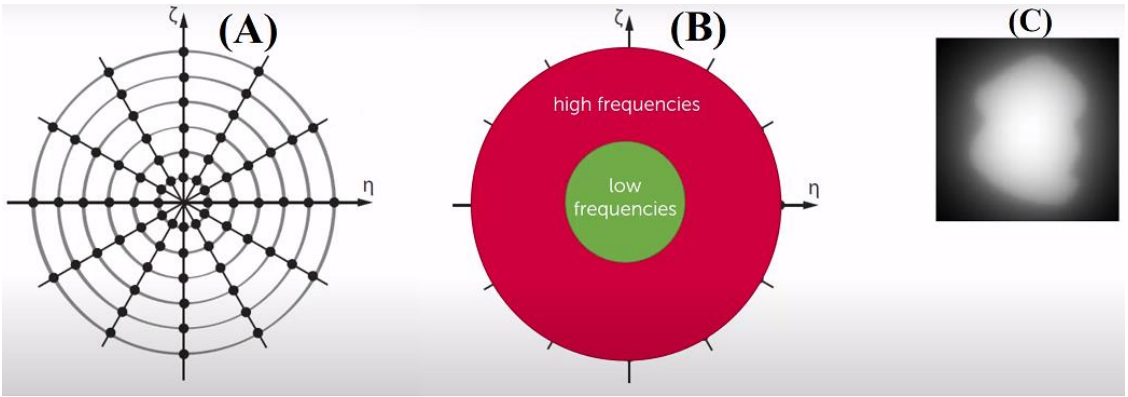

Figure 1.7: a) The radial density of projection image data in frequency space. (b)Representation of the high and low frequency. (c) This resulted in a blurred image. Figure extracted from Astra-toolbox https://www.youtube.com/channel/UCcnUlWuFeS9miMR_o8-6v3w

To solve this problem CT images are typically reconstructed using a filtered back-projection algorithm to remove this blurred from the image.

The filtered - back projection in tomographic reconstruction

In this section we will introduce the simplest reconstruction mathematics to parallel beam to contextualized this reconstruction technique and describe the FDK algorithm for the cone-beam geometry. The complete mathematics is discussed in Kak and Slaney (1998) for parallel beam and fan-beam and in the paper "*Practical cone-beam algorithm"* reported by Feldkamp, Davis, and Kress in (Feldkamp et al, 1984) the complete mathematics for cone-beam, and also fan-beam reconstruction is fully discussed.

Parallel- beam geometry

We consider a set of parallel beams to describe filtered back projection (FBP), the simplest acquisition setup. The projection data obtained by acquisition is Pθ(t), the discrete Fourier transform is called Fast Fourier transform (FFT), we denote here as Pθ(ω), the raw-lak filter applied in the frequency domain to remove the blurring is written as H(ω), so, Qθ(ω) is obtained to do the Inverse Fast Fourier transform (IFFT) and then, finally the Qθ(t) as a filtered projection is found. Figure 1.8 presents a total scheme of a filtered back projection.

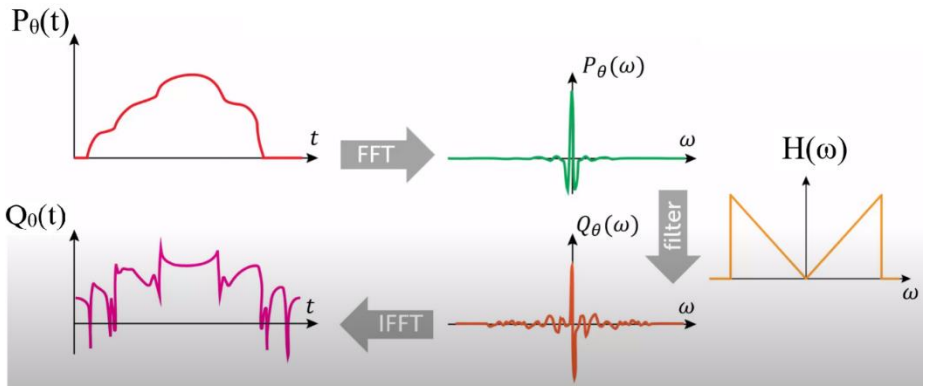

Figure 1.8: a) Scheme of the Filtered back projection. Figure extracted from Astra-toolbox https://www.youtube.com/channel/UCcnUlWuFeS9miMR_o8-6v3w

Mathematically for the parallel beam the projection $P_\theta(t)$, is:

$$P_\theta(t) = \int_{-\infty}^{+\infty}\int_{-\infty}^{+\infty} f(x,y)\delta(xcos\theta + ysin\theta - t)\,dx\,dy \quad (1.12)$$

This equation is termed the Radon transform of an object f(x,y), and $Q_\theta(t)$ the result of the IFFT.

$$Q_\theta(t) = \int_{-\infty}^{+\infty} P_\theta(\omega)H(\omega)e^{j2\omega t}\,d\omega \quad (1.13)$$

The complete mathematics path for equations 1.12 to 1.13 is presented in Kak and Slaney (1988).

Cone Beam Geometry

The cone-beam filtered-back projection reconstruction is commonly used in the FDK algorithm (Feldkamp et al.,1984). The logic is the same as for the fan beam, pre-weighting the acquired projections to apply filtered-back projection. Each elevation is considered separately as a single fan beam that needs to be transformed to parallel. Thus, the final tridimensional reconstructed object has resulted in each contribution sum of each fan beam around the acquired object.

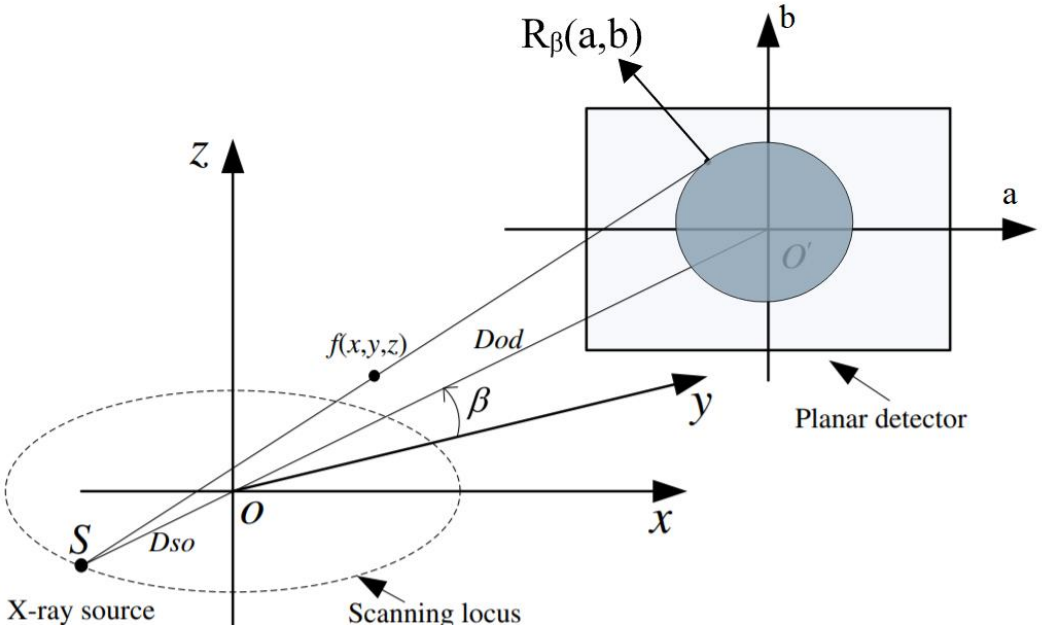

Figure 1.9: Geometry and notation for the single projection Rβ(a,b) corresponding to a cone- beam 2D linear detector configuration. Figure modified from Zhang et al, 2018 in DOI:10.1002/cpe.4697.

In figure 1.9, S is the source, Dso is the distance from S to the rotation center, Dod is the distance from rotation center O to the planar detector, $R_\beta(a,b)$ is a single line of an acquired projection at angle β.

First, the projection rays are pre-weighted according to their position within the 3D cone:

$$R'_\beta(a,b) = R_\beta \frac{Dso}{\sqrt{Dso^2+a^2+b^2}} \qquad (1.14)$$

Where a and b are the result of the back-projecting the voxel position (x,y,z)

$$a(x,y,\beta) = Dso \ \frac{xcos\beta+ysin\beta}{Dso+xsin\beta-ysin\beta} \qquad (1.15)$$

$$b(x,y,\beta) = Dso \ \frac{z}{Dso+xsin\beta-ysin\beta} \qquad (1.16)$$

The pre-weighted projections can be filtered by the convolution:

$$Q_\beta(a,b) = R'_\alpha(a,b) * g(a) \qquad (1.17)$$

Where g(a) is the applied filter.

Finally, the back-projection of the filtered projections along the cone is performing with the weighting factor U, this will recover the original f(x,y,z) object function at the cartesian coordinates. Follow the reconstructed object formula for the cone-beam geometry.

$$f_{FDK}(x,y,z) = \int_0^{2\pi} \frac{1}{U^2}\, Q_\beta(\beta, a(x,y,\beta), b(x,y,z,\beta))d\beta \quad (1.18)$$

Where:

$$U(x,y,\beta) = \frac{Dso + x\sin\beta - y\cos\beta}{Dso} \quad (1.19)$$

1.5.2 – The algebraic/iterative algorithms

The class of non-Fourier domain algorithms is called algebraic algorithms. In simple terms, these algorithms make incremental adjustments to estimate the distribution of the linear attenuation coefficients, guided by the projection data (Beister et al., 2012). This is done iteratively computing the forward projections to estimate the reconstructed image. This kind of technology demands more computational processing power, leading to the use of parallel programming, especially the use of GPU (Graphics Processing Units), the large number of kernels accelerate the computational time of reconstruction, presently this alternative is gaining increasing evidence in the context of medical image (Eklundet al. 2013). This section focuses on the description of the SIRT (simultaneous iterative reconstruction technique) (Gilber P. 1972) and a variational technique commonly used to reduce noise, the total variation minimization (TV) (Rudin et al., 1992).

SIRT - Simultaneous Iterative Reconstruction Technique

Typically, an iterative method consists to solve a system of the linear equations with i unknown and j equations of the type A.S = p represented by

$$a_{11}S_1 + a_{12}S_2 + \ldots + a_{1i}S_j = p_1$$
$$a_{21}S_1 + a_{22}S_2 + \ldots + a_{2n}S_j = p_2$$

$$\begin{array}{cccc} . & . & . & . \\ . & . & . & . \\ . & . & . & . \end{array}$$

$$a_{i1}x_1 + a_{i2}\,S_2 + \ldots + a_{ij}S_j = p_m$$

where S is the image to be found, A is the projection matrix mapping the volume geometry onto the projection geometry, and p represents the projection data. In a practical context, it is impossible to solve $S = A^{-1}p$ for two reasons. First A is not an invertible matrix, and secondly, it is too large to compute. Looking to this situation as an optimization problem in practice, an iterative algorithm needs to find:

$$S^* = argmin_s \|p - AS\| \quad (1.20)$$

In practice, we try to find S* when the difference between the measured projection and a simulated projection(p) is minimal (residual projection or projection distance).

In the SIRT algorithm, the projection data is updated simultaneously in each interaction n, the new data after each iteration is defined by:

$$S^{(n+1)} = S^n + D_1\, A^T D_2\, (p - AS^n) \quad (1.21)$$

Where S^n is the projection at the n iteration. S^n is the initial forward projection of the S^n that is subtracted from the original projection and weighted by the sum of the superior diagonal matrix D2. A^T is the back projection applied to $D_2\,(p - AS^n)$ and weighted by the inferior diagonal matrix D1. Finally, this data set is updated by the sum with S^n, resulting in the $S^{(n+1)}$. Figure 1.10 shows the workflow of the application of the SIRT algorithm for the first interaction and figure 1.11 for the last iteration.

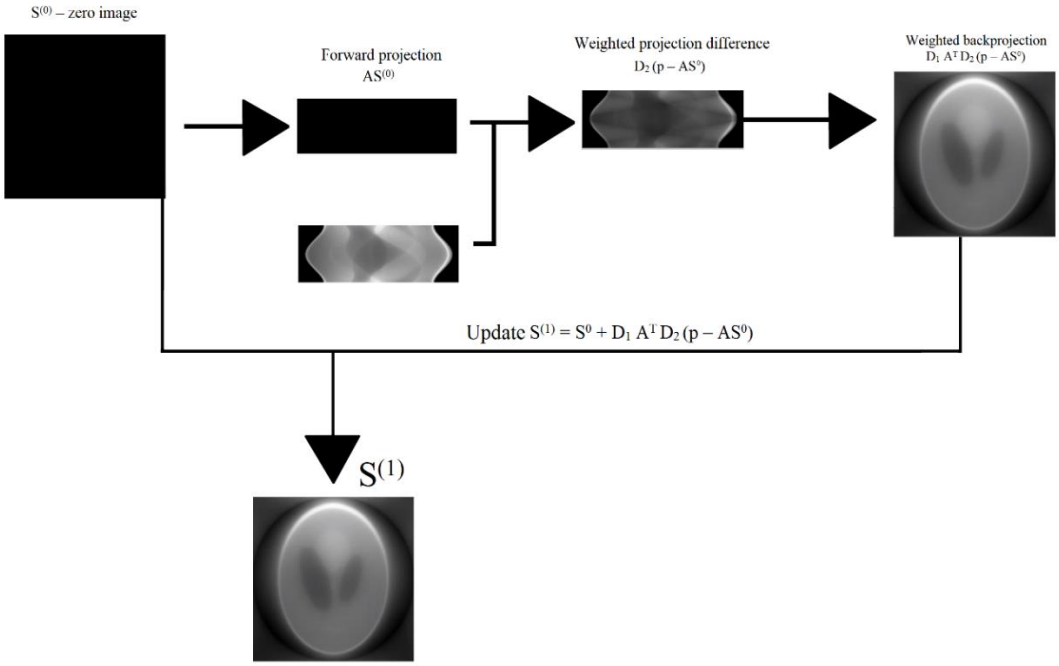

Figure 1.10: Workflow for the SIRT algorithm for the n = 1 iteration

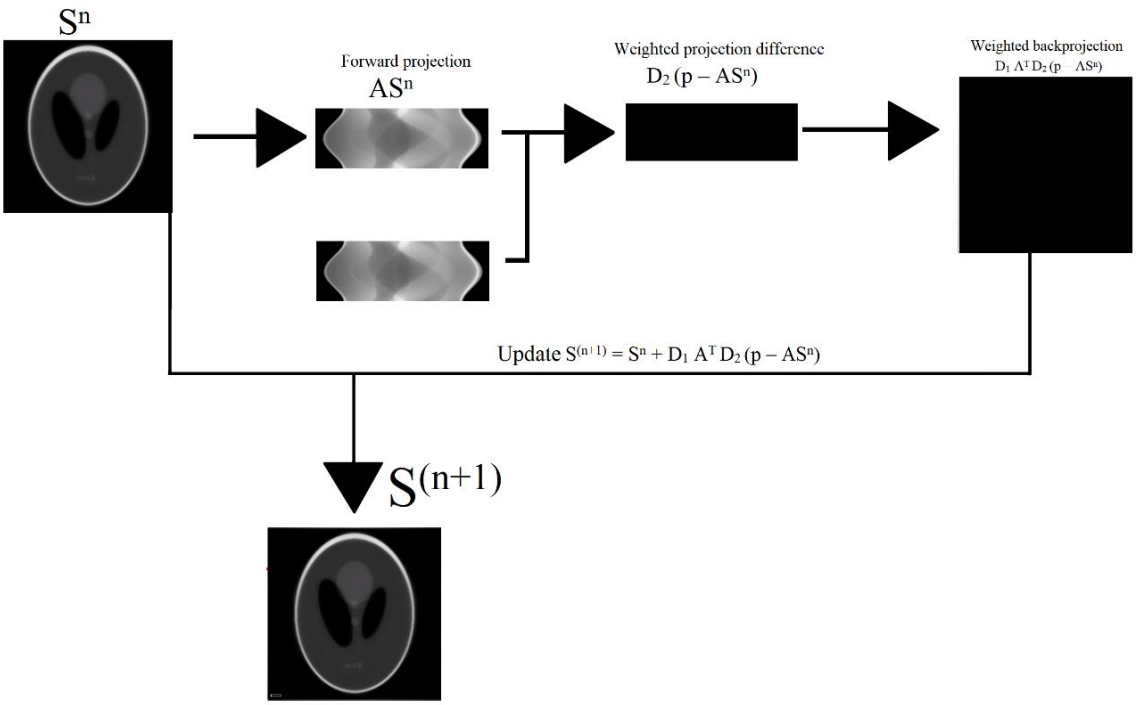

Figure 1.11: Workflow for the SIRT algorithm for the last iteration

1.5.2 – Optical-CT scanners

The laser OCT scanner was the first modality of CT scanner and was introduced by Gore et al in 1996 (Gore et al., 1996). It consisted of a He-NE laser as the light source

and the attenuated beam was detected by a photodiode. In this system, the source photodiode rotates over the sample. This reconstruction is made in parallel beam geometry to reconstruct the optical attenuation coefficient map. The main disadvantage of this kind of system is the time of scanning and reconstruction, which is an important feature for gels that can diffuse the information created by radiation at a given spot (Guo et al.,2006).

The parallel beam introduced to OCTs provide the 2D acquisition using a telecentric system to acquire the 2D transmission images. This geometry uses two convergent lenses, one to create the parallel beam from the point like light source and another to converge the transmission beam to CCD detector (Doran at al, 2009. Krstajic et al.,2006, Krstajic et al.2009. Wolodzko J et al 1999). The expensive cost of this OCT, specifically the convergent lens lead by Bache and collaborators (Bache el al. 2016) to develop a low-cost alternative, using the Fresnel's lens to create the parallel beam.

The cone-beam light source was motivated because they have fast acquisition projections using a CCD in their configuration to detect the attenuation beam. While the point detection laser to photodiode systems acquires point by point, the CCD cameras obtain a 2D projection at each scan angle to generate a transmission image projection along with all the samples, reducing the total scan time to the order of minutes. For this geometry, the simplest system is using a diffuse light source with the cone-beam acquisition by the CCD (Wolodzko et al., 1999). Based on this kind of OCT the company MODUS's QA developed a commercial system called VISTA10 and Olding in 2010 characterized the stray light contamination in the main signal, the major disadvantage for these types of scanners that use a diffuse light source (Olding et al., 2010).

Now, the development of OCTs is facing problems to have high performance, such as the cost, the large volume, the stray light contamination, and the vessels to perform dosimetry, also, the acceptation in the clinical context in the detection of the tridimensional absorbed dose (Doran at al., 2013). In chapter 2 we write about the development of the cone-beam OCT based on the convergent light source done in this thesis.

1.5.3 – Optical-CT image artifacts

Simon Doran published an illustrated guided showing how to perform OCT acquisition. The final reconstructed image in optical CT has some disadvantages and several details to consider in the acquisition for an image reconstruction (Doran et al., 2009). Here we present some examples of artefacts, such as: refraction, off-set position and non - monochromatic beam. These problems can be avoided in the acquisition process using some strategies.

Refraction loss data: Inside the water tank, often the gel is packed in a cylindrical vessel, so, there will be three different materials with different refractive indexes that will deviate the light from its original path. Figure 1.12A shows the transmission image presenting the loss of data because the refractive index mismatching. Adding a solution to the flask or to the water tank to increase the refraction index, matching both mediums, decreases this effect (Campbell et al., 2014, Rankine et al., 2013). To correct the loss data in figure 1.12A we found that the addition of sucrose in the water was an affordable and convenient procedure o adjust the refraction index to that of the gel minimizing light deviation.

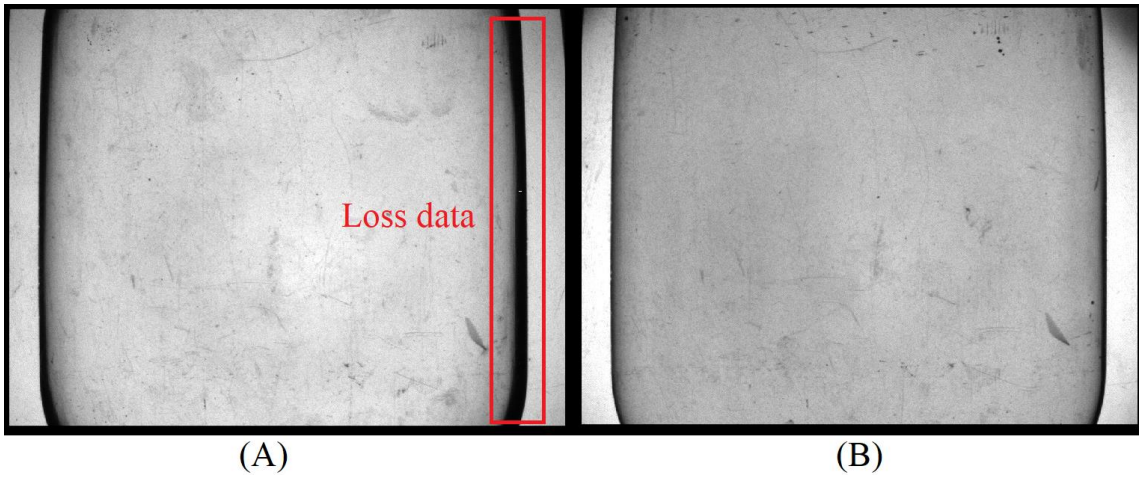

Figure 1.12: (A) Loss data image at the edges of the cylindrical vessel. (B) the loss data is minimized with the refractive index adjustment.

Offset image: The result of the offset artifact is clear in figure 1.14A, two edges to the same vessel are reconstructed (Chen and Li, 2013). To solve this problem, all OCT's components, camera, lens, water tank, and sample position needs to be recentralized to the optical axis. Another alternative is recentralizing the transmission image in the reconstruction code.

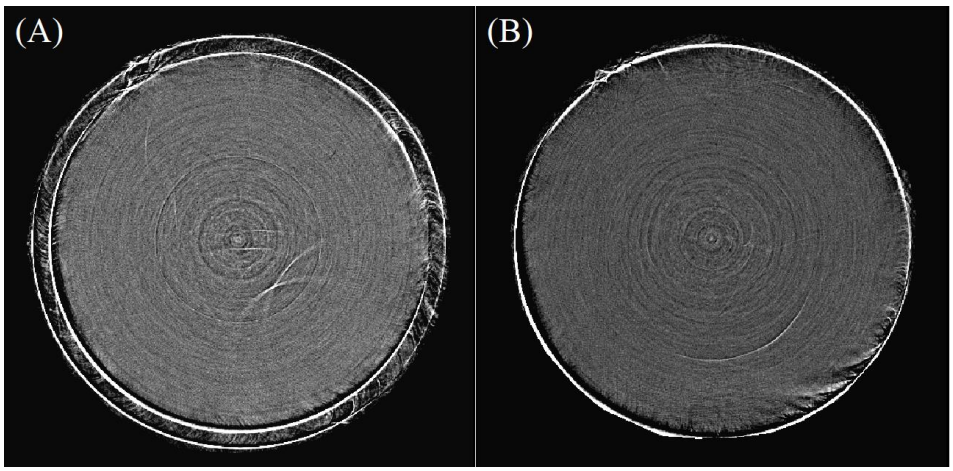

Figure 1.13: (A) Offset artefact. (B) Corrected offset artefact

Non-monochromatic beam: It is desired that the gel dosimeter and analyzed samples have the optical absorption in only one wavelength, however, this is not true in the nature of the substances. The result of this effect is different intensities in the reconstructed

image. The solution of this problem is to use a band-pass filter in the light source. Figure 1.14 shows this correction for the ARCOLOR® orange dye using a band pass filter of 545 ± 5nm.

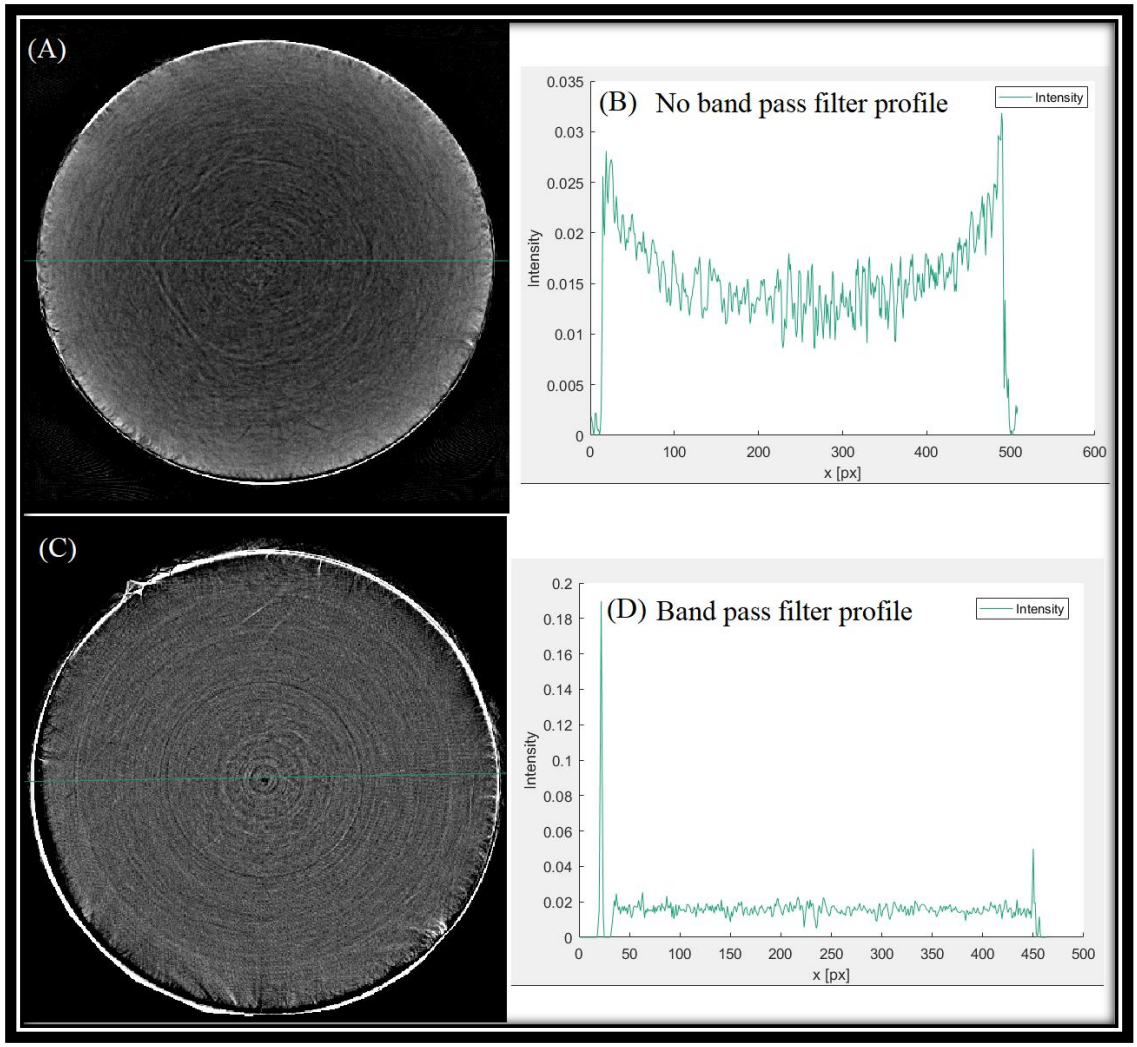

Figure 1.14: Reconstructed ARCOLOR orange dye: (A) Offset artefact. (B) Corrected offset artefact

1.6 – Objectives, motivation of research and thesis outline

Considering the demand of a truly 3D QA in clinical context this work has the main objective to build and characterize a Cone-Beam optical-CT (CBCT) to perform gel dosimetry for radiotherapy clinical planning. This also forced us to make the modification of the addiction of the formaldehyde in gel two gel dosimeters, FXO and TB, to have high melting points and become then useful in our temperature environment. Finally

combining this the OCT to modified FXO gel the 3D QA is performed in a craniospinal procedure.

Each chapter of this thesis is organized with the introductory section following to the development of the work and finalizing with the conclusion. At the end of each chapter, references are presented, each chapter is then self-consistent. In the following, we will give the main motivation and objectives of each chapter.

- Chapter 2: Here we present the results to construct and characterize the cone-beam optical-CT based on the convergent light source. The main motivation is performing the 3D dosimetry in the clinical context. To guarantee high quality images this chapter presents the optical and reconstruction characterization. The modulation transfer function (MTF) and stray light characterization are made for the transmission images. The best image reconstruction parameter was found using the FDK and SIRT-TV algorithm. The reconstructed attenuation coefficients maps are compared to measurements performed with a spectrophotometer to finally perform a percentage dose depth (PPD) dosimetry to compare to ionization chamber. The results in this chapter lead us to perform the 3D dosimetry in chapter 4.
- Chapter 3: The need to work with gel dosimeters in normal ambient temperatures led our group to investigate ways to increase the gel melting point that was achieved by adding formaldehyde in the gelatin matrix for the gel dosimeter. An initial investigation was made on the agarose matrix for the Turnbull-Blue gel dosimeter. This study was accepted in 2016 DosGel Conference and published in *Journal Physics: Conference Series* in 2017 (Silveira et al.,2017), titled as "*Characteristics of modified radiochromic gel Turnbull-Blue"* (doi:10.1088/1742-6596/847/1/012018) in this paper we found the improvement of the melting point from 33º to 55ºC for the Tb gel dosimeter. However, the idea to use agar as the gelling matrix was abandoned

because of the scattering in large flasks contaminating the transmission image. Motivated by these encouraging results, we change to gelatin as the matrix for the radiochemical's dosimeter. To solve the temperature problem, the addition of formaldehyde was made to FXO and TB gel dosimeters. The diffusion, autoxidation, auto reduction are important parameters to be determined to show the usefulness of these gels and they were characterized for FXO and TB, respectively. A high melting point was found for FXO and TB, and no energy and dose rate dependence was present in this gel dosimetry. Therefore, this paper was submitted to the *"Physics in medicine and Biology"* and now, after the referees' suggestions, the present author is revising the text to a resubmission.

- Chapter 4: This chapter presents the last work for this Ph.D. thesis, the clinical application. After the construction of the optical-CT and the gel dosimeter modification, the goals presented in chapter 2 and 3 lead us to perform the 3D dosimetry quality assurance in a complex dose distribution of multiple isocenter planning of a craniospinal procedure. The FXO – f was used as a dosimeter and the CBCT built was used to reconstruct the dose image. The measured dose using the optical CT was compared to TPS images. The results are following the literature and detected information that kind of procedure needs to be more rigorous.
- Chapter 5: In this last chapter is the conclusion of this PhD's thesis, presenting the goals of this work and the future perspectives the results lead.

References

Alexander, K. M., Pinter, C., Andrea, J., Fichtinger, G., & Schreiner, L. J. (2015). 3D Slicer Gel Dosimetry Analysis: Validation of the Calibration Process. World Congress on Medical Physics and Biomedical Engineering, June 7-12, 2015, Toronto, Canada, 521–524.

Attix F H 2004 *Introduction to radiological physics and radiation dosimetry.* Hoboken, NJ: Wiley-VCH.

Alva, M., Pianoschi, T., Marques, T., M, M. S., Baffa, O., & Nicolucci, P. 2010. Monte Carlo Simulation of MAGIC-fgel for Radiotherapy using PENELOPE. Journal of Physics: Conference Series, 250, 012067

Babic, S., Battista, J. & Jordan, K. Three-Dimensional Dose Verification for Intensity-Modulated Radiation Therapy in the Radiological Physics Centre Head and- Neck Phantom Using Optical Computed Tomography Scans of Ferrous Xylenol-Orange Gel Dosimeters. 2008. International Journal of Radiation Oncology - Biology - Physics 70, 1281–1291

Bache S, Malcolm J, Adamovics J and Oldham M 2016 Optical-CT 3D dosimetry using Fresnel lenses with minimal refractive-index matching fluid PLoS One 11 e0152606

Beister, M., Kolditz, D., & Kalender, W. A. (2012). Iterative reconstruction methods in X-ray CT. Physica Medica, 28(2), 94–108.

Brown, P. D. et al. 2017. Whole-Brain Radiotherapy for Brain Metastases: Evolution or Revolution? Journal of Clinical Oncology, JCO.2017.75.9589. Phys. Chem. 55483-7.

Baldock, C. 2009 Historical overview of the development of gel dosimetry: a personal perspective.. J. Phys. Conf. Ser. 56, 14–22.

Baldock C, De Deene Y, Doran S, Ibbott G, Jirasek A, Lepage M, McAuley, KB, Oldham, M., Schreiner, L.J., 2010. Polymer gel dosimetry. Phys. Med. Biol. 55 (5), R1–R63.

Chen, M., & Li, G. (2013). Forming Mechanism and Correction of CT Image Artifacts Caused by the Errors of Three System Parameters. Journal of Applied Mathematics, 2013, 1–7.

Campbell, W. G., Wells, D. M. & Jirasek, A. 2014 Radiation-induced refraction artifacts in the optical CT readout of polymer gel dosimeters. Medical Physics 41, 112102

De Deene Y, Walle R, Achten E, De Wagter C. 1998. Mathematical analysis and experimental investigation of noise in quantitative magnetic resonance imaging applied in polymer gel dosimetry. Signal Processing. 70:85-101.

De Deene, Y., Skyt, P. S., Hil, R. & Booth, J. T. 2015 FlexyDos3D: a deformable anthropomorphic 3D radiation dosimeter: radiation properties. Physics in Medicine and Biology 60, 1543

Doran, S. J. 2009 The history and principles of chemical dosimetry for 3-D radiation fields: Gels, polymers, and plastics. Applied Radiation and Isotopes 67, 393–398

Doran, S. 2013. How to perform an optical CT scan: an illustrated guide. Journal of Physics: Conference Series 444, 012004

Doran, S. J. 2017. Dosimetry using MRI: can it really be that di_cult? J. Phys.: Conf. Ser.847, 012051

Eklund, A., Dufort, P., Forsberg, D., & LaConte, S. M. 2013. Medical image processing on the GPU – Past, present and future. Medical Image Analysis, 17(8), 1073–1094. doi:10.1016/j.media.2013.05.008

Fricke H and Hart E, 1955, Chemical Dosimetry. In Radiation Dosimetry vol. 2 F.H. Attix and W.C. Roesch. Academic Press, New York

Feldkamp L A, Davis L C and Kress J W 1984 Practical cone-beam algorithm. J.Opt.Soc.Amer. 1 612-619.

Gambarini, G., Veronese, I., Bettinelli, L., Felisi, M., Gargano, M., Ludwig, N., … d' Errico, F. (2017). Study of optical absorbance and MR relaxation of Fricke xylenol orange gel dosimeters. Radiation Measurements, 106, 622–627.

Gedik, S., Tunc, S., Kahraman, A., Kahraman Cetintas, S., & Kurt, M. (2017). Comparison of 3DCRT,VMAT and IMRT techniques in metastatic vertebra radiotherapy: A phantom Study. EPJ Web of Conferences, 154, 01008.

Gilbert P. 1972. Iterative methods for the three-dimensional reconstruction of an object from projections. Jl Theor Biol;36:105e17

Gorjiara, T. 2011. Investigation of radiological properties and water equivalency of PRESAGE dosimeters. Medical Physics 38, 2265–2274

Guo, P., Adamovics, J. & Oldham, M. 2006. A practical three-dimensional dosimetry system for radiation therapy. Medical Physics 33, 3962.

Gore J C, Ranade M, Maryanski M J, and Schulz R J 1996 Radiation dose distributions in three dimensions from tomographic optical density scanning of polymer gels: I. Development of an optical scanner. Phys. Med. Biol. 41 2695-2704.

Getreuer P. 2012. Rudin–Osher–Fatemi Total Variation Denoising using Split Bregman. Image processing online library. http://dx.doi.org/10.5201/ipol.2012.g-tvd3

Grant, R., Ibbott, G., Yang, J., Adamovics, J., & Followill, D. (2013). Investigation of 3D dosimetry for an anthropomorphic spine phantom. Journal of Physics: Conference Series, 444, 012020.

Islam K T, Dempsey J F, Ranade M K, Maryanski M J and Low D A 2003 Initial evaluation of commercial optical CT-based 3D gel dosimeter Med. Phys. 30 2159–68

Instituto Nacional do Câncer, Estatísticas de câncer 2020, INCA, 2020.

Jordan, K. 2009. Optical CT scanning of cross-linked radiochromic gel without cylinder wall. Journal of Physics: Conference Series, 164, 012029. doi:10.1088/1742-6596/164/1/012029

Jordan, K. J., Hilts, M. & Jirasek, A. 2017. Optical and X-ray computed tomography scanning of 3D dosimeters. J. Phys.: Conf. Ser. 847, 012019

Kelly B G, Jordan K J and Battista J J. 1998 Optical CT reconstruction of 3D dose distributions using the ferrous benzoic-xylenol (FBX) gel dosimeter Med. Phys. 25 1741–50

Khezerloo, D., Nedaie, H. A., Takavar, A., Zirak, A., Farhood, B., Movahedinejhad, H., … Knuap, C. (2017). PRESAGE ® as a solid 3-D radiation dosimeter: A review article. Radiation Physics and Chemistry, 141, 88–97.

Krstajic N and Doran S J 2006 Focusing optics of a parallel beam CCD optical tomography apparatus for 3D radiation gel dosimetry Phys. Med. Biol. 51 2055–75

Krstajic, N. & Doran, S. J. 2007 Characterization of a parallel-beam CCD optical-CT apparatus for 3D radiation dosimetry. Physics in Medicine and Biology 52, 3693

Kak, A. C. & Slaney, M. 2001 Principles of Computerized Tomographic Imaging. SIAM.

Khan F M and Potish R A 1998 Treatment Planning in Radiation Oncology. Baltimore: Williams & Wilkins.

Khan, F. M. & Gibbons, J. P. 2014 The Physics of Radiation Therapy Fifth edition. LWW, Philadelphia, PA

Kron, T, Jonas D, Pope JM, 1997. Fast T1 imaging of dual gel samples for diffusion measurements in NMR dosimetry gels. Magn. Reson. Imag. 15, 211–221.

Kron T, Lehmann, J, Greer PB, 2016. Dosimetry of ionising radiation in modern radiation oncology. Phys. Med. Biol. 61 (14), R167.

Maryanski, M. J., Schulz, R. J., Ibbott, G. S., Gatenby, J. C., Xie, J., Horton, D., & Gore, J. C. 1994. Magnetic resonance imaging of radiation dose distributions using a polymer-gel dosimeter. Physics in Medicine and Biology, 39(9), 1437–1455

Maryanski, M. J., Gore, J. C., Kennan, R. P. & Schulz, R. J. 1993.NMR relaxation enhancement in gels polymerized and crosslinked by ionizing radiation: a new approach to 3D dosimetry by MRI. Magnetic Resonance Imaging 11, 253–258

Olding, T., Holmes, O. & Schreiner, L. J. 2010 Cone beam optical computed tomography for gel dosimetry I: scanner characterization. Physics in Medicine and Biology 55, 2819–2840.

Papadakis, A. E. et al. Technical Note: A fast laser-based optical-CT scanner for three-dimensional radiation dosimetry. Medical Physics 38, 830 (2011).

Quevedo, A. L., Borges, L. F., & Nicolucci, P. (2017). Avaliação da resposta do gel polimérico MAGIC-f modificado utilizando uma fonte clínica de braquiterapia e simulação Monte Carlo com o pacote PENELOPE. Revista Brasileira De Física Médica, 10(3), 2-6.

Rankine, L. & Oldham, M. 2013 .On the feasibility of optical-CT imaging in media of di_erent refractive index. Medical Physics 40, 051701 (2013).

Radon, J. Über die Bestimmung von Funktionen durch ihre Integralwerte längs gewisser Mannigfaltigkeiten. Berichte der Sächsischen Akademie der Wissenschaft 69, 262–277 (1917).

Rudin L.I. Osher S, Fatemi E., 1992. Nonlinear total variation based noise removal algorithms." Physica D, vol. 60, pp. 259 – 268.

Schreiner LJ, 2004. Review of Fricke gel dosimeters. Journal of physics: Conference Series. 3. 9-21

Sharpe, J. et al. Optical Projection Tomography as a Tool for 3D Microscopy and Gene Expression Studies. Science 296, 541–545 (Apr. 19, 2002).

Smith, S. T., Boase, N., Masters, K. S., Hosokawa, K., Asena, A., Crowe, S. B., … Trapp, J. V. 2019. A very low diffusion Fricke gel dosimeter with functionalised Xylenol orange-PVA (XOPVA). Physics in Medicine and Biology.

Solc. Spěváček V., 2009. New radiochromic gel for 3D dosimetry based on Turnbull blue: basic properties. Phys. Med. Biol. 54, 5095–5101.

Thomas, A. & Oldham, M. Fast, large field-of-view, telecentric optical-CT scanning system for 3D radiochromic dosimetry. Journal of Physics: Conference Series 250, 012007 (Nov. 1, 2010).

Wolodzko, J. G., Marsden, C. & Appleby, A. CCD imaging for optical tomography of gel radiation dosimeters. Medical Physics 26, 2508 (1999).

Webb S. 2003. The physical basis of IMRT and inverse planning. Br. J.Radiol. 76 678-689.

Vanneste, B. G. L., Van Limbergen, E. J., van Lin, E. N., van Roermund, J. G. H., & Lambin, P. (2016). Prostate Cancer Radiation Therapy: What Do Clinicians Have to Know? BioMed Research International, 2016, 1–14.

Van Gompel, G., Van Slambrouck, K., Defrise, M., Batenburg, K. J., de Mey, J., Sijbers, J., & Nuyts, J. 2011. Iterative correction of beam hardening artifacts in CT. Medical Physics, 38(S1), S36–S49.

Yu C X 1995 Intensity-modulated arc therapy with dynamic multileaf collimation: an alternative to tomotherapy. Phys. Med. Biol. 40 1435-1449.

Zelefsky, M. J., Fuks, Z., Hunt, M., Yamada, Y., Marion, C., Ling, C. C., … Leibel, S. A. (2002). High-dose intensity modulated radiation therapy for prostate cancer: early toxicity and biochemical outcome in 772 patients. International Journal of Radiation Oncology Biology Physics, 53(5), 1111–1116.

Chapter 2 - Development and evaluation of a large volume optical CT scanner based on a convergent light source

2.1 - Introduction

Optical computed tomography (CT) images of radiochromic gel dosimeters provide information about the attenuation coefficients characteristics related to their absorbed dose distribution. The measured dose distributions can be evaluated by comparisons with treatment planning system (TPS) dose distributions images (Doran and Krstajić, 2010). This dosimetric system, including a radiochromic dosimeter and an optical CT, can be applied to radiotherapy tridimensional quality assurance (QA) (Baldock et al., 2010). In the past decades, several authors studied different beam geometries and light sources to acquire the optical sinogram to produce the optical CT images: Gore et al. proposed a single laser beam that scanned the sample using a galvanometer mirror, and after emerging from the volume, it was detected by a photodiode (Gore et al., 1996), then, Maryanski et al. (2001) proposed a microbeam version for this setup. Parallel beam provided by a telecentric system lens detected by CCD camera was proposed by several groups (Doran et al.,2001, Van Doom et al.,2005, Thomas et al., 2010, Krstajić,2007a, 2007b), and a low-cost version for this apparatus was made using Fresnel Lens (Bache et al., 2016). Campbell and Jirasek developed an optical CT based on a laser fan beam detected by photodiodes (Campbell et al.,2013). A diffuse light source combined with cone-beam acquisition using a CCD camera was proposed by Wolodzko (Wolodzko et al., 1999), and it became commercially available as a simple and fast acquisition system by the company Modus QA as VISTA^{TM} (Jordan and Batista, 2006). This scanner was characterized and it was verified the presence of

stray light contaminating the acquired signal (Olding et al. 2010,2011). Recently, the cone beam with a converting light source with a narrow beam was made available to purchase from Modus QA commercial cone-beam CT (Dekker et al., 2018), with the original light source's replacement by a point light source to reduce stray light.

Different alternatives were presented in the literature for suppressing stray light contamination. First, a grid matrix with small holes can be used to subtract the stray light signal from the projection (Olding et al.,2011, Granton et al., 2016). Second, the determination of point spread function (PSF) and its use in the signal processing to reduce the glare in transmission images (Thomas et al, 2011). Third, the use of a point light source combined with a Fresnel lens (Dekker,2016). This last option has a convergent light beam to a CCD camera and was demonstrated to be practical and effective in suppressing stray light in the optical CT transmission images.

To improve the reconstruction quality in x-ray CTs, authors have implemented iterative algorithms to remove noise and artifacts. This alternative reduces the delivered dose and improves the signal's quality. Some examples of these algorithms are the simultaneous iterative reconstruction technique (SIRT), simultaneous algebraic reconstruction technique (SART), and ordered subset convex (OSC) (Beister et al, 2012). Also, the total variation denoising (TV) combined with the presented algorithms demonstrate a powerful tool to remove noise (Rudin et al, 1992). Improving the reconstruction code demands more time processing which required their implementation in parallel processing using the power of GPU (Graphics Processing Unit) because of the large number of processors. This computation strategy of the final image has been implemented in the optical CT context. For example, the use of SART-OSC-TV to DESK3d, an educational optical CT build by Modus QA (Metanine et al., 2015), and OSC-TV to radiochromic samples and dye gel dosimeters (Deeker et al.,2017). This

implementation reported good results on the determination of attenuation coefficients related to the absorbed dose.

Based on recent publications of stray light reduction and high-quality reconstructions in optical CT, this study will provide a complete description of the construction and characterization for a cone-beam optical CT with a convergent beam provided by a point light source and a Fresnel lens directing the optical rays to a CCD camera to acquire transmission images. We used the simplest instrumentation possible without compromising the results' quality, combining Arduino's power of automation with the image processing library of Matlab (https://www.arduino.cc/). The optical acquisition was made by calculating the MTF (modulation transfer function), and the stray to the primary ratio (SPR) was calculated. SIRT algorithm was used to compute our reconstructions because it is the most straightforward iterative technique. The total TV was to implement in our code to remove noise and improve the contrast; they are referred to as SIRT-TV from now and GPU parallel processing was also used to load, reconstruct and process acquired images to reduce computation time significantly. The contrast to noise ratio (CNR) was calculated for the standard algorithm for cone-beam CT, Feldkamp, Davis, and Kress (FDK) algorithm, and SIRT-TV to find the best regularization parameter in TV denoising. Finally, the optical-CT performance upon radiation dosimetry was verified by comparing the percentage dose depth (PDD) measured with the gel dosimeter to the ionization chamber measurement.

2.2- Materials and methods

2.2.1 - Cone-beam optical-CT(CBCT)

The optical CT built was based in four main parts: camera for the image acquisition; the water tank to be filled with a refractive index matching solution with the phantom; step motor to rotate the sample; and the light source to produce the convergent beam.

Camera

The astronomic monochromatic camera ASI120-S ZWO was chosen to acquire the sample's transmission image. This device has the CMOS AR0130CS 1/3" sensor (4.8mm x 3.6 mm) with a 12bit ADC and 3.75µm of pixel size. In this camera, resolutions from 640 x 480 up to 1280 x 960 pixels are available. Therefore, we analyzed projections acquired with images at 640x480, 800 x 600, and 1080 x 720 pixels of resolution to perform fast reconstructions. An optical system is coupled to the camera with a 5 – 50 mm varifocal lens to have an optical zoom, manual exposure, and focus regulation.

Water tank

The water tank function is to fill the phantom's surroundings with an adjusted refractive index liquid to avoid distortions or loss of information in the reconstructed images due to the vials' interface. It was constructed using acrylic sheets with 25 x 25 x 30 cm^3, resulting in a maximum capacity of 18.75 liters. The illuminated tank faces had a thickness of 1 mm to avoid large deviations of the light rays at these interfaces. The cleaning of the water tank and the liquid is of paramount importance because every dirt in the light path can cause artifacts and distortions in the images. In the center of the water tank, there is a system consisting of a circular small platform and a screw for holding and positioning the simulating objects.

Step motor

The step motor used follows the national NEMA 16 standard protocol, being a unipolar six-wire motor. Each step of this motor takes the displacement of 1.8 ° for full

pitch and 0.9° for half-pitch. Thus, a full 360° turn results in 200 projections and 400 projections, respectively. This pattern would limit reconstructions of 200 x 200 pixels and 400x400 pixels images, accordingly to Kak and Slaney (Kak and Slaney, 1999), which stated that to reconstruct N X N images (N is the number of pixels), it is necessary, at least, that the same number N of projections. Two resolution options for the reconstructed images were possible using a set of gears coupling the stepper motor to a larger disk. This system allows each step of the engine to be 0.25 ° on the largest disk, where the sample will be positioned. Therefore, for a complete revolution (360°), steps of 1°, 0.5°, 0.25°, and 0.125° can be obtained for acquiring a total of 360, 720, 1440, and 2880 projections, respectively. Thus, theoretically, it would be possible to reconstruct images up to 2880 x 2880 pixels depending on the computational power.

Automation - Arduino + Matlab

The automation of the pitch motor synchronized with the camera was done using the Arduino® UNO microcontroller. In this study, we combine the power of image processing and acquisition of Matlab with the control and automation functions of Arduino. This combination provided the optical CT fast acquisitions of transmission images along with the total engine rotation.

Light source

A 3W LED fixed in a cylinder of 1.5cm diameter with a diffuser was used to build a convergent light source. It was positioned before the focus (25 cm) of the acrylic Fresnel lens (20 cm x 20 cm), typical of an overhead projector, to create the convergent beam to the camera. An optical filter with 545 nm and a bandwidth of ± 5 nm was used to select the wavelength. The complete scheme of the optical CT is shown in figure 2.1.

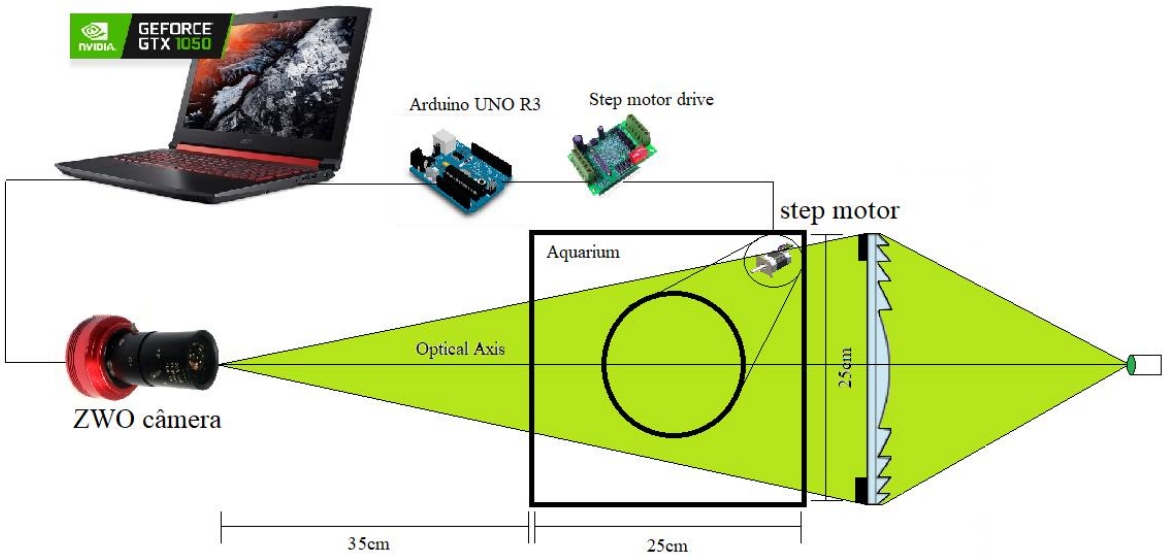

Figure 2.1: Complete scheme of our optical CT showing the light source at right, the light rays (green shaded area), the Fresnel lens, the tank with the phantom in the rotating platform, and the CCD camera.

2.2.2 - Materials descriptions

Dyes

- ARCOLOR orange dye - 545 nm wavelength peak

This solution is a commercial food dye commonly used in gelatin. For this study, it was diluted in deionized water.

- Carbon black powder(CB) – 30 nm

The carbon black powder is diluted in deionized water with 5% of hydrogen peroxide to avoid the formation of a precipitated of carbon particles.

Scatter

- Leite de Rosas® (LDR)

Leite de Rosas® is the commercial name of the zinc oxide immersed in an alcohol solution. translating to English the name may be roses milk. This light scattering solution presents an appearance e close to milk diluted in water with the advantage of being stable and inert.

Gel dosimeter

- FXO–f: Fricke – Xylenol - Orange with formaldehyde gel dosimeter

FXO–f is the gel dosimeter chosen for the PDD measurement. Its preparation follows the same steps as in Kelly et al. 1998, differing only in the addition of formaldehyde to gelatin before the original chemicals, resulting in 3%W/W of this cross-linker in the total dosimeter's volume.

2.2.3 - Optical evaluation – MTF/ spatial frequency evaluation

MTF calculation was evaluated from optical patterns printed from the Norman Koren website (http://www.normankoren.com/Tutorials/MTF2.html) to analyze the optical power of the optical CT geometry. The pattern was printed in a celluloid overhead transparency and positioned at the optical CT front wall with a 35 cm distance from the camera. Three resolutions were evaluated: 640 x 480, 800 x 600, and 1024 x 780 to verify if the change of the total number of pixels would decrease the performance in terms of spatial resolution and contrast. The comparison was made by extracting the spatial frequency from the Norman Koren chart data file and comparing it with the spatial frequency acquired on the same region by the camera positioned in the CBCT. The calculation of MTF was performed by the script available to download from the normankoren same website. This script was modified just to load our Matlab data files to perform MTF calculations.

2.2.4 – Stray light characterization

Stray light contamination signal is one of the most enemies of optical-CT image reconstruction, resulting in loss of contrast information. To find the stray light contribution in the total signal acquired in the developed CBCT the stray-to-primary ratio (SPR) was calculated for different substances. They were placed in a cylinder with 15 cm diameter and 12 cm tall placed inside the water tank filled with water. This evaluation

was made with different substances: water, a uniform scatter solution (water and an oily perfume - LDR), porcine gelatin, and uniform orange organic dye solution (ARCOLOR®). Two images were taken from the analyzed samples to calculate the SPR. The first image was a single transmission picture of the substance. The second image was the same as the first one, but using a square grid of small holes, with 5 mm diameter and spaced by 1 cm centimeter, positioned in front of the water tank facing the camera. The first image has the primary ray plus the stray light contribution, and inside the holes of the second image, only the primary ray. To find only the stray light contamination, the second image was subtracted from the first image. Then, at the holes' region, the mean intensity of the stray light and the primary ray were calculated to finally find the SPR.

2.2.5 – Reconstruction evaluation – FDK and SIRT-TV

First CBCT reconstructions were performed using a standard cone-beam filtered back projection, FDK algorithm (Feldkamp et al. 1984) with a Hamming filter, implemented in Matlab. The FDK images reconstructed has noise and small artifacts. This problem forced the implementation of SIRT and TV. With the SIRT algorithm (equation 2.1) reconstruction starts with a zero image (S^0) and converges to the original (S^n) (with noise and artifacts) in a number of n iterations. Therefore, n was chosen to achieve an improved image, minimizing the $p - AS^n$, factor in equation 2.1, before converging to the original with noise and artifacts.

$$S^{(n+1)} = S^n + D_1 A^T D_2 (p - AS^n) \quad (2.1)$$

Where S^n is the image at the n^{th} iteration, which, starts with a zero matrix S^0. The term AS^n ,the initial forward projection(A)apllied to S^n , subsequently is subtracted from the original projection matrix (p) to be weighted by the sum of the superior diagonal matrix D2. The term A^T is the back projection applied to matrix $D_2 (p - AS^n)$ and weighted by the inferior diagonal matrix D1. Finally, this set is updated by the sum with reconstruction

S^n, resulting in the $S^{(n+1)}$ reconstruction. To find the best value of iteration n, we used the (CNR) as μ/σ, where μ is the mean of the attenuation coefficient in a region of interest inside the center of the reconstructed image and σ is the standard deviation attributed to the noise in the same region of interest (ROI). This algorithm was combined with TV denoising to reduce noise amplitude (Equations 2.2 and 2.3) applied to final image S from SIRT. The TV algorithm used in this study is based on the Rudin-Osher- Fatemi algorithm - ROF (Rudin et al,1992) given by the equation:

$$S_{(m+1)} = S_m + \lambda S. \quad (2.2)$$

The term λ is the regularization parameter that minimizes noise on image S. After the total variance was shown calculated equation 2.3

$$TV(S) = \iint \sqrt{\left(\frac{\partial S}{\partial x}\right)^2 + \left(\frac{\partial S}{\partial y}\right)^2}\, dxdy \quad (2.3)$$

The result after the number m of interactions is an image suppressed from noise. We found the best λ, the regularization parameter, by calculating the contrast to noise ratio (CRN) as done in the SIRT process. This procedure will avoid destroying edges and losing signal and spatial resolution in dosimetric images.

2.2.6 - Absorbed samples reconstruction evaluations.

Uniform solutions were evaluated using the same 15 cm diameter and 12 cm tall jar. The CBCT's water tank was filled with water. Pre-scan was performed with a jar filled with 8% sucrose solution inside the vessel. Post-scans were performed using different concentrations of 30 nm carbon black solution in a 2 liters' cylinder volume. Concentrations of 2.5, 3.5, 4.5, 5.5, 6.5, and 7.5% were evaluated.

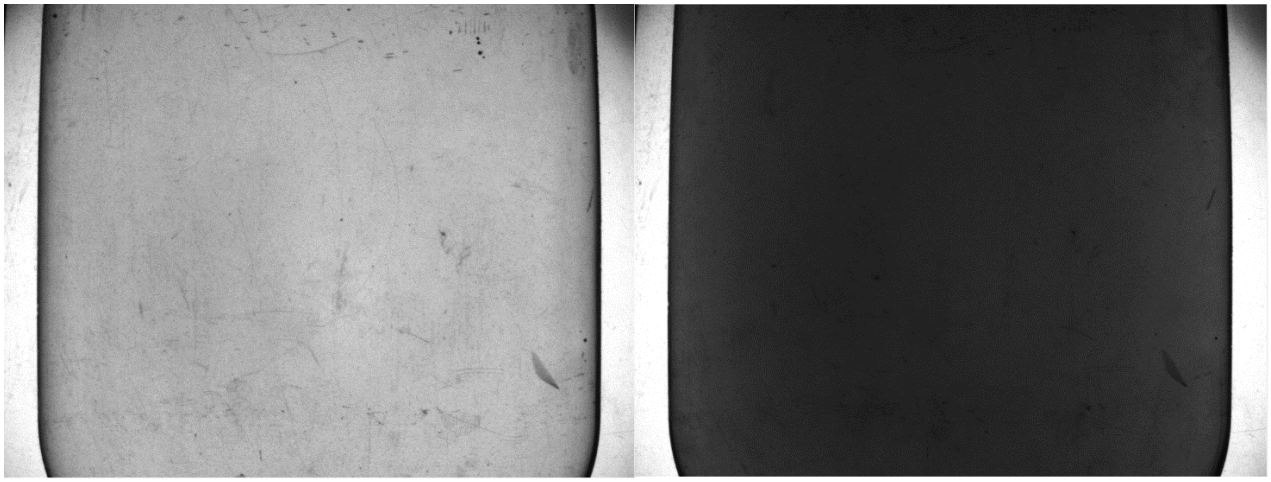

Figure 2.2: a) Pre-scan:15cm jar filled with 8% sucrose solution; b) Post-scan filled with 7.5% of carbon black solution.

2.2.7 - Uniform finger distributions evaluations.

In this set of experiments, we describe reconstructions of different concentrations with uniform fingers of gelatin combined with carbon black nanoparticles distributed along 15 cm cylindrical vessels. The concentrations used were 1.0, 3.0, 4.5, and 6% for the first cylindrical phantom and 2.5, 5.0, 7, and 8% for the second. The attenuation coefficients were determined by the CBCT and a Ultrospec® 2100 pro spectrophotometer. Reference scan (pre-scan) images were acquired using the cylindrical vessel filled with 8% gelatin concentration. The post-scan was made using the same vessel, but after total gelatin melted, small regions were filled with gelatin and carbon black nanoparticles with different concentrations. To compare the attenuation coefficients determined by the CBCT and spectrophotometer, the same concentrations of finger distributions were filled in a small cuvette of 4 ml volume. This set of reconstructions were made with the same SIRT-TV parameters used in a large sample of uniform absorbed solution. For this section, the CNR was calculated to verify the best reconstruction parameters.

2.2.8- Uniform scatter solution evaluation

Reconstruction performance for scattering solutions was determined using the same set of uniform absorption solutions, the aquarium was filled with water, and the 15 cm vessel

was filled with 8% sucrose solution. Post-scans solutions were made using different concentrations of a commercial parfum, a rose extract diluted in alcohol, and zinc oxide (Leite de Rosas-LDR) that presents a scatter behavior. A DLS measurement shows the compound has two major size distributions, particles with 1588 ± 41nm and 390 ± 31nm of diameter are responsible for the scattering of light. The reconstructions for this scatter solution were performed using the parameters determined in the absorption solutions. To evaluate the scatter attenuation coefficient in our CBCT, 0.5, 1, 2, and 4% uniform solutions were imaged and sequentially reconstructed.

2.2.9 – PDD 5x5 cm^2 dose distributions of a Fricke xylenol orange gel dosimeter.

A 15 cm diameter and 12 cm tall cylindrical jar filled with modified FXO (Fricke xylenol orange) gel dosimeter by the addition of formaldehyde was prepared. The jar was positioned at 100 cm of SSD (source-sample-distance) and irradiated using a 6 MV Linear accelerator (Primus, Siemens Medical). The dose at the depth of the maximum dose of the PDD was 2.5 Gy and a square field size of 5 x 5cm². The acquired images showed a very dark region. Thus, the exposition time was leveled up, and a parabolic compensator was positioned between the light source and the Fresnel lens to eliminate the saturated pixels in the regions outside the cylindrical object (Dekker et al, 2018). For the acquisition of the irradiated phantom images, the camera was set to 1024 x 768 pixels in high resolution, the varifocal lens was set to 50 cm focal distance, CBCT aquarium was filled with water to minimize refraction interference, and 720 projections were acquired around 360º rotation, resulting in a step rotation of 0.5º. The reconstruction protocol used was FDK as the first reconstructed image, and then we applied the SIRT-TV algorithm with the best parameters determined in previous sections. Finally, by determining the absorbed dose relation to the attenuation coefficient, the dose resolution was calculated using a confidence level of 95% (Baldock et al, 2010).

2.3 – Results and discussions

2.3.1 - Optical analysis results – MTF/spatial frequency

Three images with 0.3x0.3 mm² pixel size were evaluated to confirm the power of the camera to detect contrast and spatial resolution. Figure 2.3 shows the acquired signal from the picture template made from normankorean.com. The optical CBCT MTF was evaluated for 1024 x 768, 800 x 600 and 640 x 480 image sizes (figure 2.4).

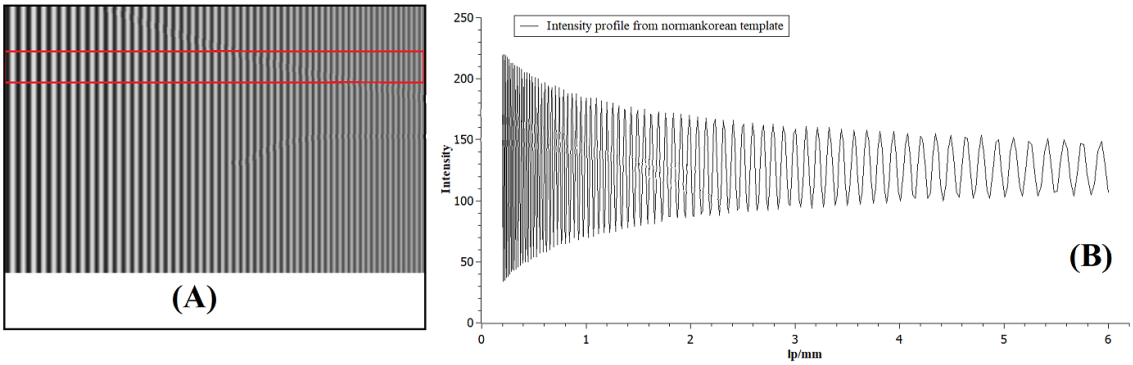

Figure 2.3: (A) Variable space-frequency pattern downloaded from normankoren.com template used to determine the modulation transfer function. (B) The brightness (intensity in nit numbers) of the image inside the red box in the upper part of image A is shown in B versus the spatial frequency in the number of lines per millimeter (1p/mm).

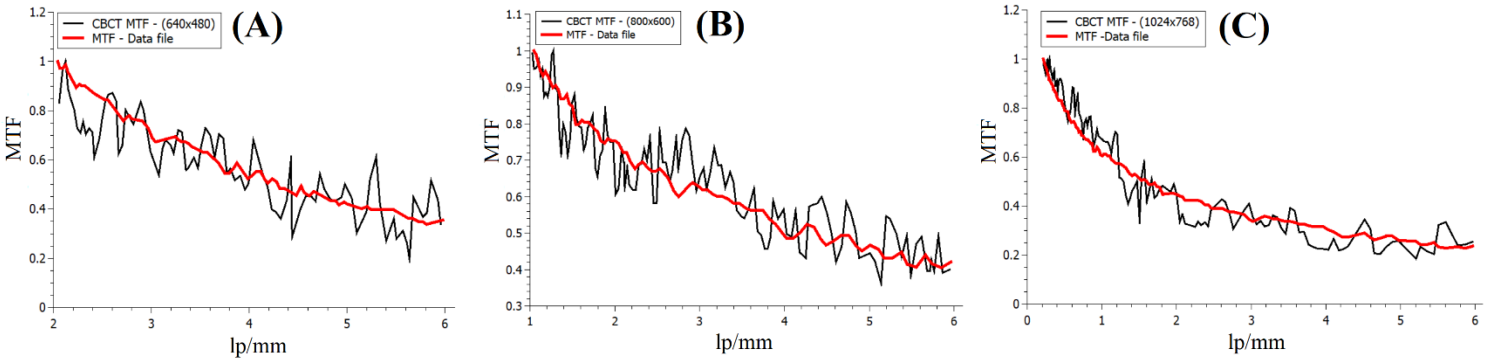

Figure 2.4: Modulation Transfer Function for the images with different sizes:(A)600x480 (B)800x600 (C)1024x768. The red line shows the theoretical values, and the black line the experimental results obtained in this study.

The data file's MTF/spatial frequency and the acquired signal is finishing at 6lp/mm highest spatial frequency. The Scattered points were attributed to print quality and moiré

effect in the transparency slides. We found 75%, 60% and 65% before converging to 100% (0 of MTF) for 1024x768, 800x600 and 640x480 resolutions for our camera combined with varifocal lens 5-50cm. These results are superior to the depth field criteria of 50% of maximum template image contrast (Kak and Slaney 1998). This data confirms that our optical camera system is adequate to perform projection acquisition for the CBCT.

2.3.2 – Stray light characterization

Table 1 shows the stray to the primary ratio (SPR) to the tested solutions: water, orange dye (ARCOLOR®), LDR as scattering, uniform 4.5% carbon black solution (CB4.5%), and non-irradiated ferrous xylenol orange with formaldehyde gel dosimeter (FXO-f).

Table 2.1: Stray to primary ratio (SPR) for the tested solutions

Chemical solution	**SPR**
Water	0.01 ± 0.02
ARCORLOR	0.08 ± 0.03
LDR	0.09 ± 0.03
CB	0.06 ± 0.02
FXO-f	0.07 ± 0.04

For different solutions tested, the SPR shows less than 10% of the acquired signal represents the stray light contamination. This behavior justifies the great accordance with spectrophotometer measurements in uniform absorption samples and finger phantoms. We attributed this SPR ratio to a small point light source combined with the Fresnel lens that results in the convergent beam to the camera. This ratio may be smaller in future studies because the vessel was not optimized to perform optical CT. Our group plan to

explore other strategies to suppress this type of stray light source, for example, mathematical models like point-spread-function (PSF) and high-quality Fresnel lens.

2.3.3 - Uniform absorbed solutions

The uniform reconstructions of absorbed solutions imaged from a 15 cm cylinder vessel with different carbon black concentrations were used to determine the best parameters to SIRT combined with TV. Figure 2.5 shows the profile of the pre-scan solution and the 7.5% carbon clack solution as post-scan. This profile shows the decrease of light signals across the vessel. Figure 2.6 shows the reconstruction images of the uniform carbon black solution comparing the FDK and the SIRT-TV optimized parameters. This reconstruction presents a homogenous profile where noise and small ring artifacts were suppressed in the reconstructed image.

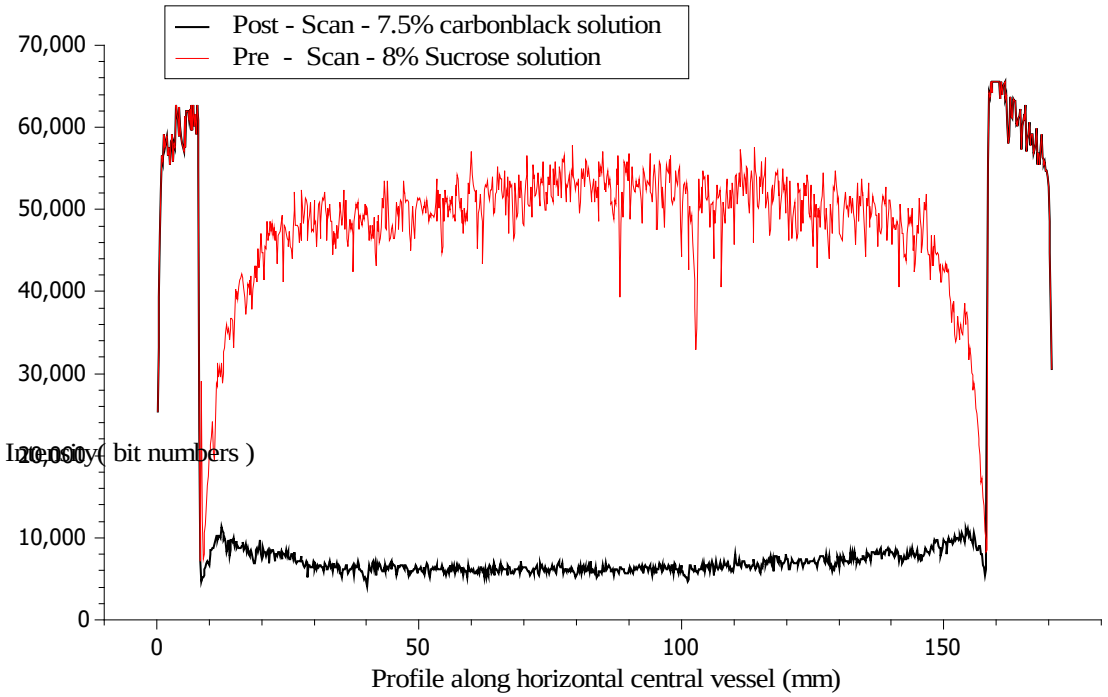

Figure 2.5: Comparison between pre-scan (red line) and post-scan profile (black line).

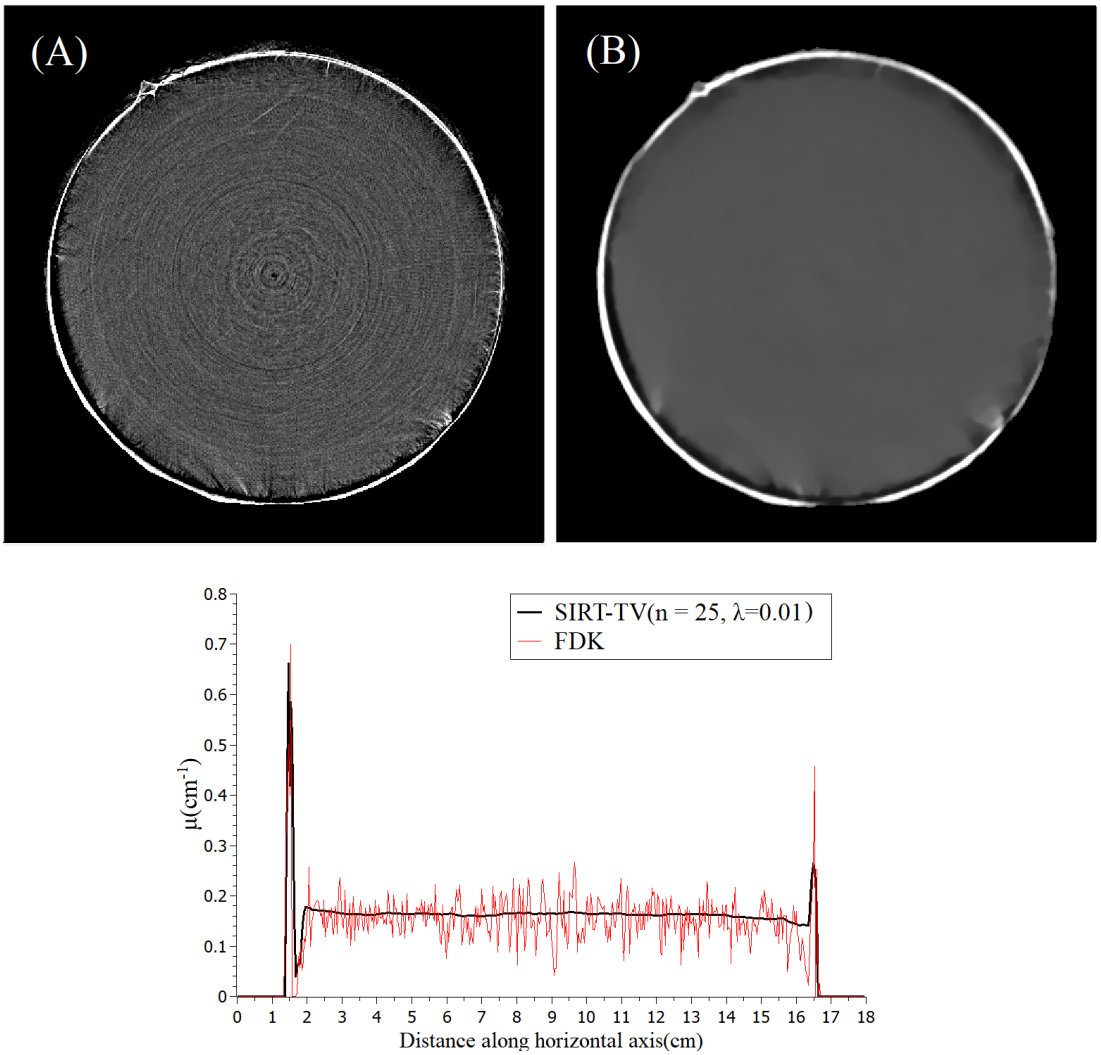

Figure 2.6: Reconstructed image A) 7.5% carbon black solution using the FDK algorithm. B) SIRT-TV, n= 25, λ=0.01. C) Comparison between horizontal profile to FDK versus SIRT-TV.

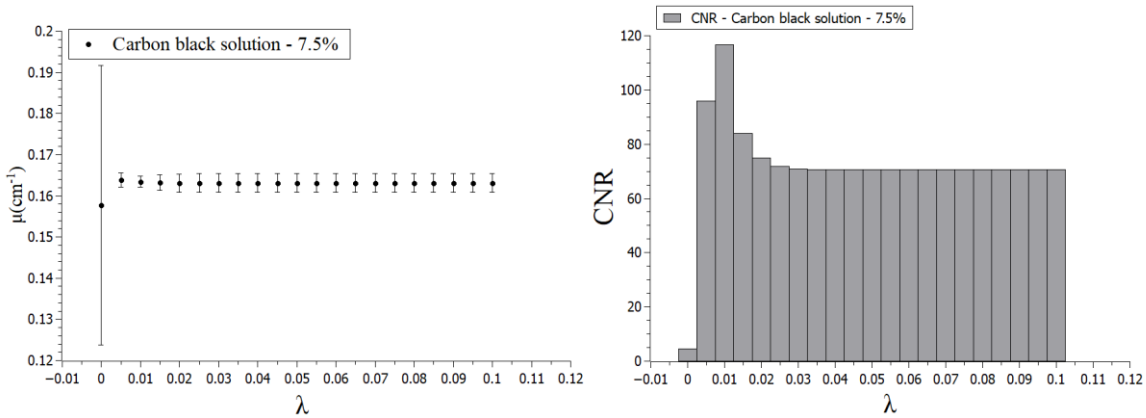

Figure 2.7: Attenuation coefficient for the 15cm cylinder diameter with 7.5%carbonblack solution (A) Plotted to present the average value in ROI versus λ. (B) CNR histogram versus λ, present best CNR at λ=0.01

Figure 2.7A presents the attenuation coefficient determined inside an ROI of the 15cm cylinder jar. It is clear that the SIRT-TV algorithm suppresses noise in the uniform solution and can be visualized by the decrease in the error bars. To find the best regularization parameter λ, figure 2.7B shows the CRN from $\lambda = 0$ to $\lambda = 0.1$; the best parameter found was 0.01. For higher λ values, the CRN is decreasing while noise is suppressed. However, the regularization parameter became aggressive to signal images, destroying the edges and diminishing contrast.

Figure 2.8 shows a group of reconstructions for a solution of carbon black with different concentrations, namely: 2.5, 3.5, 4.5, 5.5, 6.5, and 7.5%, filling the 15 cm jar and reconstructed with the following parameters: $n = 25$ interactions and $\lambda = 0.01$. In figure 2.9A, the profile along the central axis shows a homogenous intensity with small fluctuations when comparing the FDK reconstructions. Probably this small fluctuation is originally from some non-uniformity on the vessel walls, and this can cause systematic noise on the reconstructions. In this study, a common plastic vial was used, which was not an optimized vessel. The idea was to show the system's performance with ordinary plastic vials that could be easily found and discharged after use. The linear behavior for this study is shown in figure 2.9B with the equation $\mu = 2.41.10^{-2} + 4.66\ 10^{-2}$ with $R^2 = 0.996$. This result is important because 3D reconstruction in optical CTs' contrast is related to attenuation coefficient, originally from chemical concentrations, therefore, when the attenuation coefficient of the same material is determined by a spectrophotometer the result needs to agree, at the least, the same linear behavior. The next section will present this evaluation comparing the results obtained with the optical CT to the ones obtained with a commercial spectrophotometer.

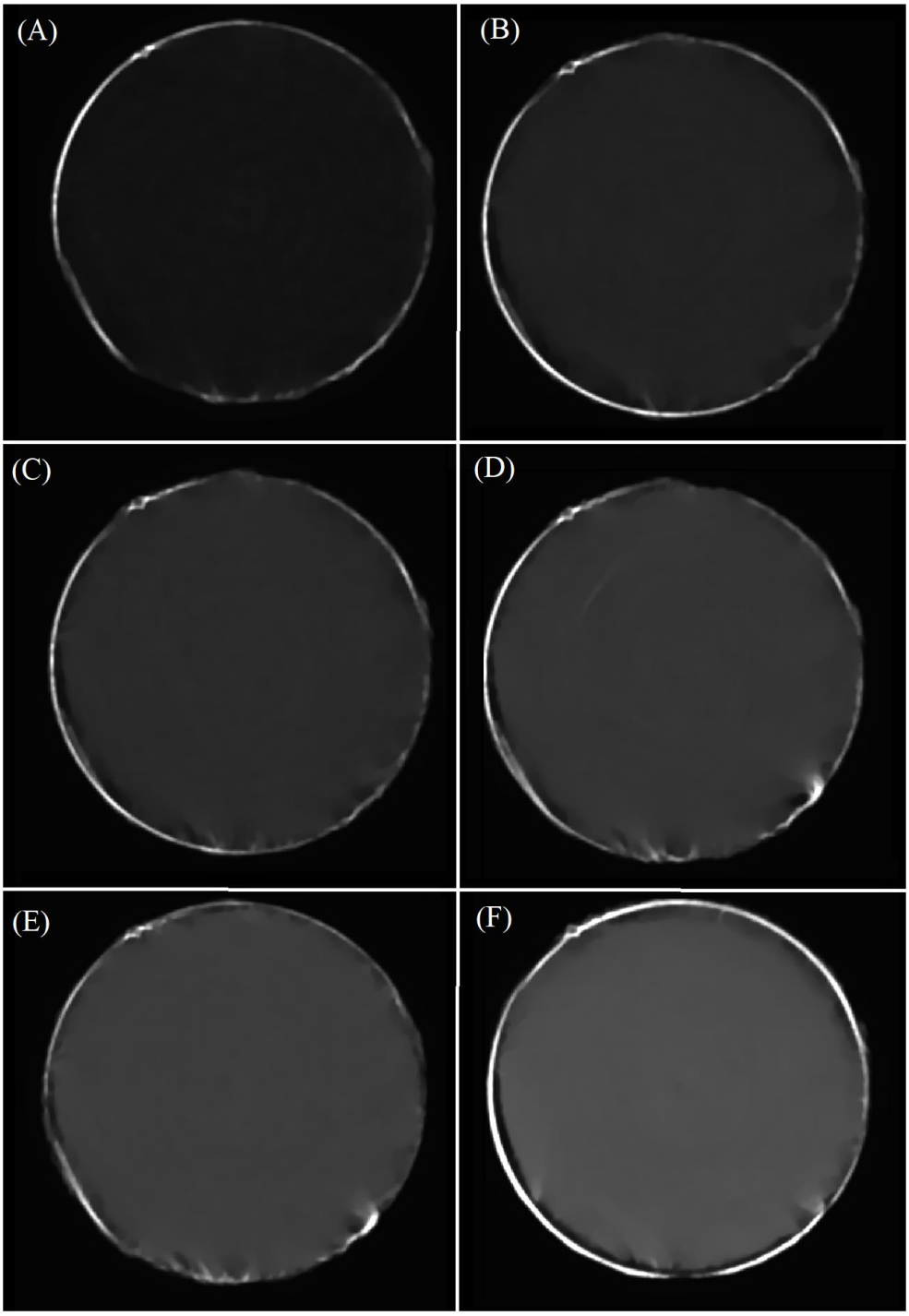

Figure 2.8: Image reconstructions for different uniform scattering water solutions with carbon black concentrations of: 2.5, 3.5, 4.5, 5.5, 6.5 and 7.5%.in weight.

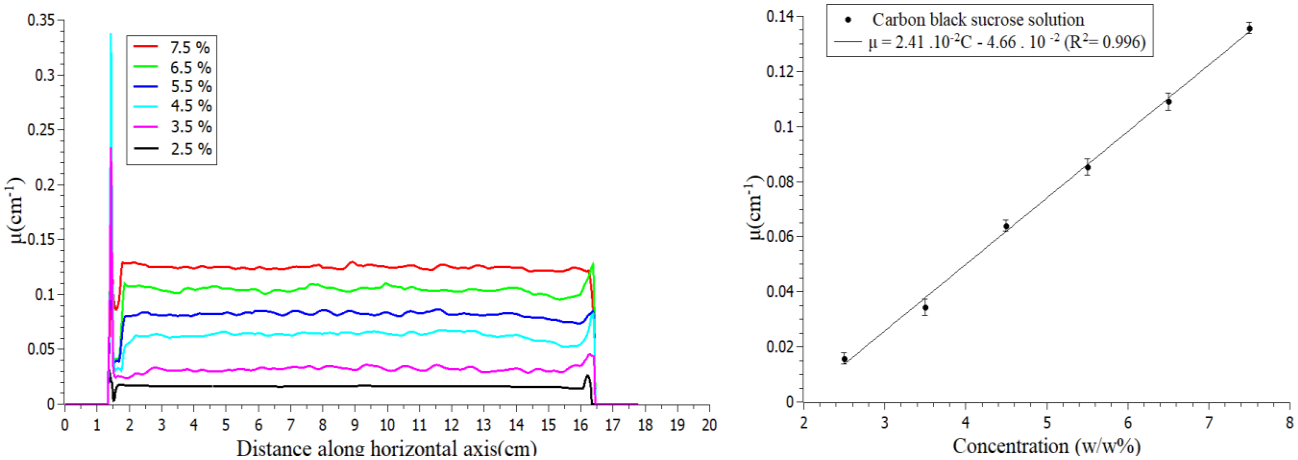

Figure 2.9: a) Light attenuation expressed as linear attenuation coefficient (μ) profile along the horizontal axis showing a uniform behavior for all concentrations. B) Linear behavior for scattering attenuation coefficient versus carbon black concentration.

2.3.4 – Small volume (finger) carbon black insertions.

To investigate the performance of the optical CT for small volumes with different attenuation coefficient distributed in a large volume (15 cm diameter), figure 2.10A presents the FDK image reconstruction of the first set of gelatin-carbon black solution, and figure 2.10B shows the same images with the SIRT-TV reconstruction algorithm, the main idea here was verifying if the same behavior found in a large cylinder filled with carbon black solution is reproducible in small volumes. Figure 2.11 shows a 7% gelatin carbon black solution used in the gel preparation as an example. It shows a different decrease of the error bar on the 7% gelatin carbon-black concentration, however, the best CRN found in figure 2.1A is at the same value of the regularization parameter $\lambda = 0.01$. This means that the same parameters used in a uniform solution in a large volume can be used for this small volume inserted in a larger volume. The comparison with the spectrophotometer measurements, figure 2.11B, shows that the attenuation coefficient value inside the carbon-black region with the optical CT shows good concordance.

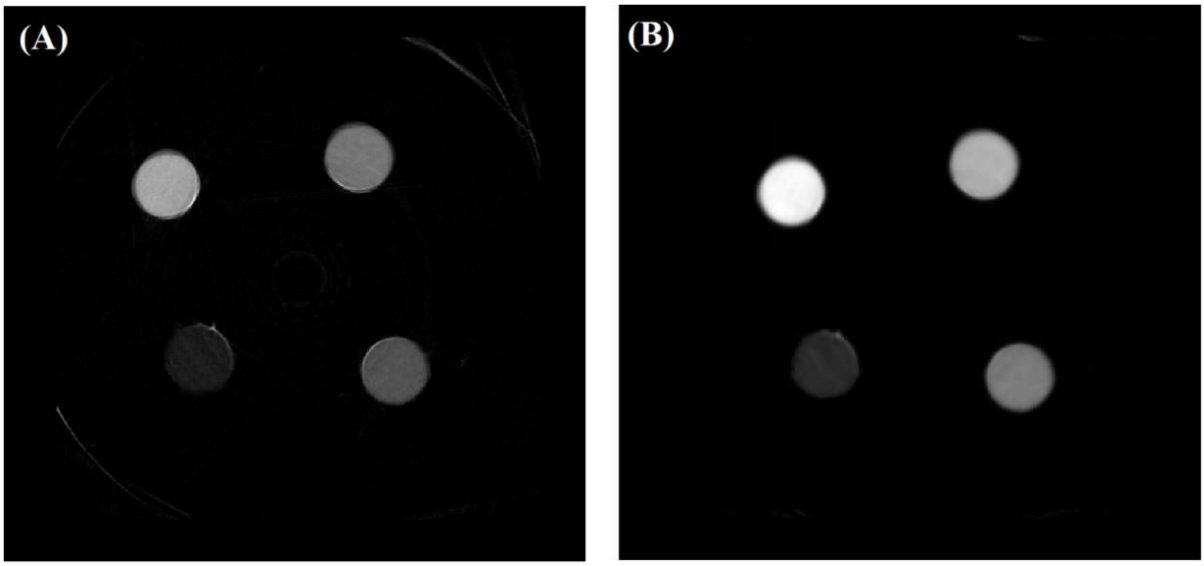

Figure 2.10: The reconstructed image of "finger" distributions of gelatin - carbon black A) with the FDK algorithm. B) with the SIRT-TV algorithm using n= 25 and λ =0.01.

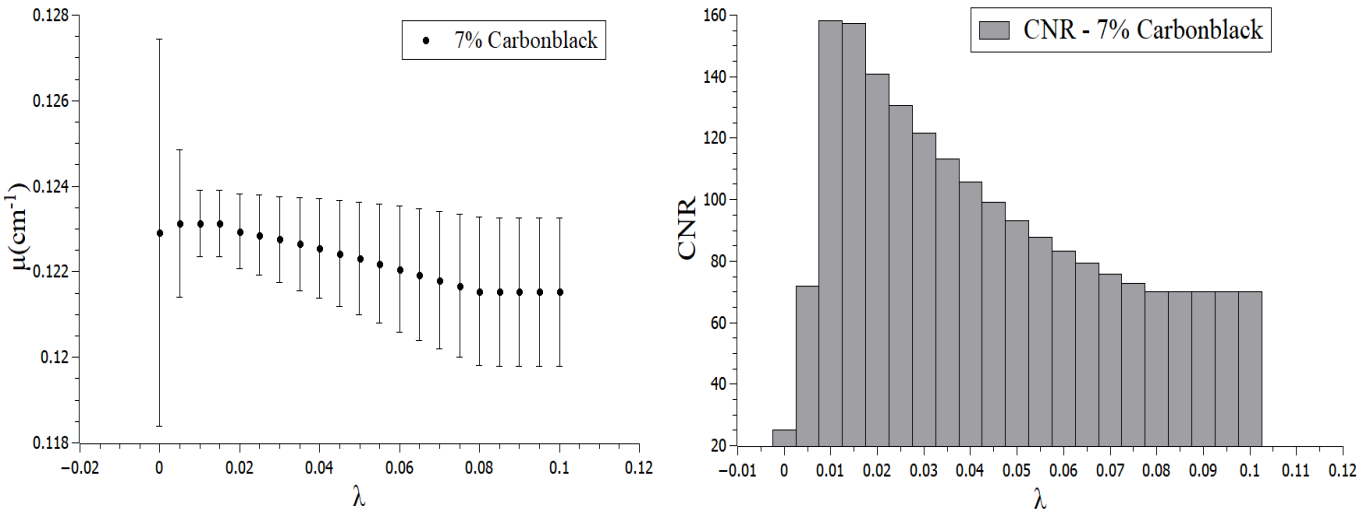

Figure 2.11: Attenuation coefficient (A) plotted to present the average value and error bar in ROI inside 7% carbon-black gelatin versus λ. (B) CNR histogram versus λ, presenting best CNR at λ=0.01

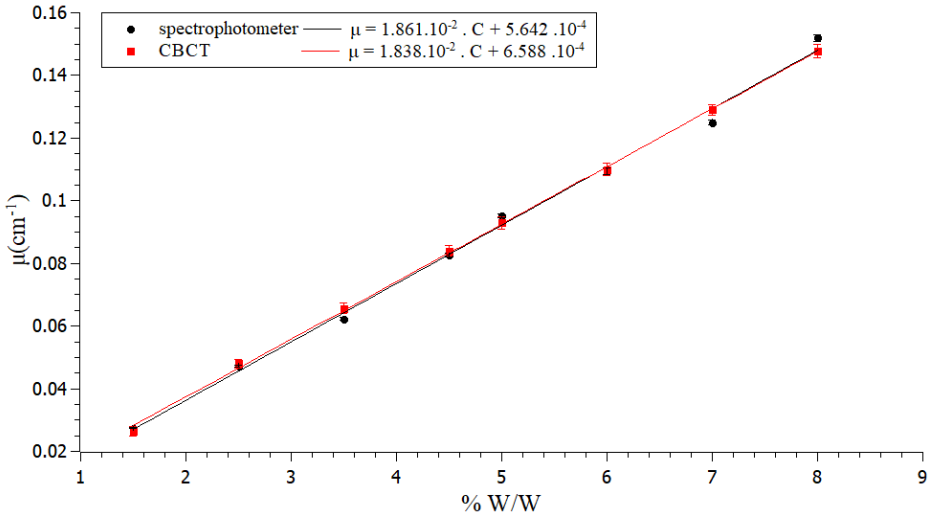

Figure 2.12: Comparison of measurements of the linear attenuation coefficient μ obtained by a commercial Spectrophotometer and with the optical-CT developed in this work presenting a good concordance.

Figure 2.12 presents the behavior of the attenuation coefficient determined by the CBCT and spectrophotometer. Comparing these results for concentrations of 2.5% to 8%, there is a slight percentage difference of 1.2% on the slope obtained by the two detectors. This difference is possibly due to small scattered light contamination, due to the non-optimized vessel used in the image reconstruction. However, the spectrophotometer presents the same behavior as optical-CT. This confirms that reconstructions in this system can be used to determine the attenuation coefficient related to chemical concentrations and, therefore, dose distributions detected by gel dosimeters along this cylinder volume.

2.3.5 – Scatter solution uniform phantom

Figure 2.13 shows the reconstructed images comparing FDK (Figure 2.13A) and SIRT-TV algorithms (figure 2.13B) for 4% LDR concentration in a uniform 15cm vessel. CNR was improved by iterative reconstruction using 25 as the number of interaction and 0.01 as minimization parameter λ in total variation code changing 11.68 to 864.58, resulting in a uniform profile resolution as shown in figure 2.13(C). Figure 2.14 shows that the

same minimization parameter λ of 0.01 results in the best CNR value for the reconstructions.

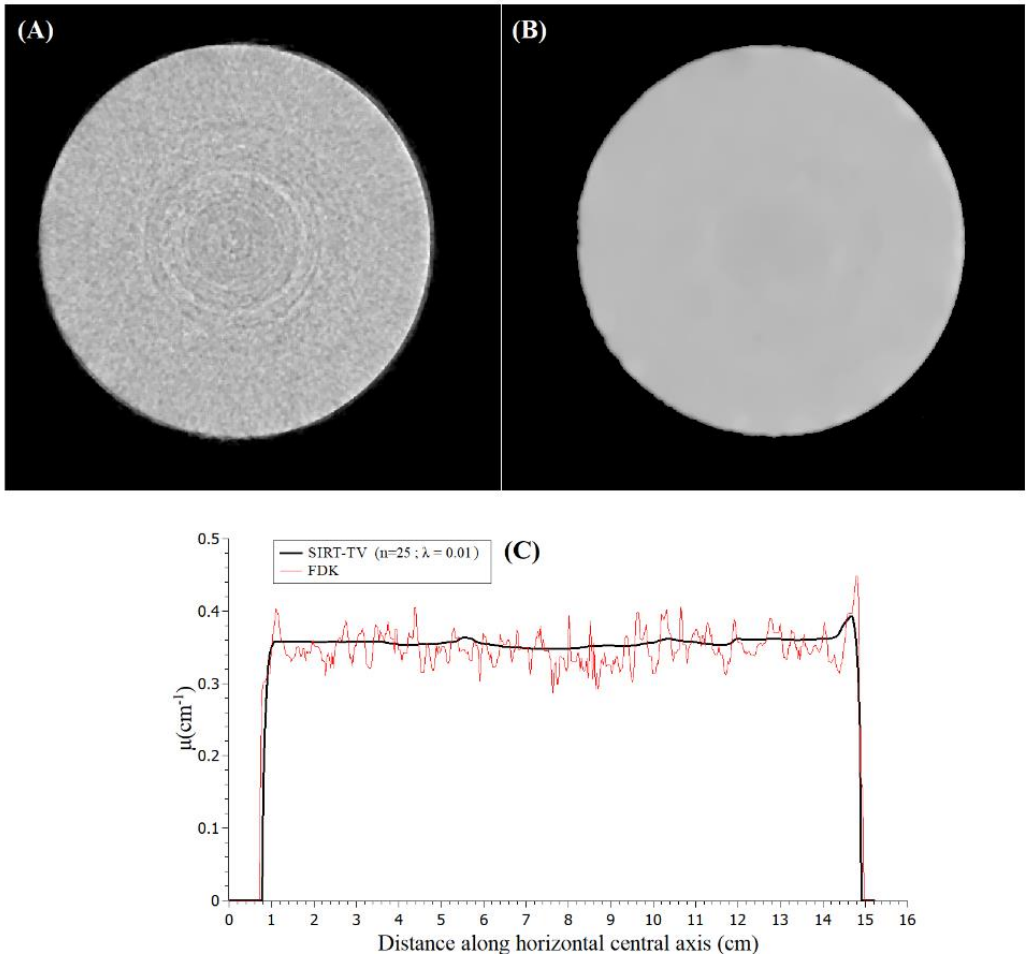

Figure 2.13: A) Reconstructed image to 4% LDR concentration using FDK algorithm. B) SIRT-TV, n= 25, λ=0.01. C) Comparison between horizontal profile to FDK versus SIRT-TV.

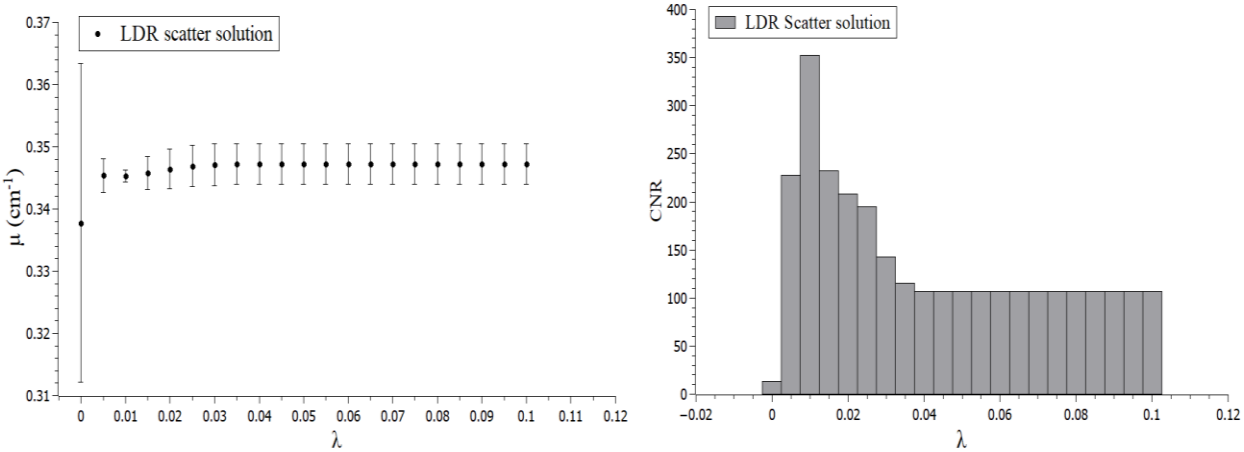

Figure 2.14: Attenuation coefficient (A) Plotted presenting the average value and error bar in ROI inside LDR solution versus λ. (B) CNR histogram versus λ, present best CNR at λ=0.01

Figure 2.15 shows uniform reconstructions to LDR samples for 0.5, 1, 2, and 4% concentration. The contrast changes for this scattering solution. Plotting the horizontal profile along the central axis, the uniformity intensity can be visualized (figure 2.16A), and by calculating the mean value in an ROI with a 15 cm radius it is possible to visualize a linear behavior when the concentrations LDR scattering solution change (Figure 2.16B). The slope results in the equation: $\mu = 8.43 .10^{-3} C + 9.34 .10^{-3}$, where μ is the scattering attenuation coefficient, and C is the concentration of scattering solution.

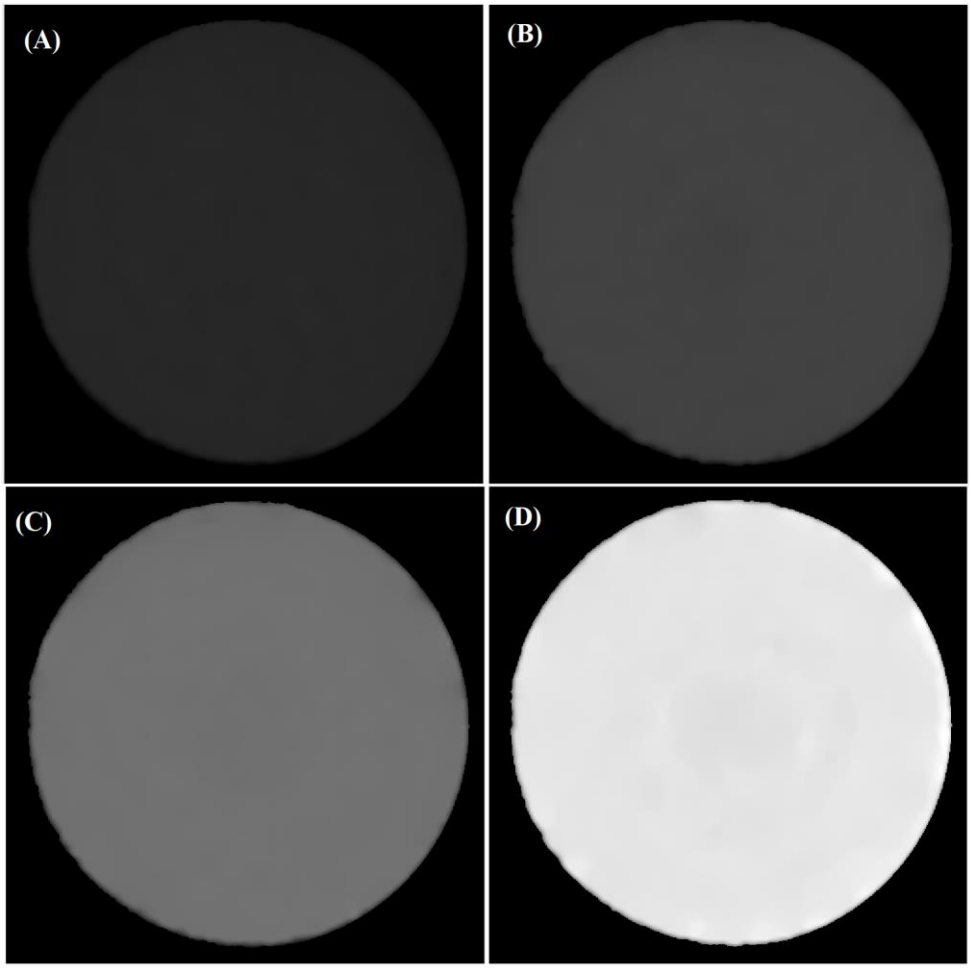

Figure 2.15: Reconstructions for different uniform scattering solution. LDR concentrations: 0.5, 1, 2 and 4%.

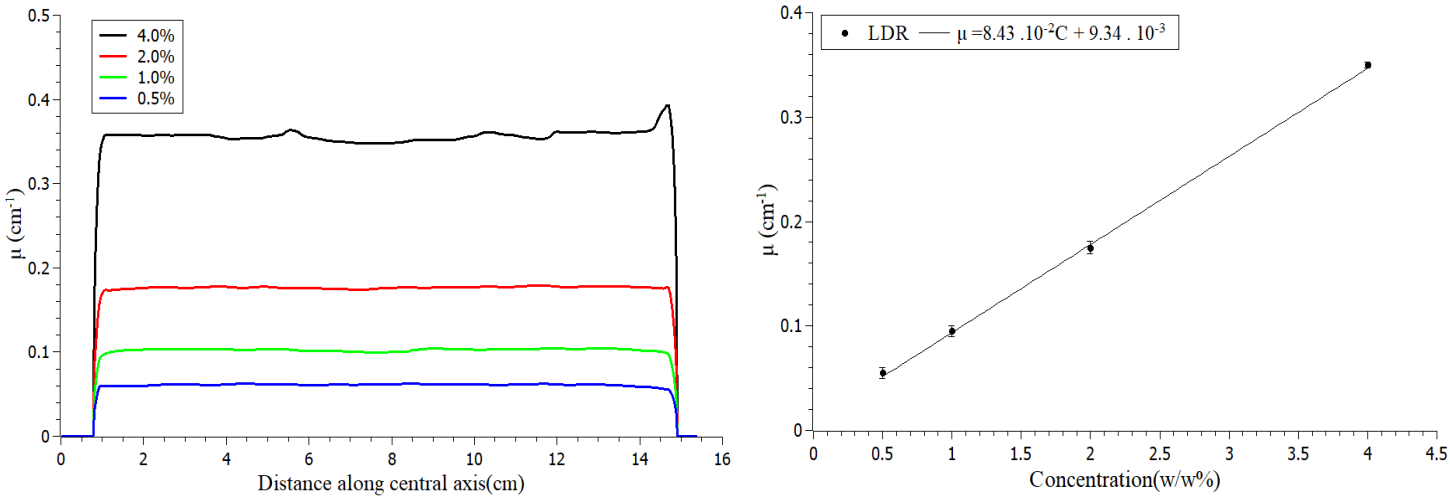

Figure 2.16 a) Profile of the attenuation coefficient μ along the horizontal axis showing a uniform behavior for all concentrations. B) Linear behavior for scatter attenuation coefficient versus LDR concentration.

2.3.6 - PDD Reconstruction - 5x5 cm^2

PDD was determined using the images calculated for a maximum dose of 2.5 Gy. We noticed the dose values' agreement obtained with the optical-CT and the values measured with the ionization chamber. Figure 2.17 (A) shows, in grayscale, the reconstructed axial image along the axis at the maximum dose slice. The comparison between ionization chamber and optical CT measurements was done using the central profile in sagittal axis figure 2.17(B) and is presented in figure 2.18(A). In this comparison, the same behavior was found. The highest doses (from 85% to 100%) and minimum doses detected in this irradiation process (from 55% to 60%) show good agreement, with a percentage difference of 0.1%, smaller than found comparison with carbon black solution. However, with doses from 60% to 80% at the jar center, this difference shows an average value of 1.2%, the same value of the carbon-black solution compared with the spectrophotometer.

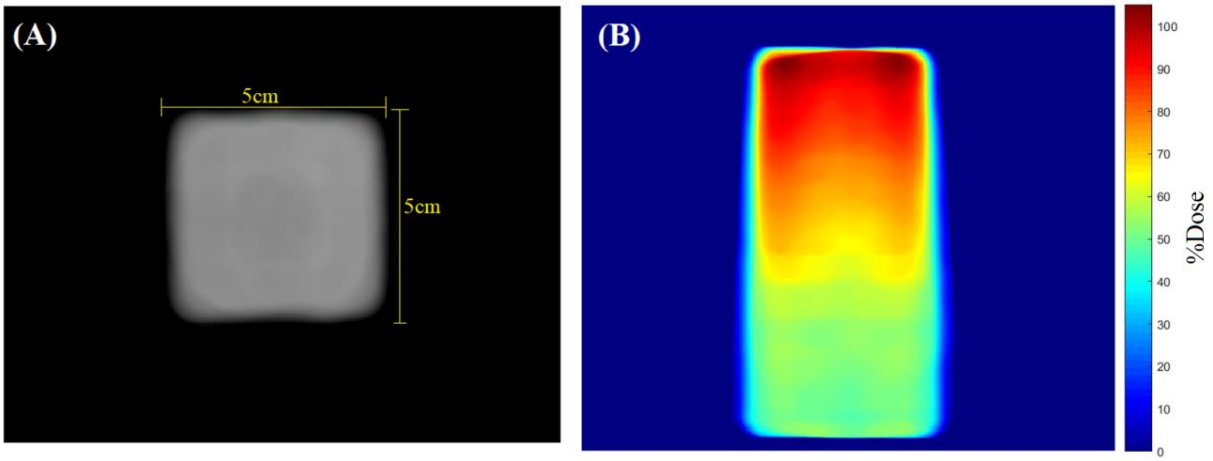

Figure 2.17 a) Reconstructed image from a 5x5 PDD. B) PDD image from a center to along the sagittal axis.

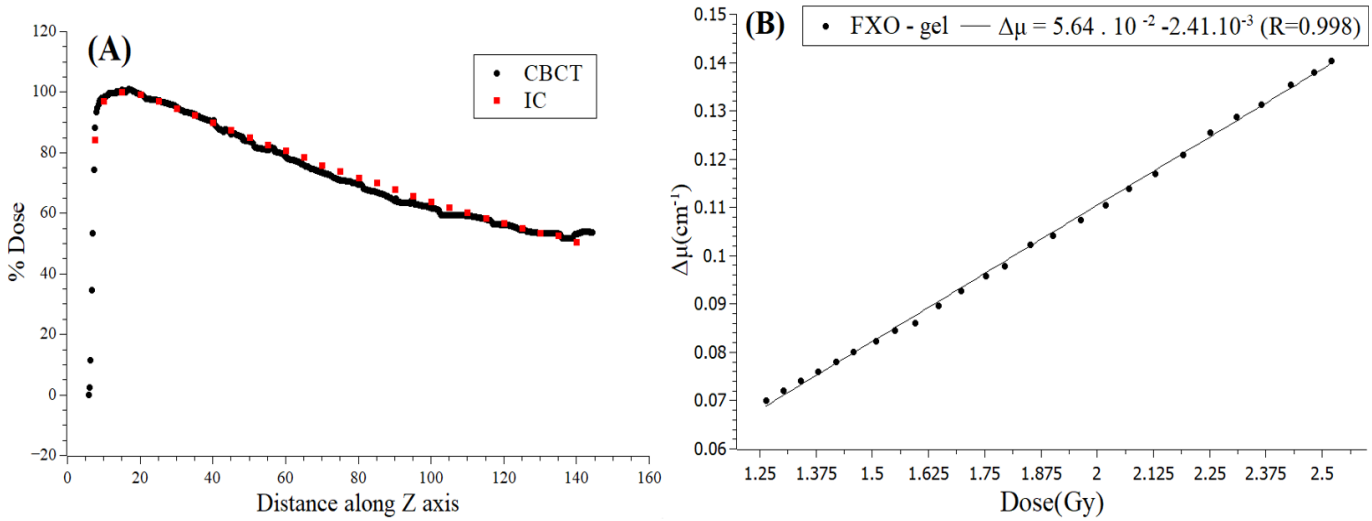

Figure 2.18: a) Comparison between PDP profile along central axis calculated by the ionization chamber (red) and gel dosimeter (dark) B) Linear behavior to absorbed dose-related to attenuation coefficient.

The determination of Δμ relative to dose, presented in figure 2.18 (B), shows the linear behavior ($R^2 = 0.998$) with a sensitivity of 0.056 cm^{-1}/Gy. From this curve, we determined the dose resolution of 0.1 Gy in the range of 0.8 Gy to 2.5Gy max dose.

The remarkable agreement between IC and CBCT and the linear behavior of Δμ relative to dose shows that the optical-CT based on the convergent light source seems suitable for 3D dosimetry.

2.4 - Conclusions

In this study, we built a CBCT based on the convergent light source. The results presented here show that this version of CBCT has low stray light contamination using uniform solutions and scattering solutions. The determination of attenuation coefficients shows excellent accordance with the spectrophotometer measurements when the interactive algorithm SIRT-TV is used to remove noise and artifacts. When comparing FXO gel sensitivity determination by the optical CT of a 5x5cm^2 PDP to the one determined by the ionization chamber we have less than 3% difference. Future studies will test new vessels to perform the best optical CT reconstruction and perform a complete 3D dose distribution measurement comparing the measured results with the treatment planning system calculation using gamma analysis.

References

Bache S, Malcolm J, Adamovics J and Oldham M 2016 Optical-CT 3D dosimetry using Fresnel lenses with minimal refractive-index matching fluid PLoS One 11 e0152606

Baldock C, De Deene Y, Doran S, Ibbott G, Jirasek A, Lepage M, McAuley, KB, Oldham, M., Schreiner, L.J., 2010. Polymer gel dosimetry. Phys. Med. Biol. 55 (5), R1–R63.

Babic S, McNiven A, Battista J and Jordan K 2009 Three-dimensional dosimetry of small megavoltage radiation fields using radiochromic gels and optical CT scanning *Phys. Med. Biol. 54* 2463–81

Beister M, Kolditz D., and Kalender W. A., Iterative reconstruction methods in X-ray CT, Phys. Med., vol. 28, no. 2, pp. 94–108, Apr. 2012

Bosi S, Naseri P, Puran A, Davies J and Baldock C 2007 Initial investigation of a novel light-scattering gel phantom for evaluation of optical CT scanners for radiotherapy gel dosimetry *Phys. Med. Biol. 52* 2893–903

Campbell WG, Rudko DA, Braam NA, Wells DM, Jirasek A,2013. A prototype fan-beam optical CT scanner for 3D dosimetry. Med Phys; 40: 061712

Dekker K H, Battista J., and Jordan K 2016., Stray light in cone-beam optical computed tomography: II. Reduction using a convergent light source *Phys. Med. Biol. 61* 2910

Dekker K H, Battista J., and Jordan K., 2017a Scanning laser optical computed tomography system for large volume 3D dosimetry *Phys. Med. Biol. 62* 2636

Dekker K H, Battista J J and Jordan K J 2017b Technical note: evaluation of an iterative reconstruction algorithm for optical CT radiation dosimetry *Med. Phys. 44* 6678–89

Dekker K H, Hazarika R, Silveira M A and Jordan K J 2018 Fixed, object-specific intensity compensation for cone-beam optical CT radiation dosimetry *Phys. Med. Biol. 63* 06NT02

Doran S J, Koerkamp K K, Bero M A, Jenneson P, Morton E J and Gilboy W B 2001 A CCD-based optical CT scanner for high-resolution 3D imaging of radiation dose distributions: equipment specifications, optical simulations and preliminary results *Phys. Med. Biol.46* 3191

Doran S.J. and Krstajić N., 2010. The history and principles of optical computed tomography for scanning 3-D radiation dosimeters. J. Phys.: Conf. Ser. 56 005

Feldkamp L A, Davis L C, and Kress J W,. 1984 Practical cone-beam algorithm *J. Opt. Soc. Am.* A *1* 612–9

Gore J C, Ranade M, Maryanski M J and Schulz R J 1996 Radiation dose distributions in three dimensions from tomographic optical density scanning of polymer gels: I. Development of an optical scanner *Phys. Med. Biol. 41* 2695

Granton P V, Dekker K H, Battista J J and Jordan K J 2016 Stray light in cone beam optical computed tomography: I. Measurement and reduction strategies with planar diffuse source *Phys. Med. Biol. 61* 2893

Jordan K. ,2013,. Optical computed tomography liquid calibration phantom.,. Phys.: Conf. Ser. 444 012076

Jordan K and Battista J 2006 Linearity and image uniformity of the Vista^{TM} optical cone beam scanner *J. Phys.: Conf. Ser. 56* 217

Kelly R G, Jordan K J and Battista J J 1998 Optical CT reconstruction of 3D dose distributions using the ferrous–benzoic–xylenol (FBX) gel dosimeter *Med. Phys. 25* 1741

Krstajić N and Doran S J 2007a. Characterization of a parallel-beam CCD optical-CT apparatus for 3D radiation dosimetry *Phys. Med. Biol.52* 3693

Krstajić N and Doran S J 2007b. Fast laser scanning optical-CT apparatus for 3D radiation dosimetry *Phys. Med. Biol. 52* N257

Maryanski M J and Ranade M K 2001. Laser microbeam CT scanning of dosimetry gels *Medical Imaging Proc. SPIE 2001* 764–74

Matenine D, Goussard Y and Després P 2015 GPU-accelerated regularized iterative reconstruction for few-view cone-beam CT *Med. Phys.42* 1505–17

Olding T, Holmes O and Schreiner L J 2010 Cone beam optical computed tomography for gel dosimetry I: scanner characterization *Phys. Med. Biol. 55* 2819 – 40

Olding T and Schreiner L J 2011 Cone beam optical computed tomography for gel dosimetry II: image protocols *Phys.Med. Biol. 56(5):1259 – 79*

Rudin L.I. Osher S, Fatemi E., 1992. Nonlinear total variation based noise removal algorithms." Physica D, vol. 60, pp. 259 – 268.

Thomas A and Oldham M 2010 Fast, large field-of-view, telecentric optical-CT scanning system for 3D radiochromic dosimetry *J. Phys.: Conf. Ser. 250* 012007

Thomas A, Newton J and Oldham M 2011 A method to correct for stray light in telecentric optical-CT imaging of radiochromic dosimeters *Phys. Med. Biol. 56* 4433–51

Van Doorn T, Bhat M, Rutten T P, Tran T and Costanzo A 2005 A fast, high spatial resolution optical tomographic scanner for measurement of absorption in gel dosimetry *Australas. Phys. Eng. Sci. Med. 28* 76–85

Wolodzko J G, Marsden C and Appleby A 1999 CCD imaging for optical tomography of gel radiation dosimeters *Med. Phys. 26* 2508

Chapter 3 - Characterization of radiochromic hydrogel dosimeters, ferrous xylenol orange and Turnbull-blue, enhanced to have a higher melting point

3.1 - Introduction

Gel dosimeters are chemical dosimeters representing the unique alternative for truly measuring tridimensional (3D) dose distributions (Baldock et al, 2010). This capability makes them the ideal dosimeter for quality assurance (QA) of the most advanced radiation therapy techniques. Their typical composition includes 90% water, 4% to 8% of gelatin, and 2% to 6% the radiosensitive chemicals (Schreiner, 2004) (Baldock et al, 2010).

The ferrous sulfuric acid solution is one of the first radiochromic aqueous dosimeters based on the oxidation of ferrous (Fe^{2+}) to ferric (Fe^{3+}) ions upon radiation (Fricke H and Morse S, 1927) (Fricke H and Hart E, 1955). The ferrous solution's association with a gelatin matrix made possible the acquisition of 3D dosimetric information by magnetic resonance imaging (MRI) scanning (Gore et al, 1984). Since its first formulation presentation, several authors have tried to improve their dose sensitivity and reduce the Fe^{3+} ions' diffusion by adding new reagents to this gel dosimeter.

The first try to increase dose-response sensitivity was the addition of benzoic acid. Gupta and Nilekani added benzoic acid and xylenol orange to the ferrous solution (FBX), allowing the observation of its color change with visible light as a function of the dose; they also extensively investigated this system's radiochemistry (Gupta and Nilekani, 1998). The addition of benzoic acid to the gel dosimeter minimized the organic impurity effects in the FBX solution. However, its role in hydrogels was considered minor. Other

authors found that adding benzoic acid to FXO gel improved its sensitivity for low doses (Valente et al, 2016), (Silvia et al, 2003).

Appleby and Leghtouz added the Fricke xylenol orange (FXO) solution to opaque agarose gel (Appleby and Leghtouz,1991) to increase gelatin hardening and reduce ions diffusion. Kelley et al. added the FBX solution to gelatin to form a transparent radiochromic gel (Kelley et al 1998) and find an adequate light wavelength for the dosimeter readout. Another improvement of FXO gel was glycerol's addition to the gelatin matrix to reduce the gel's diffusion and optical scattering (Jordan and Sekimoto, 2010). Gallo changed gelatin to the PVA matrix (Gallo et al, 2018). He also added glutaraldehyde as a crosslinker to increase the gel's melting point and hardening; this modification further improved the gel's sensitivity and reduced its diffusion coefficient (Gallo et al, 2019). A low background absorbance was recently achieved by using low bloom strength gelatin in the dosimeter's formulation (Babu et al, 2019). Phenanthroline ligands to reduce auto-oxidation and glyoxal as a crosslinking agent to reduce diffusion in FX hydrogel dosimeters were also examined (Penev and Mequanint 2013). Yang et al 2015, examined substituting xylenol orange for 5-sulfosalicylic acid in glutaraldehyde crosslinked polyvinyl alcohol gel and achieved a low diffusion rate, dosimeter.

Another radiochromic gel dosimeter is Turnbull's blue (TB). It was initially formulated by Solc (Solc J and Spevacek, 2009) and is based on the chemical complex Turnbull's blue, a Prussian blue chemical variant. The reduction of ferric to ferrous ions upon radiation (Balog et al 1999) is its response mechanism. This gel's main advantage is the inhibition of diffusion; however, the spontaneous reduction is its principal enemy, resulting in a fast darkening of the samples. To solve this problem, the use of phytagel as a gelling matrix suppressed spontaneous reduction. However, the gelatin matrix also promoted a faster reduction because of organic reactions (Solc et al, 2009). TB gel

formulations are low sensitive to dose variations. Therefore, their use in quality assurance (QA) measurements applies to high doses delivery treatments, such as the gamma Knife ones. In this application, good accordance was achieved between the delivered doses measured with TB gel with the ones calculated by the treatment planning system (Kateřina Pilařová et al, 2014).

This work investigates the addition of formaldehyde as the crosslinking agent to obtain a high melting point of the gelatin matrix of FXO and TB gel dosimeters, improving their usability at higher temperatures. Formaldehyde was chosen to crosslink gelatin (Davis et al, 1963) because it is less toxic than glutaraldehyde, which was proposed earlier with the same aim (Sun et al, 1990). Also, formaldehyde was previously added to MAGIC-f polymer gel dosimeter and increased the gelatin matrix melting point up to 69 ºC (Pavoni and Baffa, 2012).

Furthermore, this work studies these two modified gels' responses to dose rates irradiations from 100 to 1400 cGy/min. The understanding of the dosimeter's response in such high dose rates values is important because several treatments modalities are employing flattening filter-free beams of linear accelerators (LINAC), such as intensity-modulated radiation therapy (IMRT), stereotactic radiosurgery (SRS) or stereotactic body radiation therapy (SBRT) (Xiao et al, 2015). Due to the high dose conformity of these treatments and the high dose rate delivery of the doses, the availability of 3D dosimeters for these techniques QA may be a precious tool for the clinical practice.

3.2 - Material and methods

3.2.1 - Preparation of gel dosimeters

Ferrous xylenol orange formulations.

Five different recipes of FXO were prepared. The first one (FXO) followed the original FXO formulation. The second (FXO-GLY) contains glycerol as the first try to reduce the

diffusion coefficient by increasing viscosity (Jordan and Sekimoto, 2010). The addition of glycerol to the gelatin matrix results in a darker gel, with limited light transmission through the samples in larger flasks. Thus, the sulphuric acid concentration was increased, which makes the PH indicator (xylenol orange) present a bright color, but at the expense of a less sensitive final gel than the original one (Jordan and Sekimoto, 2010). Formaldehyde was added to the other formulations to evaluate its influence in combination with glycerol (FXO-GLY-f) and higher gelatin concentrations (FXO1-f and FXO2-f). In the last two formulations, the number of crosslinks between gelatin and formaldehyde will increase by increasing the gelatin concentration. Table 1 presents all the formulations with their reagents concentration.

Gel preparation was similar to Babic (Babic et al, 2008). Whenever a different step was used, it is presented in this section. 300 Bloom porcine gelatin was added to deionized water and left stirring in a water bath up to 50 °C for three hours to decompose peroxides. These peroxides are partly responsible for the initial oxidation of FXO-gel. 4mm diameter Zinc pellets cleaned by a 1M of hydrochloric acid were added to the gelatin solution for 15 minutes and finally removed, leaving the gelatin in another cleaned beaker. This step scavenges residual peroxides responsible for spontaneous oxidation of FXO-gel. After removing the zinc pellets, the solution was cooled to 30 °C. The sulfuric acid was added to the solution. After five minutes of homogenization, the addition of xylenol orange solution, ferrous ammonium sulfate, and formaldehyde was done. These reagents were taken from a 1M xylenol orange solution and a 2M sulphuric acid solution. Ferrous ammonium sulfate was weighed and added to a solution to achieve the concentration shown in Table 3.1. The gel dosimeter solution was stirred for five minutes more before filling 5 ml optical plastic cuvettes. The samples were then left for 24up to 96 hours (1 to 4 days) to study best time to complete the gelling process at 5 °C in a refrigerator for this

modified formulations. For the formulations with glycerol, the reagent was added after the dissolution of all gelatin in water as described by Jordan and Sekimoto 2010. The formaldehyde is consumed by the gelling process's crosslinking reaction, resulting in a low toxicity gel formulation.

Table 3.1: Reagent total mass percentage or concentration of the five different FXO gels prepared. All materials were from Sigma Aldrich.

Chemicals	FXO	FXO-GLY	FXO-GLY-f	FXO1-f	FXO2-f
Gelatin (300 bloom)	4%	6%	6%	6%	8%
Glycerol	-	20%	20%	-	-
Ferrous ammonium sulphate	0.3 mM	0.3 mM	0.3 mM	0.3 mM	0.3 mM
Xylenol orange	0.1 mM	0.1 mM	0.1 mM	0.1 mM	0.1 mM
Sulfuric acid	50 mM	65 mM	65 mM	50 mM	50 mM
Formaldehyde (37% CH_3O)	-	-	3%	3%	3%

Turnbull' s-blue gel with formaldehyde

Modified TB gel was prepared following the steps of Solc (Solc et al, 2009). Starting with porcine gelatin added to Mili-Q deionized water and warm up to 50 °C in a water bath, under continuous stirring. After homogenization, the solution was cooled down to 30 °C, and the solution of potassium ferricyanide was added. Ferric chloride in water solution generates small precipitates. Thus, the hydrochloric acid was added slowly to dissolve them and achieve a homogenous solution. After five minutes of stirring for the homogenization, formaldehyde (37% CH_3O) was added to the gel, as 3% of the total sample mass. Cuvettes were filled with the gel and left 24 hours for gelling at 5 °C in a refrigerator. This modified formulation will be called TB-f. The original TB gel, without formaldehyde, was also prepared. However, the samples melted so fast in our environmental temperature 25 ± 2 ºC after taking out the refrigerator, that their analysis was not possible.

Table 3.2: Reagent total mass percentage or concentration of TB-f gel. All materials were from Sigma Aldrich.

Chemical	Concentration
Gelatin (300 bloom)	6%
Potassium Ferricyanide	1 mM
Ferric Chloride	1 mM
Formaldehyde (37% CH_3O)	3%
Hydrochloric acid	5 mM

3.2.2 - Packing gels.

The prepared gels dosimeters were packed in polymethylmethacrylate plastic optical cuvettes with a volume of 1.0 x 1.0 x 4.5 cm^3 sealed with Parafilm M®.

3.2.3 - Measurement of melting point

For each gel formulation, five cuvettes were prepared for the melting point measurements. A steel ball with 3 mm diameter was pressed approximately 6 mm into the top of cuvette gel. The cuvette was placed in 80 ml of water in a small glass beaker and heated at 1ºC per minute. The water level was the same as the gel height. A thermistor placed in the water recorded the bath temperature. A small thermal gradient exists between the bath and ball. The ball was observed to begin wobbling approximately 0.3 ºC before reaching the cuvette's bottom, and then the melting point was registered.

3.2.4 - Evaluation of Diffusion Coefficients and Spontaneous oxidation (FXO) reduction (TB)

To evaluate the diffusion behavior of modified FXO and TB gels, cuvettes containing the gels were irradiated using a 6 MV beam with an absorbed dose of 4 Gy in one half of the cuvette. Samples were positioned at SSD of 100 cm, in the center of a 10 x 10 cm^2 field size, and a half-beam blocked irradiation was performed. Half of the field size was blocked by the collimator, resulting in a 5 x 10 cm^2 field covering half of the cuvette, and

the other half was not irradiated. Over 24 hours' images were taken from these samples positioned in our convergent cone beam optical CT (CBCT). The samples were scanned at a temperature of 22 ± 2 ºC. The pictures were acquired by an ELP 8-bit camera with a varifocal lens 5 to 50mm. Three light sources were employed to illuminate the gels. To avoid the threshold described by Babic et al, 545 nm peak was used for FXO gel, 590 nm peak for FXO-Gly-f (Babic et al,2008), and TB gel dosimeter scanning was done at the red region the available, with 630 nm peak. From these images, we obtained the optical density (OD) profile of transmission along the non-irradiated region to the irradiated region.

The diffusion coefficients were calculated following the methodology reported in 1997 by T. Kron (Kron 1997). The achieved OD profiles curves were fitted with the inverse of square root function (ISQR – equation 3.1). Solc also used this method in 2009 for TB gel diffusion coefficients measurements using transmission images (Solc et al.,2009). In this study, the ISQR has OD_1 as the optical density of non-irradiated region, OD_2 the intensity of irradiated region, x is the distance from dose gradient and a(t) is a curvature parameter meaning the slope of gradient region in the optical density profile. This parameter a(t) is directly related to diffusion coefficient D, $D = 0.2119\frac{da}{dt}$ where the $\frac{da}{dt}$ is the slope of the graphic of parameter a(t) versus time in hours.

$$OD(x) = OD_1 + \frac{1}{2}(OD_2 - OD_1)\left[1 - \frac{x}{\sqrt{x^2+a(t)}}\right] \quad (3.1)$$

For the FXO-GLY-f measurement, a 10 cm diameter by 11 cm high sample was irradiated with a half-beam blocked, 5 x 10 cm field size, and 6 MV beam irradiating one quadrant. Sequential 3D optical CT scans, over the next twenty hours, were reconstructed to measure profile change versus time. The typical diffusion coefficient of FXO gel found in the literature is in the range of 0.8 up to 1.05 mm^2/hr at the environment temperature

of 25 ºC (Kron et al, 1997; L.J. Schreiner,2004). Therefore, to study the dependence of the diffusion coefficient for the modified FXO gels, we measured this parameter for all formulations presented in table 1. Turnbull-blue gel dosimeter has a diffusion coefficient of 2.3 $.10^{-3}$ mm^2/hr (Solc et al, 2009), this value validates TB gel as a non-diffuse gel. It is expected that TB-f gel presents at least the same behavior. Spontaneous oxidation was evaluated using the same experimental setup as in the diffusion calculation. In this case, the data extracted is the mean intensity of an ROI in a non-irradiated region, and the variation of attenuation coefficient Δμ with time was calculated.

3.2.5 - Spectrophotometer scanner and Attenuation coefficients calculation

Absorbance and transmission measurements were performed using a spectrophotometer (Ultrospec 2100). Absorbance scanning was performed using a 1 nm wavelength increment, recording the intensities from 300 nm to 900 nm and taking as reference a cuvette filled with deionized water. Transmission measurements were performed using the same wavelength range. We also calculated the optical attenuation coefficient (μ) using the Beer-Lambert law as:

$$\mu = -\frac{1}{x}\left(\ln\frac{I}{I_0}\right) \quad (3.2)$$

X is the optical path of the cuvette (1cm), I is the light intensity through the absorbed dose, and I_0 is the light intensity through deionized water.

3.2.6 - Irradiation process – Dose rate and energy dependence

The dose rate dependence was performed in two steps for each modified gel, FXO2-f, and TB-f. The first set of experiments evaluated dose rate dependence from 100 to 400 cGy/min using a Unique^{tm} (Varian Medical Systems) 6 MV LINAC at 22 ± 1ºC room's temperature. The second set of experiments was performed using the 6 MV beam of a Varian True Beam LINAC, to investigate the dose rate dependence from 400 to 1400 cGy/min. The irradiation temperature was 20 ± 1ºC. These samples were kept at 4 °C

during transportation. They were positioned at SSD of 100 cm in a 20 x 20 cm^2 field size, and acrylic plates were used to guarantee the necessary buildup and backscattering. Doses of 1, 3, 6, 9, and 12 Gy were delivered.

The energy dependence evaluation was performed using only the True Beam LINAC beams (6 MV and 15 MV). The same setup and doses described were used.

3.3 - Results and Discussions

3.3.1 - Melting point

The melting points pasting time of the studied formulations are presented in table 3. As expected, FXO and TB gels' original formulations present the lowest melting points, which makes it difficult their use without thermal control. The average environment temperature at some locations or transportation from one place to the other can be as high as 35 ºC. For this reason, it is also desirable to have a higher melting point dosimeter.

The FXO and FXO-GLY gels melting temperatures measurements are within the variation of 1º C of melting points for similar gels (gelatin handbook 2012, Osorio 2007). The Original TB formulation presents the lower melting point, verifying the impossibility of using these dosimeters in environmental temperatures of 30 to 35ºC, such as detected before in this study. FXO1-f, FXO2-f, and TB-f present melting temperatures higher than 50 ºC, after 72 hours stored in refrigerator, which confirms the contribution of formaldehyde to the crosslinking of gelatin molecules in these formulations.

Table 3.3: Melting point of FXO formulation and TB formulation

Gel formulation	Melting Point(°C)			
	Day 1	Day 2	Day 3	Day 4
FXO - Original	32.1 ± 0.5°C	32.5 ± 0.8°C	33.1 ± 0.5°C	31.2 ± 0.4°C
TB - Original	22.1°± 0.8°C	21.4°± 0.5°C	20.4°± 0.7°C	23.1°± 0.9°C
FXO - GLY	31.9°± 0.4°C	32.9°± 0.4°C	32.2°± 0.4°C	32.5°± 0.6°C
FXO – GLY-f	39.4°± 0.6°C	42.2°± 1.2°C	43.5°± 1.5°C	45.1°± 1.1°C
FXO1-f	42.3°± 1.4C	47.3°± 2.1°C	51.3°± 1.6°C	55.3°± 1.5°C
FXO2-f	47.3°± 0.9°C	55.2°± 0.8°C	65.2°± 1.2°C	71.4°± 1.0°C
TB-f	52.7°± 0.9°C	53.4°± 0.9°C	55.2°± 0.9°C	55.7°± 0.9°C

3.3.2 - Diffusion study

All FXO gel diffusion coefficient were evaluated to gel stored for 72 hours stored in refrigerator, to guarantee the improved of the melting point. Figure 3.1A shows the FXO2-f gel OD profile along the non-irradiated (lower intensity) and the irradiated (higher intensity) region for 0.5, 4.5 and 24.5 hours after irradiation to illustrate the fitting of the inverse of square root function (ISQR). The profile inclination change indicates ferric xylenol orange complexes' diffusion from the irradiated to the non-irradiated region. The same behavior occurs for all the other formulations.

Figure 3.2A presents the plotting of a(t) parameter versus time for the different formulations used in this study. The highest slope is related to the highest diffusion coefficient. FXO2-f formulation presents the smallest diffusion with a coefficient of 0.216 mm^2/hr. The second smallest diffusion coefficient was verified for the FXO-GLY-f formulation. Thus, the addition of formaldehyde and glycerol (FXO-GLY-f) reduced the diffusion coefficients more than the addition of only glycerol (FXO-GLY). The role of glycerol to reduce the diffusion coefficient was already known, but the use of formaldehyde was not presented before.

The FXO2-f formulation resulted in a diffusion coefficient reduction of 75% and 52% of the original FXO and the FXO-GLY formulations. This characteristic of FXO2-f gel makes it more suitable to be used as a tridimensional dosimeter. Therefore, this formulation was used for the dosimetric characterization presented in the next sections.

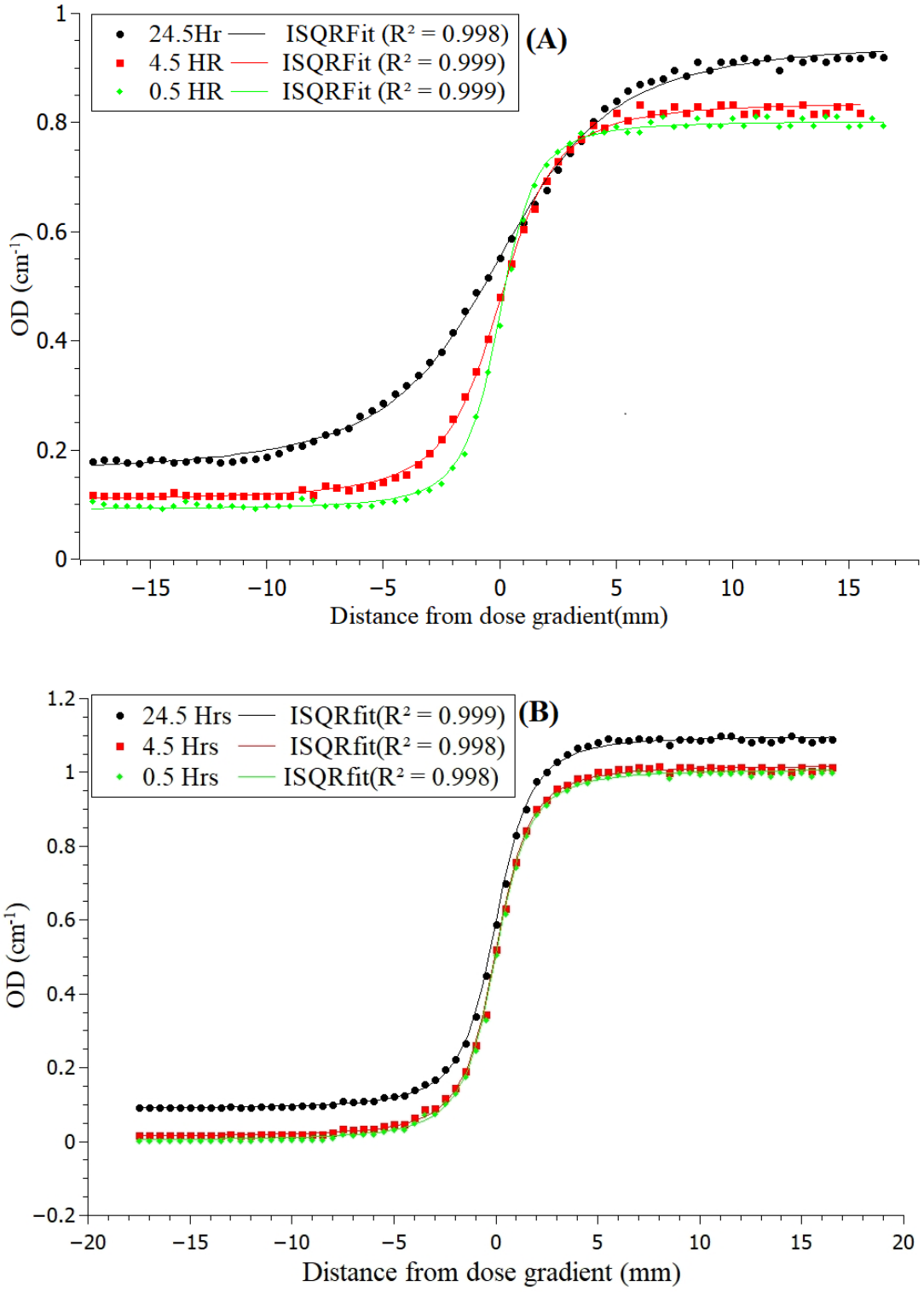

Figure 3.1: Optical density profile along dose gradient for the modified gels (markers) and corresponding fitted function (solid line): (A) FXO2-f gel, (B)TB-f

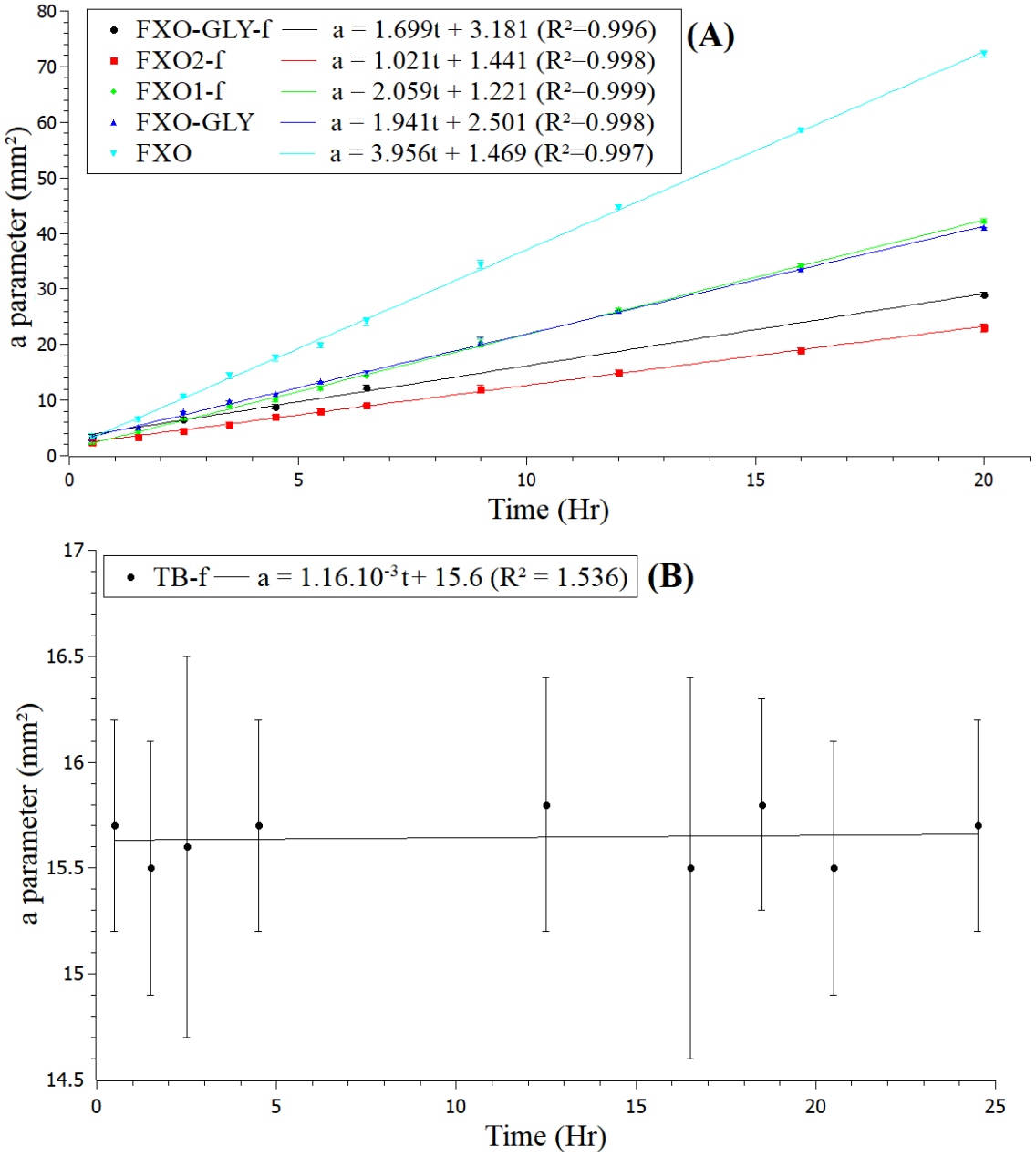

Figure 3.2: Time-dependent parameter a(t) versus post-irradiation time for modified gels:(A) FXOs (B)TB-f

The TB-f OD profile is visualized in figure 3.1B. No significant changes in the profile were verified with time, including no diffusion or auto-reduction. The non-diffusing gel characteristic is confirmed in Figure 3.2B, where the time-dependent parameter a(t) plotted does not vary with the time considering the error bars. Similar behavior was presented in the study of Solc et al., 2009. An average of the time-dependent parameter

a(t) = 15.7± 0.1 mm² along these 24 hours was calculated, and this small standard deviation confirms that no diffusion occurred in the analyzed time interval. The time-dependent parameter plot slope is 1.16 $.10^{-3}$ mm^2/hr, resulting in a diffusion coefficient of $2.10 \cdot 10^{-3}$ mm^2/hr at the environmental temperature of 24 ± 2 ºC. This result is 47% less than the $4 \cdot 10^{-3}$ mm^2/hr found by Solc for the original formulation at 24ºC, and reproduces the result of $2.3 \cdot 10^{-3}$ mm^2/hr at 5ºC (Solc et al, 2009), indicating that the addition of formaldehyde also lowered the diffusion rate for this gel.

Table 3.4 summarizes all diffusion coefficients found for the formulations studied in this study.

Table 3.4: Diffusion coefficients (D) for all gels formulations

Concentration	D (mm^2/hr)
FXO	0.837
FXO-GLY	0.411
FXO-GLY-f	0.361
FXO1-f	0.436
FXO2-f	0.216
TB	0.00230
TB-f	0.00233

3.3.3 - Auto – oxidation study

The spontaneous oxidation study was evaluated over 20 hours by monitoring the optical attenuation coefficient variation in a non-irradiated gel ROI (Figure 3.3).

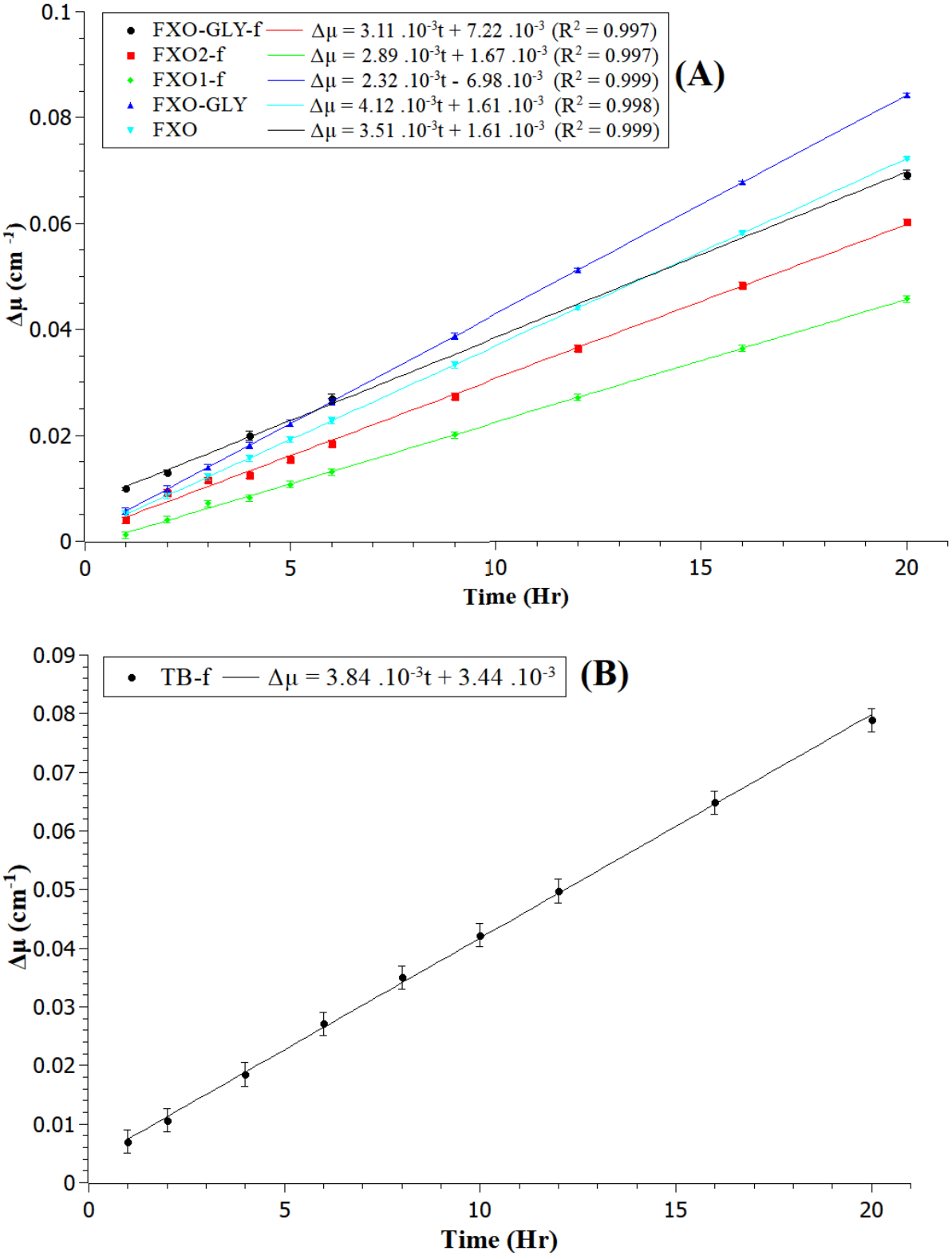

Figure 3.3: Variation of optical attenuation coefficient Δμ (A)FXO (545 nm), (B)TB-f (630 nm) gels

Figure 3.3A shows the evolution of Δμ for FXO gel, which is correlated with the chromophore concentration, along the time. The slope of each line, $\frac{d\mu}{dt}$ in units of cm^{-1}/hr is the darkening rate due to FXO gel auto-oxidation. Comparing the auto-oxidation rates of different concentrations, FXO-GLY has the fastest auto-oxidation rate. The gels with formaldehyde addition, FXO1-f and FXO2-f, show the slowest darkening rate among FXO gel formulations, with $2.32 \cdot 10^{-3}$ cm^{-1}/hr and $2.89 \cdot 10^{-3}$ cm^{-1}/hr, respectively. These values correspond to reductions of 25% and 30% compared to the original value of $3.51 \cdot 10^{-3}$ cm^{-1}/hr. Faster auto-oxidation rates may affect the transmission images between pre-scan and post-scan, compromising the Δμ determination in 3D dosimetry using these gels. Therefore, it is desirable that a gel dosimeter presents slow rates of auto-oxidation.

The modified TB-f gel dosimeter spontaneous reduction rate is $3.84. 10^{-3}$ cm^{-1}/hr at 25 °C. Figure 3.3B shows this behavior over a 20 hours' interval. Therefore, it is recommended to keep these gels at low temperatures to reduce this spontaneous darkening rate.

3.3.4 - Absorbance spectrum

Figure 3.4A shows the FXO2-f absorbance spectrum for different absorbed doses determined using as reference deionized water. By comparing the curves with a previous report (Gambarini 2017), formaldehyde's addition does not affect the original absorbance spectrum. The scanning wavelength of 545 nm was highlighted in the absorbance spectrum because it was used to calculate the attenuation coefficient presented.

Figure 3.4B shows the absorbance spectrum for TB-f gel. The 705 nm wavelength peak is close to the peak at 690 nm found by Solt et al 2009. This displacement is the result of increasing the potassium ferricyanide and ferric chloride concentration, which also improved the dose response of our gel (Solc et al, 2009). Although not being the spectrum

peak value, the 630 nm wavelength was used to calculate the attenuation coefficient in this study because it was the red light wavelength available in our CBCT.

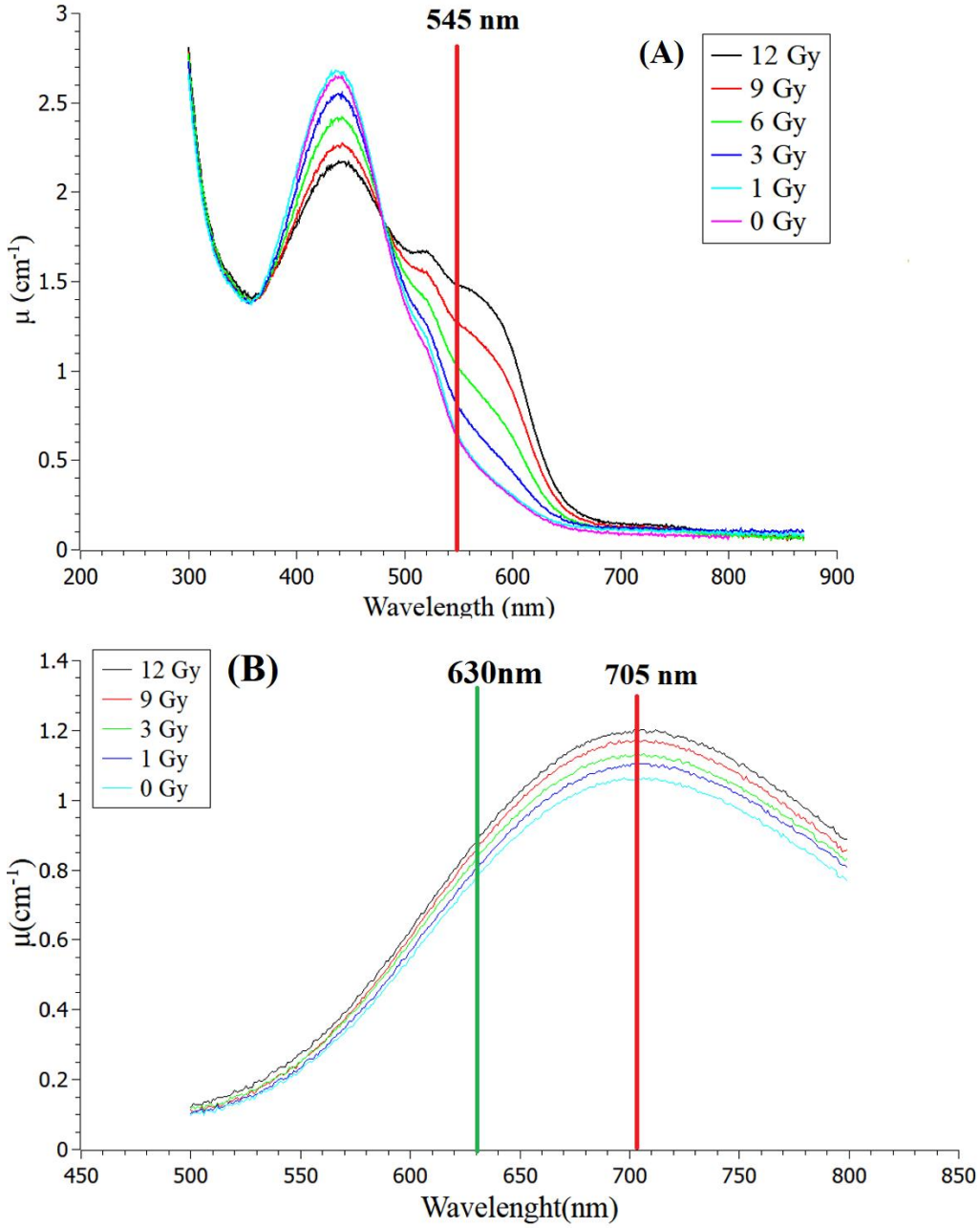

Figure 3.4: Absorbance spectra of modified gel dosimeters: (A) FXO2-f, B) TB-f, 705nm is the peak of absorbance and 630nm the scanned wavelength.

The linear dose-response curves for the original FXO and the FXO2-f gels are presented in figure 3.5. The attenuation coefficients were calculated using water as a

reference. The sensitivities of both gels are similar, being $0.98.10^{-1}cm^{-1}Gy^{-1}$ and $0.99\ .10^{-1}\ cm^{-1}Gy^{-1}$ for FXO and FXO2-f. The non-significant difference between these values indicates that formaldehyde's addition does not affect the gel dosimeter's sensitivity. The same comparison for TB and TB-f gels was not possible because of the TB gel melting temperature.

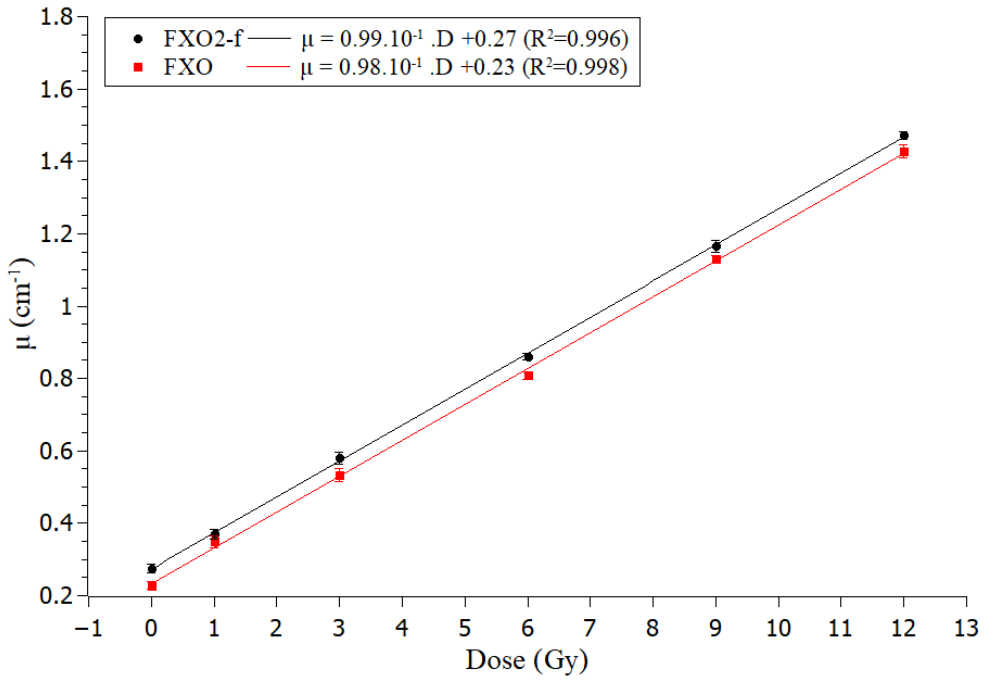

Figure 3.5: Attenuation coefficient (545 nm) versus dose of FXO gel and modified FXO2-f

3.5 - FXO2-f and TB-f energy dependence

Figure 3.6A compares the FXO2-f dose-response curves for irradiations using two energies: 6 MV and 15 MV. Again, the attenuation coefficients were determined using water as a reference. The gels' sensitivities for irradiations with 15 MV and 6 MV beams are $0.99\ .10^{-1}cm^{-1}Gy^{-1}$ and $1.01\ .10^{-1}cm^{-1}Gy^{-1}$, respectively, which corresponds to percentage difference of 2%. For TB-f gel (figure 3.6-B), the 15 MV sensitivity is $1.21\ .10^{-2}\ cm^{-1}$/Gy and for 6MV it is $1.20\ .10^{-2}\ cm^{-1}$/Gy, corresponding to a difference of only 1%. The order of scanning can explain the separation of the TB-f gels curves. The energy dependence and the dose rate dependence experiments were done on the same day, and

the 15MV sample was the last one scanned. Thus the auto reduction occurred in this sample and resulted in the linear coefficient variation of 1% found.

For both gels, no significant dose sensitivity difference was verified when changing the energy of the radiation beam from 6 to 15 MV.

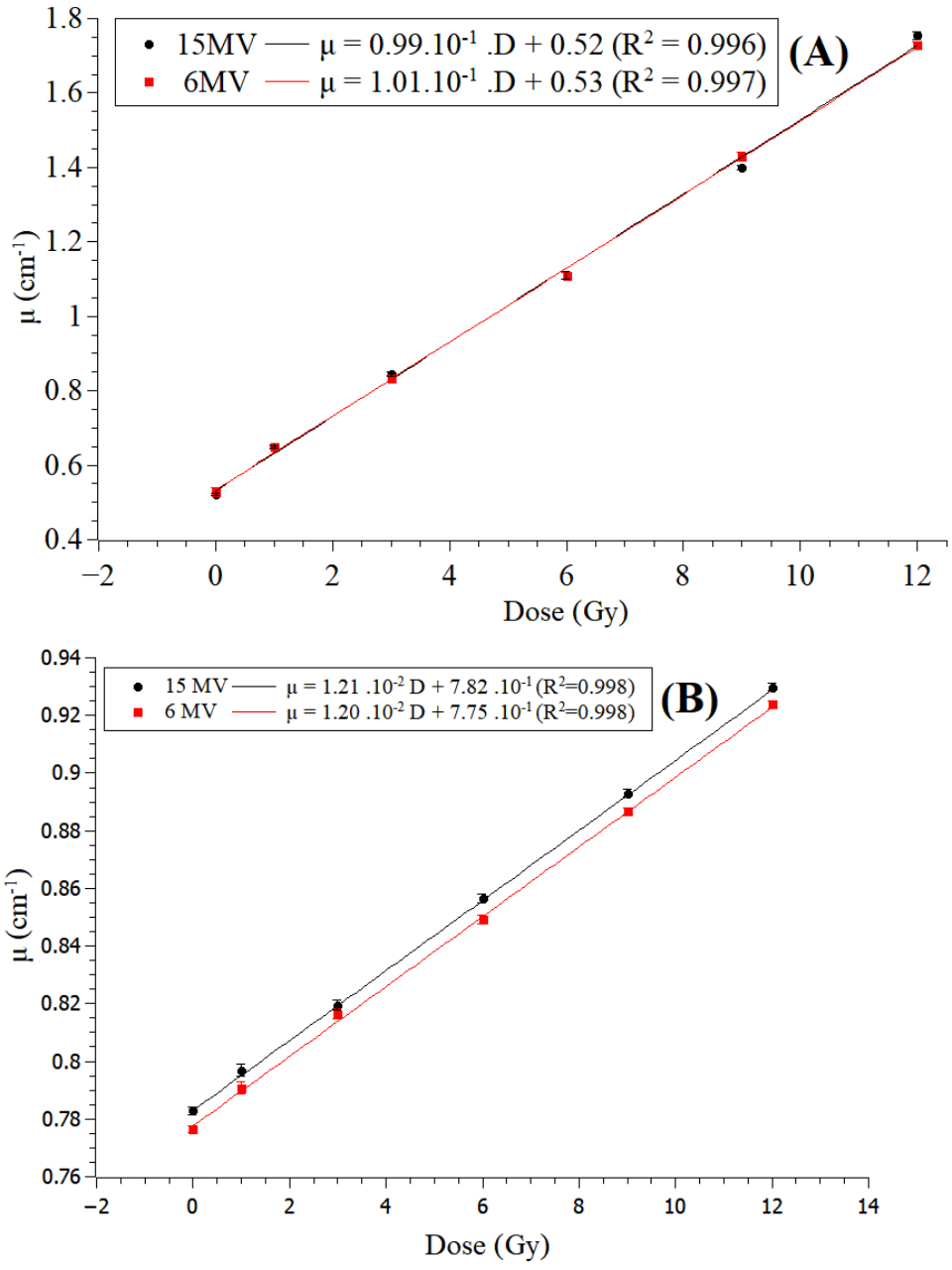

Figure 3.6: Attenuation coefficient (545 nm) vs dose and photon beam energy; (A) FXO2-f, (B) TB-f.

3.3.6 - FXO2-f and TB-f dose rate dependence

Dose rate dependence was evaluated for a range from 100 cGy/min to 1400 cGy/min. The irradiation with different dose rates can alter the creation of radicals in the gel matrix and, consequently, modify its response depending on its value. It is also important to guarantee that the gel dosimeter has the same behavior when irradiated in different beams.

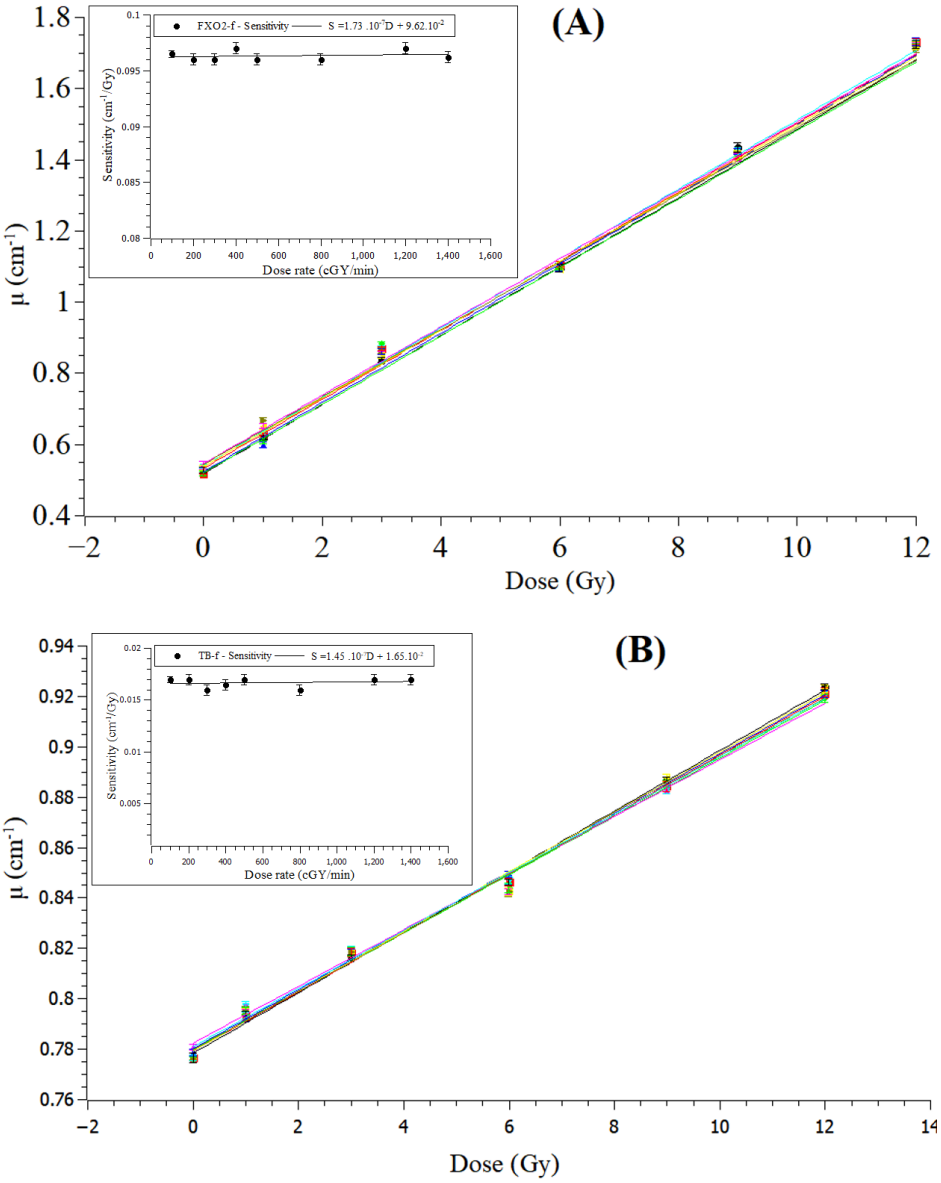

Figure 3.8: Attenuation coefficient (545 nm) vs dose and dose rate from 100 to 1400 cGy/min: (A)FXO2-f (545 nm), (B)TB-f (630 nm).

The mean sensitivity value for FXO2-f irradiation in the selected dose rate range was (0.96 ± 0.01) 10^{-1} $cm^{-1}Gy^{-1}$ (Figure 3.8A). When we compare the maximum sensitive value (0.97 $.10^{-1}$ $cm^{-1}Gy^{-1}$) with the minimum one (0.95 $.10^{-1}$ $cm^{-1}Gy^{-1}$) the percentage difference is 2%. The TB-f dose-response evaluation at the same dose rates (figure 8B) resulted in a mean sensitivity value of (1.16 ± 0.02).10^{-2} $cm^{-1}Gy^{-1}$ and in a maximum sensitivity variation difference of 3%.

No significant sensitivities variations in the dose rate range evaluated were found for FXO-2 and TB-f gel dosimeters. This behavior allows them to be used in tridimensional measurements of different radiotherapy modalities with variable high dose rates, such as IMRT or SRS/SBRT treatments using FFF beams.

3.4 - Conclusions

The present study improved the FXO and TB gel dosimeter dosimetric performance and handling, making these chemical dosimeters more suitable for being used in the clinical context. The addition of formaldehyde to the gelatin matrix increased the gels' melting point to 65.2 ºC for FXO2-f and 55.2 °C for TB-f, after 72 hours. The gels showed almost no energy dependency (<1%), presenting the same sensitivity for 6 MV beam and 15 MV beam. Their dose rate dependence for irradiations from 100 cGy/min to 1400 cGy/min varied only 2% for FXO-2 and 3% for TB-f. The diffusion coefficient evaluation showed that FXO2-f gel presents a 75% smaller diffusion rate than the original formulation without crosslinking. Therefore, the formaldehyde addition to FXO and TB gels resulted in more adequated tridimensional dosimeters than the previous formulations.

References

Appleby A and Leghrouz A, 1991, Imaging of radiation dose by visible color development in ferrous-agarose-xylenol orange gels Med. Phys. 18, 309-312.

Babu S, Peace S, Rafic K, Raj E, Christopher S, Ravindran P, 2019. Escalation of optical transmittance and determination of diffusion coefficient in low bloom strength gelatin-based Fricke gel dosimeters. Radiat. Phys. Chem. 156, 300–306.

Babic S, Battista J, & Jordan K (2008). An apparent threshold dose response in ferrous xylenol-orange gel dosimeters when scanned with a yellow light source. Physics in Medicine and Biology, 53(6), 1637–1650.

Baldock C, De Deene Y, Doran S, Ibbott G, Jirasek A, Lepage M, McAuley, KB, Oldham, M., Schreiner, L.J., 2010. Polymer gel dosimetry. Phys. Med. Biol. 55 (5), R1–R63.

Balog J, 1999, Radiation chemical formation and precipitation of Turnbull blue from Fe(III)-oxalate Rad. Phys. Chem. 55483-7.

Baldock, C, Historical overview of the development of gel dosimetry: a personal perspective. J. Phys. Conf. Ser. 56, 14–22.

Davis, P, Tabor, BE, 1963, Kinetic Study of the Crosslinking of Gelatin by Formaldehyde and Glyoxal, J. of Polym. Sci., vol 1, 799-815.

Fricke H and Morse S, 1927, The chemical action of Roentgen rays on dilute ferrous sulphate solutions as a measure of dose Am. J Roent. Radium Ther. Nucl. Med 18, 430–432

Fricke H and Hart E, 1955, Chemical Dosimetry. In Radiation Dosimetry vol. 2 F.H. Attix and W.C. Roesch (Academic Press, New York)

Gallo S, Cremonesi L, Gambarini G, Ianni L, Lenardi C, Argentiere S, Bettega D, Gargano M, Ludwig N, Veronese I, 2018. Study of the effect of laponite on Fricke xylenol orange gel dosimeter by optical techniques. Sensor. Actuator. B Chem. 272, 618–625.

Gallo S, Artus, E, Brambilla MG, Gambarini G, Lenardi C, Monti A, Torresin A, Pignoli E, Veronese I, 2019. Characterization of radiochromic PVA-GTA Fricke gels for dosimetry in X-rays external radiation therapy. J. Phys. D Appl. Phys. 52, 225601.

Gambarini G, Veronese I, Bettinelli L, Felisi L, Gargano M, Ludwig N, Lenardi C, Carrara M, Collura G, Gallo S, et al. 2017, Study of optical absorbance and MR relaxation of Fricke xylenol orange gel dosimeters, Radiat. Meas,106, 622-627.

Gore JC, Yang YS and Schulz R I, 1984. Measurement of radiation dose distributions by nuclear magnetic resonance (NMR) imaging, Phys. Med Biol. 29, 1189–97.

Gupta B, Nilekani S, 1998, Ferrous ion oxidations by H, OH and H2O2 in aerated FBX dosimetry system, Radiat. Phys. Chem. 53, 643-650.

Harris P, Piercy A, Baldock C, 1996. A method for determining the diffusion coefficient in Fe (II/III) radiation dosimetry gels using finite elements. Phys. Med. Biol. 41, 1745–1753.

Sun HW, Feigal RJ, Messer HH, 1990, Cytotoxicity of glutaraldehyde and formaldehyde in relation to time of exposure and concentration, Pediatric Dentistry, 12, 303-307.

Jordan K and Sekimoto M, 2010, Effects of adding glycerol and sucrose to ferrous xylenol orange hydrogel J. Phys.Conf. Ser. 250012048

Pilařová K, Kozubíková P, Šolc J, Spěváčeka V, 2014 , Characteristics of polyacrylamide gel with THPC and Turnbull Blue gel dosimeters evaluated using optical tomography. Radiat. Phys.Chem.14, 283-286

Kelly R U, Jordan K J, and Battista J, 1998, Optical CT reconstruction of 3D dose distributions using the ferrous benzoic-xylenol (FBX) gel dosimeter, *Med. Phys*. *25*, 1741–50.

Kron, T, Jonas D, Pope JM, 1997. Fast T1 imaging of dual gel samples for diffusion measurements in NMR dosimetry gels. Magn. Reson. Imag. 15, 211–221.

Kron T, Lehmann, J, Greer PB, 2016. Dosimetry of ionising radiation in modern radiation oncology. Phys. Med. Biol. 61 (14), R167.

Valente M, Molina W, Silva LC, Figueroa R, Malano F, Pérez P, Santibañez M, and Vedelag V. 2016, Fricke gel dosimeter with improved sensitivity for low-dose-level measurements *Med. Phys*. 17, 402-417.

Pavoni JF and Baffa O, 2012, An evaluation of dosimetric characteristics of MAGIC gel modified by adding formaldehyde, Radiation Measurements 47(s 11–12):1074–1082

Penev K and Mequanint K, 2013. Controlling sensitivity and stability of ferrous–xylenol orange–gelatin 3D gel dosimeters by doping with phenanthroline-type ligands and glyoxal. Phys. Med. Biol. 58, 1823–1838.

Schreiner LJ, Crooks I, Evans MDC, Keller BM, Parker WA, 1994. Imaging of HDR brachytherapy dose distributions using NMR Fricke-gelatin dosimetry, Magn. Reson. Imag. 12, 901–907.

Schreiner LJ, 2004. Review of Fricke gel dosimeters. Journal of physics: Conference Series. 3. 9-21

Silva N, Nicolucci P, Baffa O., 2003, Spatial resolution of magnetic resonance imaging Fricke-gel dosimetry is improved with a honeycomb phantom. Med Phys.; 30: 17– 20.

Šolc J, Spěváček V., 2009. New radiochromic gel for 3D dosimetry based on Turnbull blue: basic properties. Phys. Med. Biol. 54, 5095–5101.

Xiao Y; Kry SF; Popple R; Yorke E; Papanikolaou N; Stathakis S; Xia P; Huq S; Bayouth J; Galvin J; Yin FF., 2015, Flattening filter-free accelerators: a report from the AAPM Therapy Emerging Technology Assessment Work Group. J. Appl. Clin. Med. Phys.; 16: 12–29.

Yang Y, Yang L, Chen J, Chen B, Luo W, Sui G, Lu X, Chen J, 2015. Preparation and characterization of novel sulfosalicylic acid-ferrous-PVA hydrogel as a 3D dosimeter, J Radioanal. Nucl. Chem. 304, 481–487

Chapter 4: Tridimensional dosimetry by optical-CT and radiochromic gel dosimeter of a multiple isocenter craniospinal radiation therapy procedure

4.1 - Introduction

Craniospinal irradiation (CSI) is an important treatment method for primary tumors including medulloblastoma, high-risk germ-cell tumors, and some radio-sensitive secondary malignant tumors of the meninges (Wang et al,2013, Biltekin et al, 2021). CSI traditionally treated the central nervous system using two or three adjacent field sets. However, this planning involves complex anatomical structures and requires more advanced treatment planning resources. In this context, the newer techniques of radiation therapy, tridimensional conformational radiotherapy (3DCRT), and intensity-modulated radiation therapy (IMRT) allow the possibility of improving the planning of this treatment with more safety than traditional procedures using the large fields, (Paker et al.2010, Fogliata et al, 2001), thus irradiating the tumor and at the same time preserving healthy cells.

IMRT technology can offer better conformity index and homogeneity index than traditional multi-field 3DCRT. Nevertheless, IMRT implementation for CSI treatment requires strategies for matching the required treatment fields with non-uniform fluency. Cao et al proposed the jagged-junction IMRT in which a three-isocenter IMRT plan is used to address the junction issues by intentionally overlapping adjacent fields (Cao et al., 2012) After, Wang et al developed the three-isocenter overlap-junction (TIOJ) IMRT, a simplified approach, which reduced the planning and treatment time involved (Wang et al.,2013)

Although, alternatives for the planning issues appeared, they still need rigorous quality assurance (QA) checks to result in real benefits to the patient. Due to the dose distribution complexity, especially in the matching field regions, 3D dose verification may be the ideal tool for QA. 3D dosimetry by gels, combined with an imaging technique, stands out for the 3D determination of absorbed dose along total volume, really simulating the treatment while giving information about the dose distribution in 3D (Baldock et al, 2010, Pavoni et al, 2012, Watanabe et al, 2010).

Optical computed tomography (OCT) is one of the emerging image techniques candidates to perform the 3D dosimetry on the clinical routine (Kelly et al.,1998, Jordan et al, 2013). The recent studies and reconstruction techniques allow the determination of complex dose distributions. In past years, the FXO (Fricke xylenol orange) gel dosimeter demonstrated good results in 3D dosimetry. By combining this radiochromic gel dosimeter with OCT, the 3D dose determination is possible, allowing to perform the comparison between the measured and the treatment system planning (TPS) dose calculation (Arsena et al. 2018, Gallo at al, 2021).

For all of these reasons, this study applied FXO gel dosimeter and OCT for performing a 3D quality assurance procedure in the matcing field of an IMRT CSI planning using multiple isocenters. The plan was previously approved using bi-dimensional dosimetry with an ionization chamber array detector.

4.2 - Materials and methods

4.2.1 – FXO-f gel dosimeter and simulated objects.

The FXO-f is a modified version of the Fricke xylenol orange by the addition of formaldehyde. Its preparation procedure started with the dissolution of 8% gelatin in deionized water. This solution was warmed up to 50ºC in constant stirring for 3 hours. Zinc pellets were added to the gelatin solution for 15 minutes to clean undesired peroxides

and avoid the fast darkening of the gel. Sequentially, the solution was cooled down to 35ºC, and the 3% formaldehyde was added. After five minutes of homogenization, 0.05 mM of xylenol orange and 0.3 mM of ferrous ammonium sulfate diluted in sulphuric acid were added to gelatin solution. The concentration of sulphuric acid in the final gel is 50 mM. For this CSI procedure, three cylinders of 12.5 cm tall and 15 cm in diameter (figure 4.1) were filled with a total volume of 1.9 liters of gel. Two objects were used for PDD (percentage depth dose) curve measurements, and the last one one for the CSI matching field veficiation.A were prepared. The phantoms were left in the refrigerator for 32 hours to guarantee the complete gelling process.

Figure 4.1: Cylindrical object (12.5 cm tall and 15 cm in diameter) filled with FXO-f to perform 3D dosimetry.

4.2.2 – Cervical and head planning

CSI treatment and verification plan creation

Before the irradiation of the cylindrical object, an x-ray computed tomography of the phantom was done using a standard head and spinal protocol in the Philips software of the CT. The phantom was filled with gelatin, and the images acquired were in 512 x 512 pixels resolution with a 0.5 x 0.5 mm² effective pixel size. A reference point in the

cylinder was marked with a radiopaque material to be used as a reference in the 3D treatment planning software (TPS) and the optical CT images.

The x-ray computed tomography images of the cylindrical object were imported to the *Eclipse*® TPS (Varian Medical Systems, Palo Alto-CA) and were used as the base for the CSI verification plan creation. The CSI was planned using the simplified approach described in the TIOJ IMRT treatment protocol with two isocenters, one in the cranial region and the other in the spinal region. The matching of these fields was verified. Therefore, it was necessary to create two verification plans, one for each field used. This happened because of our interest in evaluating the combined dose distribution of the borders of both fields. Figure 4.2 shows the dose distribution of each field of the CSI plan, recalculated in the phantom geometry in the verifications plans visualized using the CERR interface (*Computational environment for radiotherapy research*) (Deasy et al.,2013).

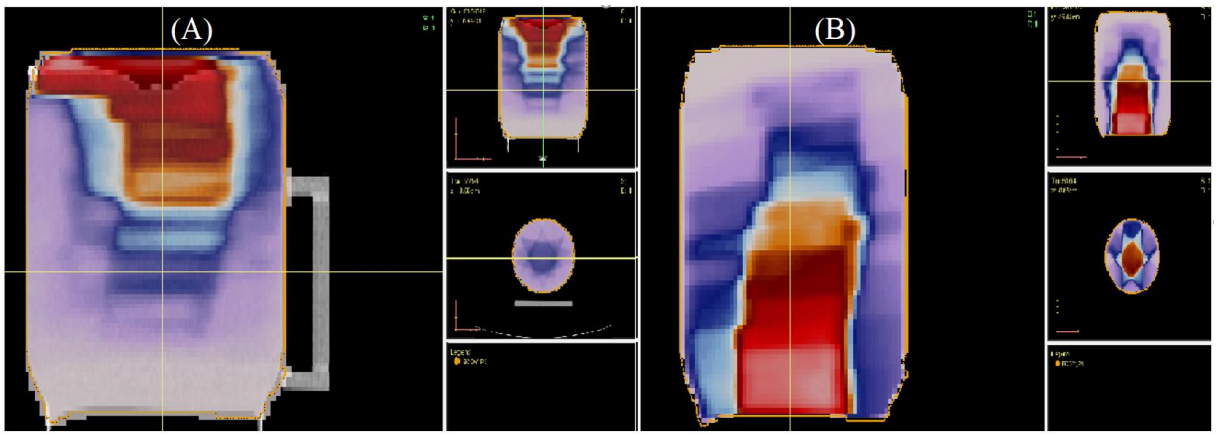

Figure 4.2: Three plan views of the planned dose distribution extracted from the TPS and visualized in CERR. A – Cranial IMRT field. B – Spinal IMRT field

The complete 3D dose distribution to be verified in the matching region was achieved by summing the presented dose distribution data in 3D, by a code written in Matlab. The complete junction dose distribution in the coronal plane is presented in figure 4.3.

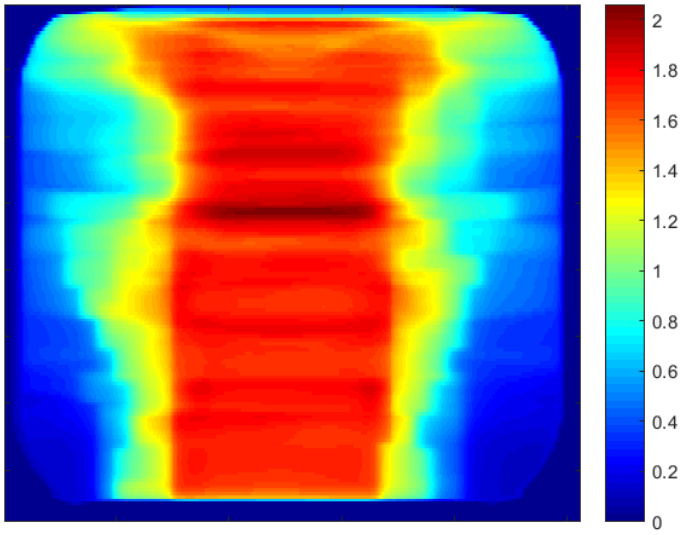

Figure 4.3: Coronal plane of the complete dose distribution at the junction region of the treatment planning in the phantom geometry.

4.2.3 – Irradiations

The irradiation procedures were performed at the radiotherapy service of University Hospital in Ribeirão Preto Medical School, on a 6MV Unique™ LINAC (Varian Medical Systems, Palo Alto-CA).

4.2.3.1 - Calibration

All 3D dosimetry procedures using radiochemical gels require a calibration process for each gel batch prepared because slight differences in the manufacturing process and the aging of the chemicals may result in different attenuation coefficients which are related to the absorbed dose. To calibrate the gel for this procedure, the 15 cm cylinder phantom was positioned inside a larger cylinder filled with water to guarantee all the scattering and back scattering necessary for the PDD measurement at the central axis. The upper surface of the larger cylinder was open and allowed the positioning of the cylindrical gel phantoms in the vertical orientation with 100 cm of the source to surface distance (SSD). Two PDD curves were measured with the two gel phantoms, the first one

with 3 Gy delivered at the depth of maximum dose, and then, we replace the gel phantom and measured another PDD with 1.5Gy at the depth of maximum dose.

4.2.3.2 – Phantom

The irradiation of the phantom followed the CSI plan. Our aim was to measure the matching region of fields used. Considering that our phantom did not cover all the treatment region, it was necessary to locate both treatment isocenters projections in the LINAC couch to allow a careful positioning of the gel phantom in the matching region. All the displacements necessary for the positioning and irradiation were based on the couch coordinates. The phantom was first irradiated with the CSI cranial beam, and after the displacement, the spinal treatment field was delivered to the phantom. This way, the total treatment dose distribution in the matching field region was delivered to the same cylindrical phantom. This phantom was scanned by the optical-CT, and the measured dose distribution was compared to the TPS calculated dose distribution.

4.2.4 – Scanning and image processing

4.2.4.1 – Optical - CT settings

The optical-CT used to scan the gel dosimeters uses a cone beam geometry and is equipped with an EPL-8bit high-resolution camera with a 5-50mm varifocal lens. Its water tank is filled with water and sucrose to adjust the light refraction index, and its convergent light source is provided by a Fresnel lens and a point 3W LED coupled with a 545nm bandpass filter.

4.2.4.2 – Image acquisition protocol

To reconstruct a 3D attenuation coefficient map, the phantom was scanned before irradiation without any delivered dose. After the irradiation, the phantom was scanned

again with the same protocol. The scanning is performed with a complete 360º rotation in 0.5º steps , resulting in acquisition of 720 projections from the cylindrical phantom. Each projection was acquired with 800 x 600 pixels with an effective pixel size of 0.3 x 0.3 mm². The primary reconstruction dose was done with the FDK algorithm, however, to improve resolution and suppress noise, the simultaneous iterative algorithm (SIRT) combined with total variation minimization was implemented, resulting in a high-quality image to compare with TPS. The total scanning time is 1.20 minutes and the reconstruction time for SIRT-TV is 2 minutes. The final images were reconstructed with the same effective pixel size of 0.3 x 0.3mm² and 512 x512 pixels.

4.2.4.3 – Image comparisons

The fiducial marks were used to register the slices in the TPS, and optical CT reconstructed images. These images were compared using a 2D gamma index analyses provide by an own code implemented in Matlab (Low et al., 1997) with the 3%/3mm criteria (Van Dyk et al.,1993) and threshold of 40% of total dose in a slice by slice basis, and a gamma image of each slice was generated. The approval criteria used was that more than 90% of the pixels in the gamma image should be approved to validate de correct matching fields region.

4.3 – Results and discussion

4.3.1 – Calibration

The two PDD images (figure 4.4) were used to build the calibration curve (figure 4.5). The first (figure 4.4 - A) and the second (figure 4.4 - B) PDD images correspond to the delivery of 3 Gy and 1.5 Gy maximum doses to the 12.5 cm axis cylinder.

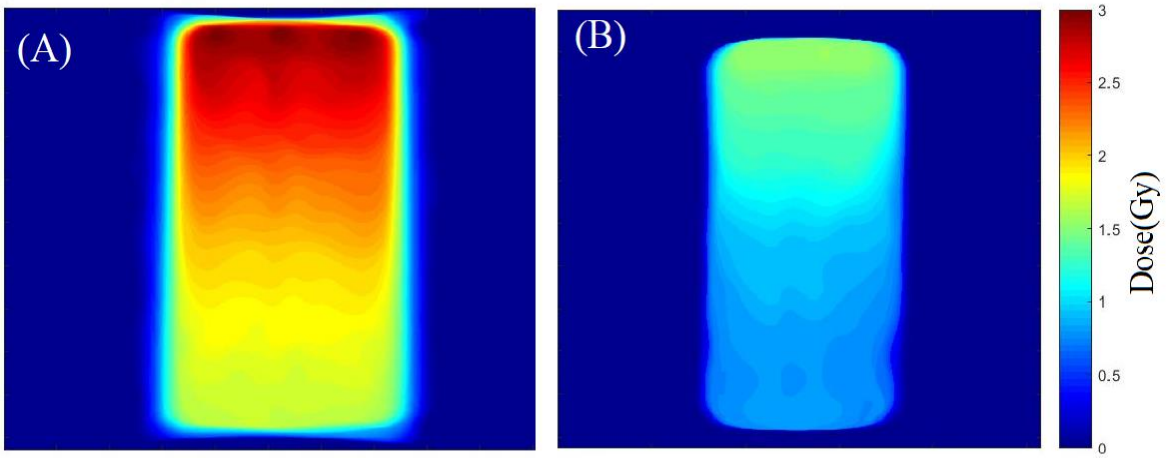

Figure 4.4: Measured PDD for calibration purposes: A –PDD with 3Gy delivered to the maximum dose depth; B –PDD with 1.5Gy delivered to the maximum dose depth.

The calibration curve presented in figure (4.5) shows the linear relation between the attenuation coefficient(μ) and absorbed dose(D) for the two calibration cylindrical objects. This behavior is expected because the same gel batch is present inside the calibration phantoms. A sensitivity of $4.22.10^{-3}cm^{-1}/Gy$ was found from the angular coefficient with an $R^2 = 0.999$ correlation coefficient. This linearity justifies the normalization of the dose distribution in the measured and calculated image. The calibration curves, dose versus attenuation coefficient, present the minimum of 0.8Gy, corresponding the 40% of the total dose, for this reason the comparisons results are presented with a threshold of 40% for the gamma analysis.

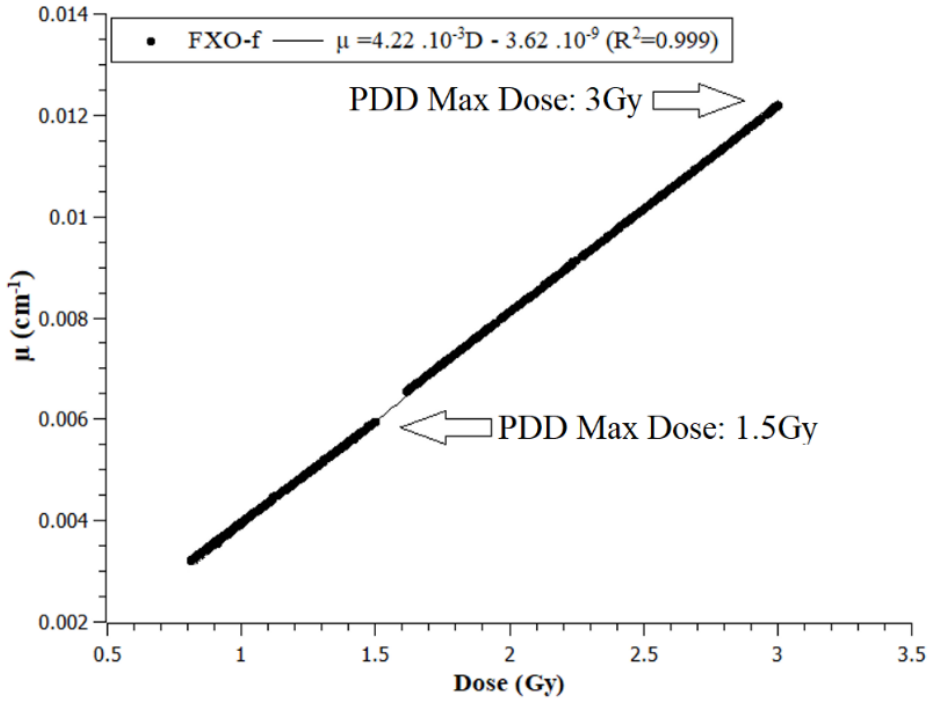

Figure 4.5: 3 and 1.5GY max doses correspond to the maximum doses of the first and second irradiated cylinder objects. The same linear behavior was found for the two curves and linked to show exactly the complementary curve presenting the same sensitivity of $4.22.10^{-3}cm^{-1}/Gy$.

4.3.2 – 3D QA for CSI treatment

Figure 4.6 shows the TPS image(A) and the measurement(B) image at the center of the matching fields region. From this image, the similarity between the planned dose and the measured dose can be observed. The gamma map in figure 4.7 is an example slice of the gamma evaluation using 3%/3mm/40%threshold criteria.

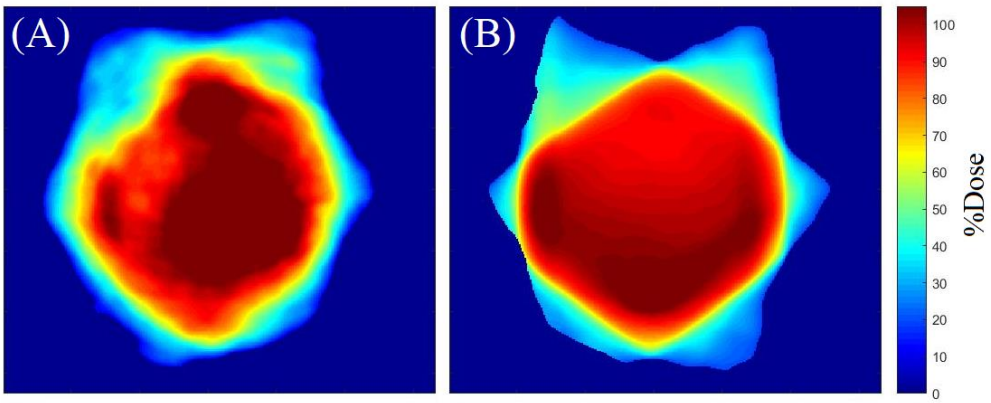

Figure 4.6: Dose distribution measured by the gel dosimeter with optical CT scanning (A) and the corresponding slice calculated by the TPS (B).

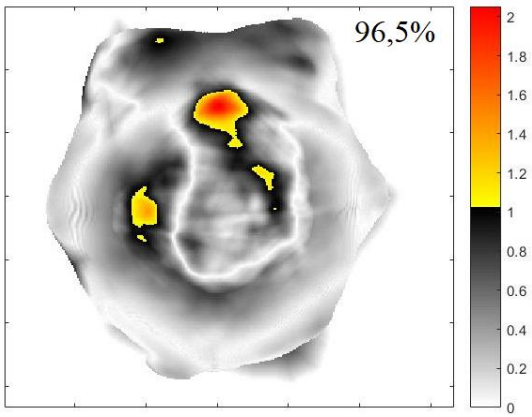

Figure 4.7: Gamma map index comparing the measured image and calculated image of figure 6, with 96.5% of approved pixels.

Table 4.1 shows the percentage of approved points in the gamma analyses at all slices evaluated at the junction region. The average approved pixels' percentage in this procedure is 91.9%, within the range of 89.6 % to 96.5%. This analysis detected two regions with less than 90% of the approved pixels in gamma analysis which would not be approved considering our criteria. This result is important because the 3D dosimetry by optical CT using FXO-f gel detected fail regions not detected in the conventional QAs.

Table 4.1: Gamma's pass rate for junction region in the cylindrical object in all slices at the junction region.

Z(cm)	Gamma(%)	Z(cm)	Gamma(%)
4.11	91.2	6.27	94.3
4.23	91.9	6.39	93.5
4.35	90.3	6.51	89.7
4.47	90.5	6.63	90.3
4.59	90.6	6.75	91.4
4.71	90.7	6.87	92.7
4.83	90.1	6.99	92.9
4.95	90.7	7.11	91.2
5.07	90.9	7.23	91.5
5.19	90.3	7.35	92.1
5.31	90.0	7.47	91.2
5.43	89.6	7.59	90.2
5.55	90.5	7.71	90.1
5.67	92.5	7.83	90.2
5.79	94.5	7.95	90.5
5.91	95.5	8.07	91.5
6.03	96.5	8.19	92.4
6.15	94.1	8.31	92.1

Comparing the result to literature, Wang found the range of 92.5 to 97.5% with the mean of 94.5% of the approved pixel in gamma analysis (Wang et al.,2013) using the 2D film dosimetry. Zhou et al. use the ArcCHECK and EBT3 film dosimeter to perform CSI plan QA, analyzing the impact of setup errors. This evaluation presented the range of 85% to 95% on the multiples dose and distance to agreement criteria (Zhou et al.,2020). The meaning of 90.1% of approved pixels in gamma analysis is a good result considering the setup of the irradiation was adapted from the conventional QA and not optimized for a truly 3D QA, and manually displacements for the irradiation process was made. Therefore, the results found in the literature and presented in this paper are related and consistent for the CSI planned using the multiple isocenter. It means that this technique requires more rigorous planning to have above 95% of gamma pixels approved in a truly 3D QA.

4.4 – Conclusion

These results show that gel dosimetry using the radiochromic gel FXO-f combined with optical CT allows tridimensional dose determination for a craniospinal procedure with complex multiple field planning. For the evaluation of the junction region, we found two region slices less than 90% of approved pixels. These regions of higher failure rates were not detected by conventional QA, which approved the treatment in a previous analysis. The findings of this studyreveal the importance of true 3D quality assurance in clinical procedures.

References

Asena, A., Nilsson, S., Smith, S. T., Kairn, T., Crowe, S. B., & Trapp, J. V. (2018). A method for obtaining three-dimensional measurements of HDR brachytherapy dose distributions using Fricke gel dosimeters and optical computed tomography. Australasian Physical & Engineering Sciences in Medicine. doi:10.1007/s13246-018-0715-y

Baldock, C., DeDeene, N., Doran, S., Ibbott, G., Jirasek, A., Lepage, M., Mcauley, K.B., Oldham, M., Schreiner, L.J., 2010. Polymer gel dosimetry. Phys. Med. Biol. 55, R1eR63.

Biltekin, F., Yazici, G. & Ozyigit, G. A novel inverse optimization based three-dimensional conformal radiotherapy technique in craniospinal irradiation. Phys Eng Sci Med 44, 265–275 (2021).

Cao, F., Ramaseshan, R., Corns, R., Harrop, S., Nuraney, N., Steiner, P., … Karvat, A. (2012). A Three-Isocenter Jagged-Junction IMRT Approach for Craniospinal Irradiation Without Beam Edge Matching for Field Junctions. International Journal of Radiation Oncology*Biology*Physics, 84(3), 648–654.

Deasy JO, Blanco AI, Clark VH. CERR: a computational environment for radiotherapy research. Med Phys 2003; 30:979–85.

Dyk, J. V., Barnett, R. B., Cygler, J. E., & Shragge, P. C. (1993). Commissioning and quality assurance of treatment planning computers. International Journal of Radiation Oncology Biology Physics, 26(2), 261–273.

Fogliata A, Bergstrom S, Cafaro I, Clivio A, Cozzi L, Dipasquale G, Hållström P, Mancosu P, Navarria P, Nicolini G, Parietti E, Pesce GA, Richetti A, Scorsetti M, Vanetti E, Weber DC: Cranio-spinal irradiation with volumetric modulated arc therapy: a multi-institutional treatment experience. Radiother Oncol 2011, 99:79–85. PMID:21421273

Gallo S , Pasquale S , Lenardi C , Veronese I, Gueli AM, 2021, Effect of ionizing radiation on the colorimetric properties of PVA-GTA Xylenol Orange Fricke gel dosimeters. Dyes and Pigments.v.187. 109141

Kelly, R. G., Jordan, K. J., & Battista, J. J. (1998). Optical CT reconstruction of 3D dose distributions using the ferrous-benzoic-xylenol (FBX) gel dosimeter. Medical Physics, 25(9), 1741–1750.

Jordan, K., Turnbull, D., Batista, J.J., 2013. Laser cone-beam computed tomography scanner geometry for large volume 3D dosimetry. J. Phys. Conf. Ser. 444, 012062.

Lee YK, Brooks CJ, Bedford JL, Warrington AP, Saran FH: Development and evaluation of multiple isocentric volumetric modulated arc therapy technique for craniospinal axis radiotherapy planning. Int J Radiat Oncol Biol Phys 2012, 82:1006–1012. PMID:21345612

Low, D., Dempsey, J., 2003. Evaluation of the gamma dose distribution comparison method. Med. Phys. 30, 2455e2464.

Pavoni, J.F., Pike, T.L., Snow, J., DeWerd, L., Baffa, O., 2012. Tomotherapy dose distribution verification using MAGIC-f polymer gel dosimetry. Med. Phys. 39,2877e2884.

Parker, W., Brodeur, M., Roberge, D., & Freeman, C. (2010). Standard and Nonstandard Craniospinal Radiotherapy Using Helical TomoTherapy. International Journal of Radiation Oncology*Biology*Physics, 77(3), 926–931.

Wang Z, Jiang W, Feng Y, Guo Y, Cong Z, Song B. (2013) A simple approach of three-isocenter IMRT planning for craniospinal irradiation. Radiat Oncol 8(1):217

Watanabe, Y., Gopishankar, N., 2010. Three-dimensional dosimetry of Tomotherapy by MRI-based polymer gel technique. J. Appl. Clin. Med. Phys. 12, 3273e3280.

Zhou Y, Ai Y, Han C, Zheng X, Yi J, Xie C., Jin, X., 2020 Impact of setup errors on multi-isocenter volumetric modulated arc therapy for craniospinal irradiation. J Appl Clin Med Phys 2020; 1–9

Chapter 5: Conclusions and perspectives

This study built and characterized an optical CBCT for a genuinely 3D QA using gel dosimetry in the radiotherapy clinical practice. A modification in two radiochromic gel dosimeters, FXO and TB, was also made by adding formaldehyde to increase their melting points and turn them useful in our environment temperatures. Finally, by combining this optical CBCT to the modified FXO gel a 3D QA was performed in a craniospinal radiotherapy procedure using IMRT, which proved the clinical applicability of the dosimetric system developed.

5.1 – Summary of the Contributions

This thesis brings to Brazil the first optical-CT as an alternative image technique to an alternative to MRI to perform 3D dosimetry. The results presented in chapter 2 show that the optical-CT based on the convergent light source has optical contrast and resolution to acquire good projections with low stray light contamination. The attenuation coefficients comparison with the spectrophotometer measurements presented excellent agreement between the OCT results and a consolidated measuring technique. The PDD curve achieved using the modified FXO-f gel dosimeter measurements in a large volume have great accordance with clinical reference dosimetry.

In chapter 3, the addition of formaldehyde to the Fricke Xylenol orange and Turnbull-blue radiochromic gel dosimeters improved their melting point, to 62ºC and 55ºC, respectively. This modification brings another advantage, the reduction of the diffusion coefficient for the FXO gel dosimeter. The dosimetric response of these gels

presented no dose rate dependency in the range from 100cGy/min to 1400cGY/min. This expanded the range of dose rate evaluation allows their use in the flatness filter-free LINACs. Besides, no energy dependence was found in the FXO-f and TB-f response to irradiation with 6 and 15 MV. The characteristic found for these two radiochromic gel dosimeters guarantee the usable in clinical context in terms of temperature's physical stability and dosimetric aspects.

In chapter 4, we apply the constructed CBCT combined with FXO-f in a clinical procedure of complexes craniospinal planning using IMRT technique. The success in the evaluation of this procedure brings to clinical context a truly 3D quality assurance tool to evaluate the region of the matching field of this IMRT plan. For this evaluation, the gel demonstrates linear behavior in the dose-response curve. In the gamma analysis, 3%/3mm at the center of the planning junction 96,3% of the pixel were approved. The present analysis found two slices with less than 90% pass rate. This fact is important because the conventional QAs have not detected this fail and it may indicate the contribution of a 3D dosimetric technique for evaluating complex clinical treatments.

5.2 – Future works and perspectives.

The whole area of gel dosimetry involves, chemistry, physics in radiation therapy, optical, computational coding mathematics, and clinical applications. We believe this study opens new challenges to gel dosimetry using radiochromic gels.

Optical-CT Acquisition and reconstructions: The present optical CT based on the convergent light source is fast and accurate on the dosimetry performance. However, we believe it is possible to improve the performance if finding an optimal gel vessel to perform the CT reconstructions is investigated, or changingto a plastic dosimeter that does not need a vessel. For the reconstruction programming coding in this work, we

applied the FDK and SIRT-TV in parallel programming, exploring the use of GPU power. In this meantime new GPUs with more cores and faster processing times have appeared on the gaming market and could be used to make faster the reconstructions. This hardware development stimulates the use of another algorithm, that at the moment requires a long time, like SART or OSC to improve the image quality

Gel dosimeters: The presented gel dosimeters FXO-f and TB-f are candidates to be used in the clinical context. The FXO-f still has the diffusion problem, so the 3D absorbed dose are not available all the time in the dosimetry. In comparison to TB-f, it presented better dose-response; however, no diffusion was found for the last one. Here we have some possibilities:

1 – Change the gelatin matrix for the FXO-f, for example, PVA (Polyvinyl alcohol), or try the agarose gel.

2 – With TB-f the only problem is the less sensitive than FXO-s, this can be solved by adding a chemical inside the gel that complements the irradiation dose effect, this can improve the sensitivity at the same time the gel will not present the formaldehyde.

3 –Initial work suggested the use of the genipin gel dosimeter. Because of the use of sulfuric acid and the melting point was lower than the presented gel in this work we decided to try other gels. However, the addition of formaldehyde can be done in genipin dosimeters to make this improvement. The advantage of the genipin gel dosimeter is that it is a less toxic chemical found for the dosimeters and the most water equivalent.

Clinical challenges: In this work, the problem of treatment with multiple isocenter planning and a junction of two planning was faced. Other clinical complexes distribution can be tried to perform 3D QA, for example, the multi-metastasis procedures in the brain

and the mama cancer procedures. The last one with a difficult geometry does reproduce in an optical simulated object. Also, then the small fields dosimetry.